POLARIZATION, MOTION, AND FRAGMENTATION: EXPLORING THE ROLE OF QUARKS IN THE NUCLEON THROUGH SEMI-INCLUSIVE LONGITUDINAL SPIN ASYMMETRIES AT HERMES

BY

JOSHUA GEORGE RUBIN

B.A., University of California at Santa Barbara, 2000
B.S., University of California at Santa Barbara, 2000
M.S., University of Illinois at Urbana-Champaign, 2004

DISSERTATION

Submitted in partial fulfillment of the requirements
for the degree of Doctor of Philosophy in Physics
in the Graduate College of the
University of Illinois at Urbana-Champaign, 2009

Urbana, Illinois

Doctoral Committee:

Associate Professor Matthias Grosse-Perdekamp, Chair
Professor Naomi C. R. Makins, Director of Research
Professor Laura H. Green
Professor John D. Stack

Acknowledgments

This dissertation and the research that fills its pages could not have happened without the help of a small army of colleagues, friends, and family. First of all, I'd like to thank my parents, Karen and David, my sister, Julia, and my brother, Daniel, for their inexhaustible interest, encouragement, and support.

I'd like to extend my most sincere gratitude to Krista Kloth for giving me reason to stay in Champaign-Urbana through some of the bleakest hours of my graduate career. She encouraged and inspired me through much of this work. I'd also like to thank the Kloth family for making a Californian feel completely at home in the Midwest.

I'd also like to extend a heartfelt thank you to my good friend and adviser, Naomi Makins, whose talents for explaining patiently, conceptualizing even the most abstract concepts, and listening with curiosity and respect are truly exceptional. Most, if not all, of the methods developed and results presented in this dissertation are direct products of our conversations and the encouragement I was given to trust and explore my ideas. Thanks to my group-mates, dear friends, and world travel companions, Alex Linden-Levy and Rebecca Lamb, for getting me into and keeping me out of trouble, respectively. Thanks also to my senior my group-mate, Slow Production guru, and reluctant European adventurer, Aaron Andrus. Thank you to Micah Stoutimore who's been a close friend and confidant since we shared an office in our first year and who's patiently humored (and even participated in!) an assortment of odd ideas, hobbies, and schemes. Sincere thanks also to Drew Gifford, Khurram Gillani, and Eric White who have been compatriots and spirited thinkers since our first days in Urbana.

Thank you to my HERMES colleagues who are exceptionally creative, vigorous, first-rate scientists. In particular, I'd like to thank Polina Kravchenko without whose crosscheck and collaboration the results presented in this dissertation would be greatly reduced in quality and reliability. Also, thank you to Elke-Caroline Aschenauer for guidance, helpful suggestions, and the occasional opportunity to practice raising my voice in lively debate.

I'd like to thank the faculty of the Nuclear Physics Lab for providing a collaborative and open environment in which students can learn and share and particularly to Matthias Grosse Perdekamp and Jen-Chieh Peng for their enthusiasm and encouragement. I'd also like to extend

my gratitude to Penny Sigler in the NPL office for her encouragement, for taking care of piles of travel-related paperwork, and for greatly simplifying other logistics that would have otherwise taken significant thought and time. Sincere thanks also to Wendy Wimmer in the Physics Department Graduate Records office for making the thesis defense/deposit/graduation process tolerable – what an incredible relief it is to have someone trying to simplify a tiring and stressful process rather than mechanically presenting students with a list of rules and forms.

I'd also like to take this moment to thank the Department of Physics, the National Science Foundation, and the Nuclear Physics Lab for the financial support I've received as a teaching assistant, as a research assistant, and as a recipient of the Felix T. Adler fellowship.

Finally, I'd like extend my sincere appreciation to Dolce, my cat, for her patience and company through many nights of dissertation typing and for all the edits she made (most of which were improvements) while I was busy making coffee.

Contents

Preface **vi**

1 Theoretical Background **1**

1.1 Introduction . . . 1
1.2 *ep* Scattering . . . 2
1.3 Confinement and Asymptotic Freedom . . . 7
1.4 Parton Distribution Functions . . . 7
1.5 Isospin Symmetry and the Neutron . . . 10
1.6 Bring in the Gluons! . . . 11

2 The HERMES Experiment **12**

2.1 HERA . . . 12
2.2 The HERMES Target . . . 13
2.3 The HERMES Spectrometer . . . 14
2.4 Offline Data Production . . . 19

3 Data Analysis **22**

3.1 Particle Identification . . . 22
3.2 Data Selection . . . 28
3.3 Binning . . . 35
3.4 Burst-Level Data Selection . . . 36
3.5 Polarimetry . . . 38

4 Asymmetries **39**

4.1 The Longitudinal Double-Spin Asymmetry . . . 40
4.2 Nucleon Polarizability . . . 44
4.3 Unfolding and the Born Asymmetry . . . 44
4.4 Azimuthal Correction for Semi-Inclusive Asymmetries . . . 53
4.5 Final Born Asymmetries . . . 60

4.6 Systematic Uncertainties . . . 71

5 Fragmentation and the Purity Method **77**

5.1 Untangling the Complexity: Three Complementary Strategies . . . 77

5.2 Limitations of Fragmentation Symmetries . . . 78

5.3 The Purity Method . . . 83

6 The Quark Helicity Distributions **102**

6.1 The Quark Polarizations . . . 102

6.2 The Quark Helicity Densities of the Nucleon . . . 110

6.3 Fits to the Quark Polarizations . . . 113

6.4 Valence Distributions and Difference Asymmetries . . . 116

6.5 The Light Sea Asymmetry . . . 116

References **118**

Author's Biography **121**

Preface

The motivation for this work was to improve upon prior analyses that extracted the quark helicity distributions, $\Delta q(x)$, of the proton. These extractions, performed by the HERMES collaboration, were *excellent* analyses, the most recent of which contained the vast majority of the data analyzed here. "If they were so good, how much could you improve on their results?" one might ask. Well, not to spoil the punch line, but *some*. The precision was improved modestly and our understanding of the systematic uncertainties was improved more significantly. The reader is welcome to jump to Chapter 6 and see.

The approach that we took however was to *try* many new things. Not all of these efforts yielded improvements on the scale we had hoped for, but many interesting new techniques were developed and we were able to produce several related new results along the way. Let me suggest then that rather than thinking of Chapter 6 as the result of this analysis, consider that *there are valuable new results and insights scattered throughout this work.*

Chapter 4 contains several new double-spin asymmetries which are results in their own right. The $p_{h\perp}$ dependence is plotted for the first time with HERMES data which is uniquely hadron separated. The hadron charge difference asymmetry is presented which, in combination with the quark helicity densities of Chapter 6, can put limits on fragmentation symmetry breaking in semi-inclusive DIS. Additionally, a novel method of unfolding yields (reducing smearing effects from detector resolution limitations and QED radiation) was developed and presented here for the first time which potentially allows new kinds of asymmetries to be constructed which were unavailable before. Also, this chapter describes the method by which the first ever three dimensionally binned SIDIS double-spin asymmetries were produced. These asymmetries, which will be used as the data inputs for the $\Delta q(x)$ extraction, are valuable inputs to world fits being performed by theorists.

Chapter 5 further explores this idea of fragmentation symmetry breaking with Monte Carlo studies of fragmentation functions. These studies test assumptions which are frequently made in the interpretation of asymmetries like the hadron charge difference of the prior chapter and suggest that these assumptions should be approached with some caution. Also, a technique for tuning and more importantly propagating systematic uncertainty through non-analytic Monte Carlo models, like the Lund-String model which provides an essential input to the $\Delta q(x)$ extraction, is developed

and potentially has widespread applications.

That being said, the author hopes you enjoy the techniques developed and results presented in the following chapters.

Chapter 1

Theoretical Background

The topic of this work, most simply put, is the spin-structure of the *nucleon*, a constituent particle of an atom's nucleus which can be either a proton (p) or a neutron (n). By *spin-structure* we refer to the configuration of the sources of the angular momentum which contribute to the $S = \hbar/2$ that these composite particles have been observed to carry.

While a complete account of the history of nucleon structure, deep-inelastic scattering, or particle physics is outside the scope of this work, explaining a few key steps is essential and will introduce concepts and terminology that will be relevant here and in later chapters.

1.1 Introduction

Hideku Yukawa is credited with the first theory of the *strong force* [1], a force which binds together nuclei (and, as we will see, nucleons as well), which are positively charged and thus subject to very large electromagnetic, or *Coulomb*, repulsion. By estimating the short-range behavior of this force (as it's clearly not observed at a distance scale larger than that of the nucleus), he estimated the mass of the exchanged particle at approximately 1/6 that of the proton or ∼150 MeV. This particle became referred to as a *meson*, or middle-weight particle, in contrast to the heavier proton and neutron, known as *baryons*, and the light-weight electron, a *lepton*, with a mass of only 0.511 MeV. In 1947 Cecil Powell published the first emulsion-track observation of Yukawa's meson [2], the pi-meson or *pion*, with an estimated mass of $375 \pm 70 m_e$ (where m_e is the electron's mas), or 192 ± 36 MeV. This earned Yukawa the Nobel Prize in Physics in 1949. Although we've come to understand that the pion is a composite particle and not the fundamental carrier of the strong force, it continues to be understood to be an essential effective force-carrier in nucleon-nucleon interactions.

Over the next twenty years, experimental particle physics proved to be a prolific pursuit. Many new particles were identified by mass, charge, and a theoretically ill-understood property

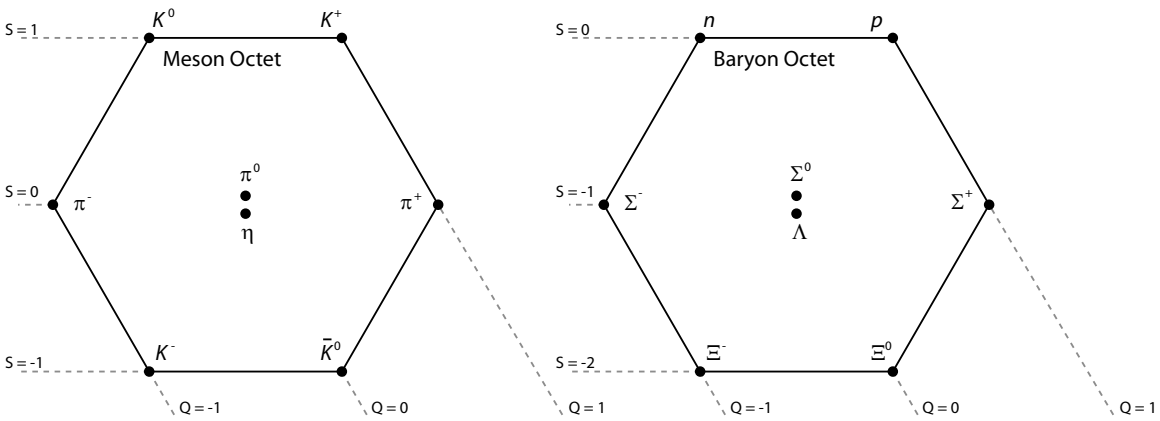

Figure 1.1: The eight light mesons and baryons arranged into *octets* according to their strangeness and charge.

known as *strangeness*. Particles carrying strangeness were largely characterized by long lifetimes and production in pairs – the hallmark of a quantity conserved in fundamental interactions.

Seeking to make sense of this growing catalog of observed particles, Murray Gell-Mann organized them into geometric configurations which he would refer to as *the Eightfold Way*. Figure 1.1 depicts the lightest eight mesons and baryons arranged into hexagonal *octets* according to their charge and strangeness. In 1964 Gell-Mann observed that the most theoretically elegant explanation for these patterns was a system of three fundamental spin-$\frac{1}{2}$ constituents (suppressing the $\hbar$ for convenience), u, d, and s, and their antiparticles, $\bar{u}$, $\bar{d}$, and $\bar{s}$, which all carry fractions of the electron charge. These labels refer to the quark *flavor*, a somewhat mysterious property that distinguishes them from each other. The symbols, u, d, and s stand for *up*, *down*, and *strange* quark flavors. He called these particles *quarks* [3] borrowing the term from James Joyce's *Finnegans Wake*. Gell-Man's $u(\bar{u})$ quark carries a charge of $\frac{2}{3}e$ ($-\frac{2}{3}e$) and zero strangeness, the $d(\bar{d})$ carries a charge of $-\frac{1}{3}e$ ($\frac{1}{3}e$) and zero strangeness, and the $s(\bar{s})$ carries $-\frac{1}{3}e$ ($\frac{1}{3}e$) with a strangeness of +1(-1). Furthermore, this formulation coupled with the knowledge that the mesons and baryons respectively carry integer and half integer spin suggests that baryons are composed of three quarks and mesons two[1].

1.2 *ep* Scattering

Let us, for a moment, take a detour from our historical introduction to discuss the basic terminology of electron-proton scattering. Figure 1.2 depicts a beam lepton interacting with a proton via the exchange of a virtual photon. This virtual photon, γ^*, is our probe; it will interact

[1] Gell-Mann actually entertains the notion that baryons could carry *any* odd number of quarks greater than one and that mesons could carry any even number. There has been a great deal of recent experimental activity (by HERMES [4] and many other collaborations) regarding the possibility of these exotic five-quark baryon states. Despite several early positive signals, the combined experimental evidence seems to be converging upon a negative consensus [5].

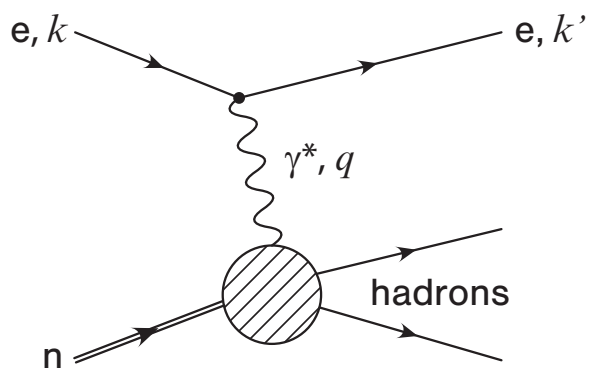

Figure 1.2: An electron, e, with initial four-momentum k, interacts with a nucleon, n, via the exchange of a virtual photon ($\gamma*$) leaving a scattered electron with four-momentum k' and an unspecified hadronic final state.

either coherently with the nucleon as a whole or incoherently with one of the partons within. The symbols k and k' represent the incoming and outgoing four-momenta (containing both the energy and the momentum three-vector) of the beam lepton. E and E' will be used specifically to refer to their energies. As k and k' are measured in a scattering event, energy and momentum conservation allows us to compute the four-momentum of the virtual photon, q. ν will be used to represent it's energy. Table 1.1 lists variables essential to characterizing the event. To compute these quantities, we need observe only the scattered beam lepton, which is referred to as an *inclusive* measurement. This terminology suggests that when requiring only the scattered lepton, all of the other possible configurations of the final state are *included*. As we will see, a remarkable amount of information about the structure of the nucleon is accessible through inclusive scattering.

At this point the Lorentz invariant Q^2 is of particular interest. It can be thought of as representing the inverse of the *wavelength* of the virtual photon and defining the energy scale of the interaction. Figure 1.3 is a cartoon illustration of *ep* scattering in two distinctly different Q^2 regimes. If Q^2 is significantly smaller than 1 GeV^2 (a scale comparable to the *size* of the proton), the nucleon is likely probed as a coherent whole. In this regime, if scattering occurs elastically ($W^2 = M_p^2$), the proton's cross section is best written in terms of a *form factor*:

Variable	Formula	Description
M		Mass of the target nucleon
ν	$E - E'$	Energy of the virtual photon (measured)
Q^2	$-(k - k')^2$	Negative virtual photon 4-momentum squared
W^2	$M^2 + 2M\nu - Q^2$	Invariant mass squared of the hadronic final state
x	$Q^2/2M\nu$	*Bjorken-x*. The parton momentum fraction in the infinate momentum frame.

Table 1.1: Kinematic variables necessary for desctibing an *ep* interaction.

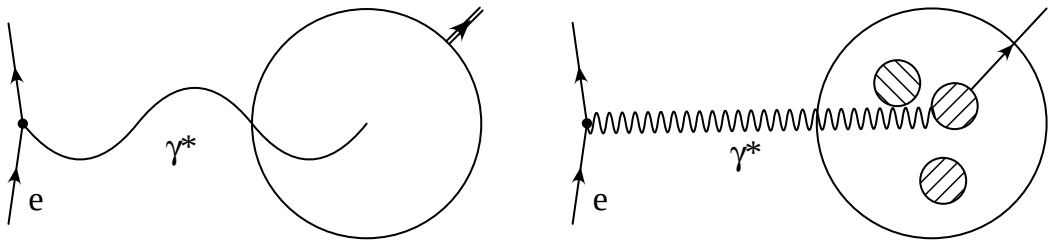

Figure 1.3: As the energy of the virtual photon increases, increasingly small sub-structures (partons) can be resolved. Ultimately, the scale of the nucleon itself is lost to a large degree and ceases to influence scattering behavior.

$$\frac{d\sigma}{d\Omega} = \left(\frac{d\sigma}{d\Omega}\right)_{\text{Mott}} |F(q)|^2 , \tag{1.1}$$

where $(d\sigma/d\Omega)_{\text{Mott}}$ is the cross section for a structureless point target and the form factor,

$$F(\boldsymbol{q}) = \int \rho(\boldsymbol{x}) e^{i\, \boldsymbol{q}\,\cdot\,\boldsymbol{x}} d^3x, \tag{1.2}$$

is a momentum-space representation of a diffuse charge distribution.

The right panel of Figure 1.3 depicts a large-Q^2 event in which the virtual photon has a small enough wavelength to clearly resolve individual elements of the nucleon's substructure. Deep inelastic scattering (DIS), where the parton structure of the nucleon is resolved, is the focus of this work. $Q^2 > 1$ GeV^2 is conventionally considered to the boundary of this regime[2]

1.2.1 Bjorken Scaling and the Quark Parton Model

In the late 1960s J. D. Bjorken predicted that if at increasing values of Q^2 scattering was occurring on point-like *partons*, then the structure function $F(\nu, Q^2)$ (described below) should depend on only one free parameter as the scale of the nucleon is lost. Bjorken's prediction was supported by data [6] in which it was observed that F approaches a constant value as a function of the ratio ν/Q^2. This feature of deep inelastic scattering is known as Bjorken scaling.

Bjorken's next step was to combine this strong support for the parton picture with Feynman's concept of a "Frozen Approximation". This entails interpreting the interaction in the *infinite momentum frame* – a reference frame in which the nucleon has infinite momentum. This has several important consequences.

- In such a frame, the partons are *frozen* by relativistic time dilation. In this limit, a parton could be struck by the virtual photon without any interaction (coherence) with other partons.
- The mass of the parton is negligible compared to the longitudinal momentum of the partons.

[2]Strictly speaking, the Q^2 requirement allows perterbative QCD to be used to describe the event. An additional DIS requirement on the final state invariant mass, $W^2 > 4$ GeV^2, excludes coherent scattering. This requirement is discussed further in Sections 3.2.1 and 4.1.2.

- The intrinsic transverse momentum of partons, k_T, becomes negligible.
- A parton i has momentum $p_i = x_i P$, where P is the total momentum of the nucleon.

The scaling variable x introduced in the last bullet is often called *Bjorken-x* and represents the longitudinal momentum fraction of the nucleon carried by the struck quark in the infinite momentum reference frame.

A general inelastic unpolarized lepton-proton cross section can be written

$$\frac{d\sigma}{d\Omega dE'} = \frac{\alpha^2}{Q^4}\frac{E'}{E}\left\{W_2\left(\nu, q^2\right)\cos^2\frac{\theta}{2} + 2W_1\left(\nu, q^2\right)\sin^2\frac{\theta}{2}\right\} \tag{1.3}$$

with structure functions W_1 and W_2 parameterizing the structure of the nucleon. θ is the angle between the scattered lepton and the beam axis in the target rest frame.

In Feynman's approximation, however, the nucleon takes the form of a collection of non-interacting point structures [7]. Because of this, for *each parton* we can write,

$$W_1^{(1)}\left(\nu, Q^2\right) = \frac{Q^2}{2m^2}\,\delta\left(\nu - \frac{Q^2}{2M}\right) = \frac{Q^2}{4m^2\nu}\,\delta\left(1 - \frac{Q^2}{2m\nu}\right)$$

$$W_2^{(1)}\left(\nu, Q^2\right) = \delta\left(\nu - \frac{Q^2}{2m}\right) = \frac{1}{\nu}\,\delta\left(1 - \frac{Q^2}{2m\nu}\right). \tag{1.4}$$

The partons here behave like simple free point particles. If we define $\omega \equiv \frac{2M\nu}{Q^2}$, and then substitute $m = xM(= \sqrt{x^2E^2 - x^2\vec{P}^2})$, we can rewrite Equation (1.4),

$$W_1^{(1)}\left(\omega\right) = \frac{1}{2x^2\omega M}\,\delta\left(1 - \frac{1}{x\omega}\right)$$

$$W_2^{(1)}\left(\omega\right) = \frac{1}{\nu}\,\delta\left(1 - \frac{1}{x\omega}\right). \tag{1.5}$$

Introducing $q^{(1)}\left(x\right)$, the probability that a particular parton is found with momentum fraction x, we can write the total W_2 for the nucleon:

$$W_2\left(\omega\right) = \frac{1}{\nu}\sum_q \int_0^1 dx\; e_q^2\; q^{(1)}\left(x\right)\; x\;\delta\left(x - \frac{1}{\omega}\right). \tag{1.6}$$

We have thus expressed W_2 as a sum over its constituent partons. Here one can see that the delta function equates $1/\omega$, a kinematic expression, with x, the parton momentum fraction. The choice to denote the parton momentum probability $q^{(1)}(x)$ was done with the knowledge that we would soon use $q(x)$ to denote the *number density* of partons. Unlike $q^{(1)}(x)$, which represents a single parton, $q(x)$ will represent all quarks of flavor q. Bjorken identifies these point-like partons with Gell-Mann's quarks.

Additionally, Bjorken observed that a simple three quark model was deficient in that it

produces a cross section that vanishes as $x \to 0$. This prediction was at odds with the CERN *ep* data available which showed no indication of a vanishing low-x cross section. Bjorken's solution, one which is the prevailing picture of the nucleon today, is of three valence quarks, which are responsible for the nucleon's quantum numbers, and a *sea* of quarks and antiquarks. Because these sea quarks are produced from gluons originating from the valence quarks, they carry less momentum and hence reside at a lower x and because they occur in particle-antiparticle pairs are unconstrained in number.

1.2.2 Structure Functions

More generally, the cross section for polarized lepton-nucleon scattering,

$$\frac{d\sigma}{d\Omega dE'} = \frac{\alpha^2}{Q^4}\frac{E'}{E}L^e_{\mu\nu}W^{\mu\nu}, \tag{1.7}$$

is the contraction of the well known leptonic tensor, $L^e_{\mu\nu}$, and a general hadronic tensor (a *hadron* is a composite particle – either a meson or a baryon), $W^{\mu\nu}$, which we can use to parameterize the structure of the nucleon.

$W^{\mu\nu}$ may be written as the sum of two parts. The first of these is symmetric,

$$W^{(S)}_{\mu\nu} = \frac{1}{M}\left(-g_{\mu\nu} + \frac{q_\mu q_\nu}{Q^2}\right)F_1 + \frac{1}{M^2\nu}\left(p_\mu - \frac{p\cdot q}{Q^2}q_\mu\right)\left(p_\nu - \frac{p\cdot q}{Q^2}q_\nu\right)F_2, \tag{1.8}$$

where $F_1 = MW_1$ and $F_2 = \nu W_2$ from the previous section. These *spin-averaged structure functions* represent the longitudinal momentum distributions of the partons in the nucleon.

The second part of the hadronic tensor is antisymmetric,

$$W^{(A)}_{\mu\nu} = \frac{\epsilon_{\mu\nu\alpha\beta}}{M\nu}\, q^\alpha S^\beta g_1 + \frac{\epsilon_{\mu\nu\alpha\beta}}{M^2\nu^2}\, q^\alpha \left[(P\cdot q)\, S^\beta - (S\cdot q)\, p^\beta\right]\, g_2, \tag{1.9}$$

where S is the initial spin vector of the nucleon. The *spin-dependent structure functions* g_1 and g_2 are composed of the quark spin densities which are at the heart of this work.

In the simple parton model, in which we assume $Q^2 \to \infty$ and that the partons are massless, non-interacting, and have no transverse momentum, the structure functions are not independent. It follows from (1.5) and (1.6) that,

$$2xF_1(x) = F_2, \tag{1.10}$$

which is known as the Callan-Gross relation. Similarly, in this simple model, g_1 and g_2 are related. The relationship is described by the Wandzura-Wilczek relation [8],

$$g_2(x) = -g_1(x) + \int_x^1 \frac{dx'}{x'} g_1(x'). \tag{1.11}$$

1.3 Confinement and Asymptotic Freedom

In 1973, David Gross and Frank Wilczek formulated a theory of the strong force [9] (for which they would win the 2004 Nobel Prize with David Politzer) that accommodated the following observations:

1. Gell-Mann's quarks are never observed in a free state. They are always appear in composite particles
2. Hadrons seem to come in two configurations, either baryons composed of three valence quarks (or antiquarks), or mesons composed of a valence quark and an antiquark.
3. Bjorken scaling suggests that inside hadrons, quarks can behave as virtually free particles.

This theory contained the concept that quarks and gluons carry *color charge* (conserved charge quanta that combine like colors on a color wheel). Because of this, the theory would be known as *quantum chromodynamics* (QCD). In this theory quarks carry color, antiquarks carry anti-color, and gluons carry *both* a color and an anticolor. Asymptotic freedom, the property that at close ranges quarks behave like free particles, is a critical result of QCD. Unlike the more familiar gravity and electromagnetism, the force produced by QCD *increases in strength with distance.* This gives us the concept of *color confinement*: that free color is never observed, and all hadrons contain quarks and gluons in net colorless configurations. Energetic quarks escaping their colorless bound state will, through the energy stored in the color-field, produce quark-antiquark pairs such that the hadrons in the final state are once again colorless. QCD was further supported in 1979 by the experimental observation of three-jet events at DORIS [10]– the clear signature of the flavorless gluon.

An important (but unfortunate) feature of this theory is that perturbation theory, an essential mathematical tool for making calculations of observables based upon fundamental theories of interactions, is somewhat limited in its applicability. While hard interactions, like energetic scattering events, can be expanded perturbatively – in orders of gluon vertices – the structure of the dynamical bound states is non-perturbative: the number of gluons involved becomes large, if finite at all, making perturbative series approximations impossible. The *fragmentation process*, by which an escaping color-charged parton *hadronizes* producing new colorless bound states is also non-perturbative, suffering from similar difficulties.

1.4 Parton Distribution Functions

The left side of Figure 1.4 depicts the simplest possible interpretation of a DIS event. It is of *leading order* in QCD, meaning that outside of the circle, which contains the non-perturbative

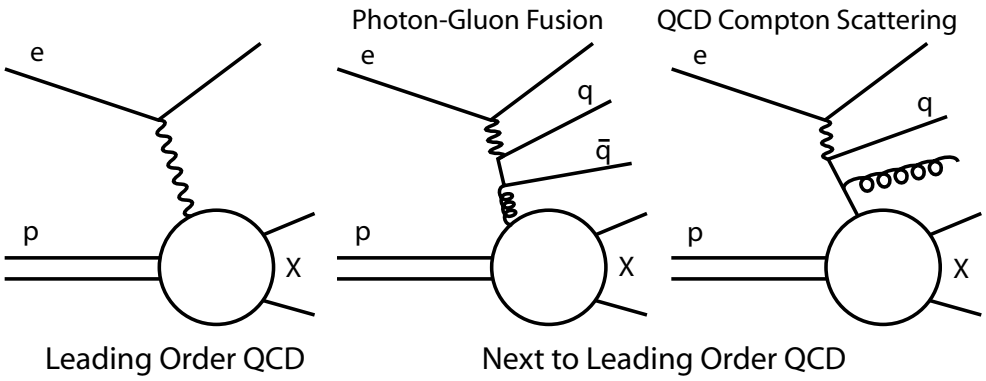

Figure 1.4: LO NLO.

nucleon–structure and the fragmentation process, there are no gluons explicitly included the calculation.

In leading-order then, we can write down an expression for the inclusive structure function $F_1(x)$ of Equation 1.8 in terms of the spin-independent parton distribution function (PDF) $q(x)$:

$$F_1(x, Q^2) = \frac{1}{2} \sum_q e_q^2 \, q(x, Q^2), \tag{1.12}$$

where the index q runs over both quarks and antiquarks. The PDF $q(x)$ is a number density which can be integrated over x to yield the total number of quarks in the proton of flavor q. From this we can write

$$N_{q_v} = \int_0^1 q(x, Q^2) - \bar{q}(x, Q^2) \, dx, \tag{1.13}$$

where N_{q_v} is the number of valence quarks of flavor q in the proton. The parton distributions have a weak Q^2 dependence which we have included explicitly here. This will be described further in Section 1.6.

The spin-dependent structure function, $g_1(x, Q^2)$ of Equation 1.9 can be written in terms of the *helicity densities*, or spin-dependent parton distribution functions $\Delta q(x, Q^2)$:

$$g_1(x, Q^2) = \frac{1}{2} \sum_q e_q^2 \, \Delta q(x, Q^2), \tag{1.14}$$

where

$$\Delta q(x, Q^2) = q^+(x, Q^2) - q^-(x, Q^2) \tag{1.15}$$

is the difference between the densities of quarks with polarizations aligned (+) and antialigned (−) with the spin of the proton. The flavor separation of $g_1(x, Q^2)$ into flavored $\Delta q(x, Q^2)$ functions is a primary goal of this work.

1.4.1 Semi-Inclusive DIS (SIDIS) and Factorization

A measurement of the helicity distributions, $\Delta q(x, Q^2)$, is difficult because our lepton beam is sensitive to the cross section, which is proportional to the structure functions, rather than individual quark flavor distributions. In fact, as the electromagnetic interaction is oblivious to quark flavor, an inclusive measurement alone can *at best* probe $\Delta\Sigma$, the sum of polarized parton distributions[3]. To assist us in unraveling these contributions, we will additionally consider the *semi-inclusive* structure functions. By "semi-inclusive", we mean that in addition to the scattered beam electron we require a final state hadron to be measured as well – usually a pion or kaon. The identity of these hadrons will give us a crucial hint regarding the flavor of the struck quark. In leading order the semi-inclusive F_1^h and g_1^h can be written:

$$F_1^h(x, Q^2, z) = \frac{1}{2} \sum_q e_q^2 \; q(x, Q^2) \; D_q^h(Q^2, z), \tag{1.16}$$

and

$$g_1^h(x, Q^2, z) = \frac{1}{2} \sum_q e_q^2 \; \Delta q(x, Q^2) \; D_q^h(Q^2, z). \tag{1.17}$$

Here $D_q^h(z, Q^2)$ is a *fragmentation function*, a number density describing the likelihood that an event in which a quark of flavor q is struck produces a final state hadron of variety h carrying a fraction z of the virtual photon's energy. We should note here the principle of *factorization*. At sufficiently high Q^2 and W^2, the parton distribution function and the fragmentation function depend on independent variables. That is, except for the weak dependence on Q^2, the nucleon structure depends only on x and the fragmentation function depends only on z.

Strictly speaking, the semi-inclusive structure functions are also functions of the hadron transverse momentum with respect to the q-vector (the topic of Section 4.5.2) which can originate both in k_T, the intrinsic transverse motion of the quarks and in p_T, the transverse "kick" given to new hadrons by the fragmentation process. Moreover, these structure functions can depend on the azimuthal scattering angle (also around the q-vector) which we have tried to integrate out for the purpose of this analysis. Correcting for its interaction with the spectrometer acceptance, however, is a somewhat complicated story and the topic of Section 4.4.

1.4.2 The Purity Method

While both asymmetries and purities are the topics of their own chapters (4 and 5 respectively), we will introduce them briefly here. The (semi-)inclusive longitudinal double-spin asymmetry is

[3] A flavor decomposition of the spin-dependant structure of the nucleon is expected in the near future from the colliders, PHENIX [11] and STAR [12], at RHIC. They have proposed to use the weak interaction, $q\bar{q} \to W$, which *is* sensitive to flavor, by triggering on final state muons (a possible decay product of the W) in pp scattering.

defined as follows:

$$A_1^{(h)}\left(x, Q^2\left(, z, p_{h\perp}\right)\right) = \frac{\sigma_{1/2}^{(h)} - \sigma_{3/2}^{(h)}}{\sigma_{1/2}^{(h)} + \sigma_{3/2}^{(h)}}\left(x, Q^2\left(, z, p_{h\perp}\right)\right) = \frac{g_1^{(h)}}{F_1^{(h)}}\left(x, Q^2\left(, z, p_{h\perp}\right)\right). \tag{1.18}$$

The 3/2 and 1/2 labels refer to the total angular momentum J_z of the virtual-photon–nucleon system along the virtual photon direction. The J_z state indicates whether the photon and nucleon spins are aligned (3/2) or anti-aligned (1/2). While the semi-inclusive asymmetries also depend on ϕ_h, we intend to integrate over this variable (experimentally) and will hence omit it from this discussion. The asymmetry $A_1^{(h)}$ is equivalent to the following measurable yield ratio:

$$A_1^{(h)}\left(x, Q^2\left(, z, p_{h\perp}\right)\right) = \mathbb{C}(x, Q^2)\frac{N_{\uparrow\downarrow}^{(h)} - N_{\uparrow\uparrow}^{(h)}}{N_{\uparrow\downarrow}^{(h)} + N_{\uparrow\uparrow}^{(h)}}\left(x, Q^2\left(, z, p_{h\perp}\right)\right), \tag{1.19}$$

where $N_{\uparrow\uparrow(\uparrow\downarrow)}$ is an experimental event yield in the parallel (antiparallel) beam-target spin configuration. $\mathbb{C}(x, Q^2)$ is simply a placeholder for the kinematic factors and corrections which we will spend the bulk of Chapter 4 computing.

Writing down the fully factorized expression for the semi-inclusive asymmetry,

$$A_1^h(x, Q^2, z, p_{h\perp}) = \frac{\sum_q\ e_q^2\ \Delta q(x, Q^2)\ D_q^h(Q^2, z, p_{h\perp})}{\sum_{q'}\ e_{q'}^2\ q'(x, Q^2)\ D_{q'}^h(Q^2, z, p_{h\perp})} = \sum_q\ P_q^h(x, Q^2, z, p_{h\perp})\frac{\Delta q(x, Q^2)}{q(x, Q^2)}, \tag{1.20}$$

where

$$P_q^h(x, Q^2, z, p_{h\perp}) = \frac{e_q^2\ q(x, Q^2)\ D_q^h(z, p_{h\perp})}{\sum_{q'}\ e_{q'}^2\ q'(x, Q^2)\ D_{q'}^h(Q^2, z, p_{h\perp})}. \tag{1.21}$$

We call P_q^h a *purity*. It represents the probability that an observed hadron of variety h was produced by striking a quark of flavor q. The purity is the key to *flavor tagging* events by observed hadron type and will allow us to disentangle the sum of quark contributions that comprise the structure functions. As we will discuss in detail in Chapter 5, these purities are generated using a Monte Carlo simulation containing world fits to the unpolarized PDFs, $q(x, Q^2)$ and a carefully tuned phenomenological fragmentation model.

1.5 Isospin Symmetry and the Neutron

We will be taking advantage of both hydrogen (proton) and deuterium (deuteron, p-n) targets as the proton and neutron give us different combinations of parton distribution functions. It seems important to note at this point that we will be assuming *isospin* symmetry. This symmetry is the notion that the proton and neutron can be thought of as forming a symmetry group and that the proton (uud) and neutron (ddu) are isospin conjugates of one another. Though the bare u and d

masses differ somewhat ($\sim$ 2 MeV and $\sim$ 5 MeV respectively), they are both tiny with respect to the $\sim$900 MeV nucleon mass. The vast majority of the energy for both nucleons resides in the highly relativistic strong field. Because of this, we can assume that the neutron PDFs, $q_n(x, Q^2)$, are the isospin conjugates of the proton PDFs, $q(x, Q^2)$– i.e. $u \rightleftharpoons d$ and $\bar{u} \rightleftharpoons \bar{d}$

1.6 Bring in the Gluons!

Although the gluon will play a fairly modest role in our calculations, it seems prudent to remember that of the nearly 1 GeV that makes up the mass of the proton, only 0.1% can be attributed to the bare mass of the valence quarks. This reminds us that unlike an atomic bound state, the nucleon is highly relativistic. A large amount of energy resides in the color field that binds hadrons together, and that field, depending on how it's probed, is potentially composed of numerous gluons and sea quarks. These gluons affect DIS in two primary ways.

1. The weak Q^2 dependence of the PDFs and fragmentation functions that we've mentioned previously is a result of the increasing resolving power that our virtual photon probe has as Q^2 increases. As the photon is able to probe smaller regions, momentum which was previously attributed to quarks is now observed to belong to soft gluon radiation in the vicinity of the quark. This has the effect of shifting the PDFs to smaller x as Q^2 is increased. This effect is well known and is described by *Altarelli-Parisi* (or *DGLAP*) evolution equations. For example, this evolution can be computed [7],

$$\frac{d}{d\log Q^2}\ q(x, Q^2) = \frac{\alpha_s}{2\pi}\int_x^1 \frac{dy}{y}\ q(y, Q^2)\ P_{qq}(\frac{x}{y}), \tag{1.22}$$

   where P_{qq} is a *splitting function*, reflecting the likelihood that the final state quark will have given up a certain energy fraction to a radiated gluon. These splitting functions for both quarks and gluons can be computed to the desired order using perturbation theory.

2. While the strategy of this analysis is to interpret our semi-inclusive asymmetries in a leading-order formalism, another strategy is to interpret events at next-to-leading order (NLO) [13] by explicitly including $O(\alpha_s)$ diagrams like those on the right side of Figure 1.4. This results in a somewhat more complicated expression for the $g_1(x, Q^2)$ structure function which includes a singlet structure function ($\Delta q_S \equiv \Delta\Sigma$), non-singlet structure function (Δq_{NS}), and a spin-dependent gluon PDF ($\Delta g(x)$). Each of these functions is found in a convolution over x with various calculable coefficient functions. As this strategy grants access only to certain combinations of PDFs, it would offer little advantage in our effort to disentangle each of the quark contributions to the proton's structure.

Chapter 2

The HERMES Experiment

This chapter is intended to provide the necessary introduction to the experimental setup with which the data analyzed in following chapters was produced. For the most part, I will be brief as detail on these topics is readily available. I will be drawing heavily on a 1998 HERMES publication [14] describing the detector and on the excellent *Techniques for Nuclear and Particle Physics Experiments: A How-to Approach* by W.R. Leo [15] for most explanations of detector physics. That being said, I hope the summary provided here provides readers with enough information to enjoy the detailed analysis description that follows.

2.1 HERA

The HERA storage ring (*Hadron-Elektron Ringanlage*) in Hamburg, Germany operated between the years of 1992 and 2007. HERA was the home of four experiments– two colliders H1 and Zeus which used both of HERA's counter rotating proton and electron/positron rings, and HERA-B and HERMES (HERA Measurement of Spin) which were fixed target experiments. While HERA-B provided beam protons with a solid target, HERMES collided the 27.6 GeV electrons or positrons with a gas target. Though we may refer generically to this beam as "the electron beam", positrons were used more readily as they provide a longer beam lifetime having fewer interactions with beam gas and other ordinary matter. Many physics processes, and all of those of interest in this work are the same for both electrons and protons which differ only in the sign of their electric charge.

The electron beam is self-polarized by the Sokolov-Ternov effect. Although this effect can theoretically produce polarizations as high as 92.4% in an ideal ring, in practice the polarization is somewhat less. Due to focusing elements and beam-beam interactions in H1 and ZEUS as well as other non-ideal features of the accelerator, the beam polarization rarely exceeds 45%. The beam polarization is measured by a longitudinal polarimeter (LPOL) and a transverse polarimeter (TPOL) situated opposite sides of the ring. While the beam self-polarizes perpendicular to the

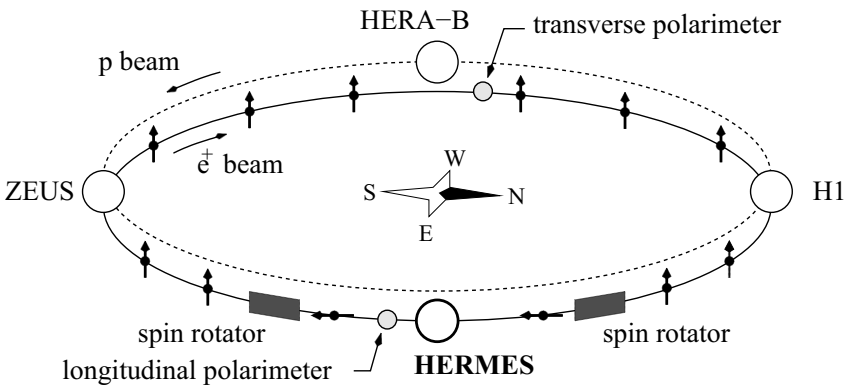

Figure 2.1: Schematic depiction of the HERA accelerator and the locations of its four experiments. The electron beam is polarized vertically by the Sokolov-Ternov effect but is rotated to and from the longitudinal orientation by a pair of spin rotators near the East Hall which contains the HERMES experiment. [16]

orbital plane, spin rotators on either side of HERMES rotate the polarization to and from the longitudinal orientation with respect to the beam's trajectory. The orientation of the beam polarization and positions of the polarimeters are depicted in Figure 2.1.

HERA typically injects electrons to currents ranging from 30-50mA and dumps the beam at 10mA.

2.2 The HERMES Target

The HERMES target cell [17] is an ultra-pure aluminum tube, elliptical in cross section and $\sim$100μm thick, through which the electron beam passes. Its dimensions are $\sim$ 3cm $\times$ 1cm $\times$ 40cm. It is fed polarized gas from the Atomic Beam Source (ABS) and is open on either side to allow a powerful system of pumps to maintain the beam line vacuum away from the HERMES target. The target density is approximately 10^{14} nucleons/cm^2 (integrated over the length of the target cell). This setup is shown in the schematic on the right of Figure 2.2. A collimator upstream of the target cell protects the cell from intense synchrotron radiation that can be produced in the beam line. Particles produced inside the HERMES acceptance exit the target chamber through thin (0.3 mm) stainless-steel exit window.

The typical luminosity can be calculated,

$$\begin{aligned} \mathcal{L}_{\rm unp} &\approx I \times \rho_{\rm unp} \quad 2 \times 10^{32}\ {\rm cm}^{-2}{\rm s}^{-1} \\ \mathcal{L}_{\rm pol} &\approx I \times \rho_{\rm pol} \quad 2 \times 10^{31}\ {\rm cm}^{-2}{\rm s}^{-1}, \end{aligned} \tag{2.1}$$

where I is the beam current (in electrons/sec) and ρ is the target density(in nucleons/cm^2).

Using a sophisticated Stern-Gerlach configuration of magnets, the ABS can produce target

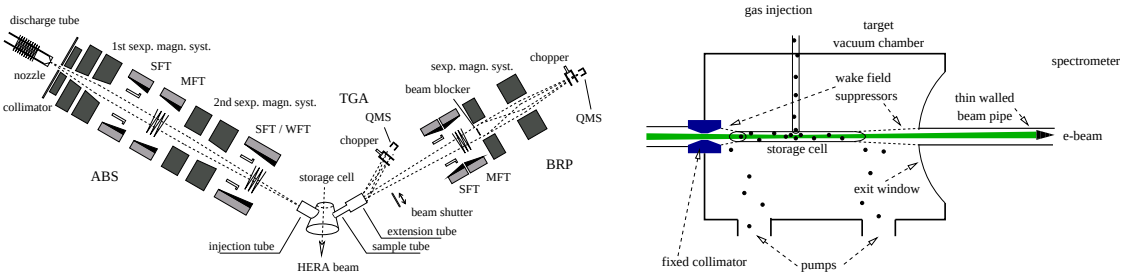

Figure 2.2: (Left) A schematic diagram of the atomic beam source (ABS) which uses a Stern-Gerlach configuration of magnets to select a particular polarization state. A Breight-Rabi (BRP) polarimeter samples the gas and measures its polarization. (right) A cut-away diagram of the target chamber which contains a target cell through which the beam passes and into which polarized gas is injected.[16]

polarizations as high as 90% and can control all combinations of nuclear and atomic spin of the target gas. An illustration of the ABS/target polarimeter configuration can be seen in the left panel of Figure 2.2. The target polarization is monitored by sampling target gas using a Breit-Rabi polarimeter to determine the relative populations of the various hyperfine states of hydrogen or deuterium atoms. From this the polarization can be computed.

2.3 The HERMES Spectrometer

The HERMES spectrometer (Figure 2.3) has an opening angular acceptance of $\theta_x = \pm 170$mrad and $\theta_y = \pm 140$mrad. This angular acceptance corresponds directly to the desirable kinematic range of the physics for which HERMES was designed. This correspondence will be seen clearly in Figure 3.6 of the next chapter. At the heart of the spectrometer is a 1.5 T·m magnet. The momentum dependant deflection of a charged particle traveling through the magnetic field is measured using the tracking detectors and hence each track's momentum is reconstructed. As the beam pipe passes through the opening between the upper and lower halves of the magnet a heavy iron septum plate shields the beam from the magnetic field.

The detector components of the spectrometer can be roughly divided into the following subsystems:

2.3.1 The Trigger and the DAQ

A trigger is a signal produced by a logical combination fast detector signals which lets the data acquisition system (the DAQ) know to readout the state of the spectrometer and record the event on disk. Optimally the HERMES DAQ records events at approximately 300Hz. Above this rate, events begin to be rejected as the system is frequently busy recording a prior event.

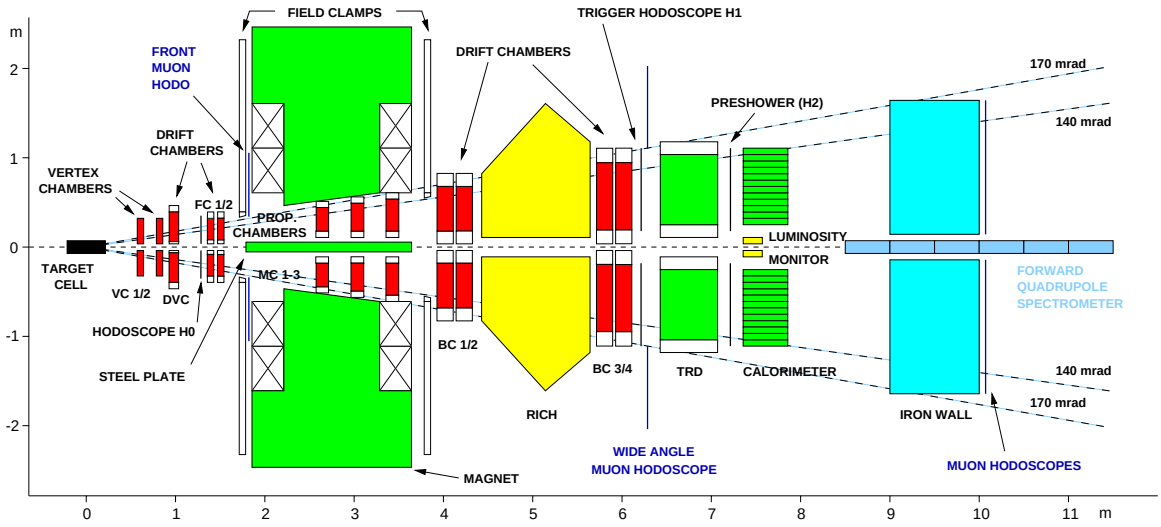

Figure 2.3: Side view of the HERMES spectrometer. The HERA electron beam pipe passes through the spectrometer's center shielded from the spectrometer magnet by a massive iron plate and an additional correction coil. The spectrometer is top-bottom symmetric which aids in controlling systematic uncertainties.

There are two primary triggering detectors:

Electromagnetic Calorimeter The main purpose of the calorimeter is to provide a trigger signal for scattered beam electrons. Each half of the calorimeter is composed of 420 $9 \times 9 \times 50$ cm^3 lead-glass blocks. This provides 18 radiation lengths of stopping power for electrons. Each block has a photomultiplier tube attached to its back face which quickly provides a signal reflecting this energy deposition.

Trigger Hodoscopes There are three planes of trigger hodoscopes, H0, H1, and H2. H0 is in the front region; H1 and H2 are in the back. Each hodoscope system consists of 42 vertical modules in each half of the detector. Each module consists of a panel of plastic scintillator material with a PMT fixed to the end. The modules are staggered in such a way that there is 2-3 mm overlap between panels.

A sample of HERMES triggers is provided in Table 2.1.

2.3.2 Tracking

The role of the tracking detectors is to provide precise position information about particles that pass through their active volume. This is accomplished primarily through the drift vertex chambers (DVCs), front chambers (FCs) and back chambers (BCs). Each of these chambers is comprised of two sets of three planes of wires each strung in a different orientation, vertical (0°), +30°, and −30°. Field wires and cathode planes are kept at large electric potential $\sim$ 1kV so that when a high-energy charged particle passes through the chamber gas in the detector volume it

Number	Logic	Description
21	$(\texttt{H0T} \times \texttt{H1T} \times \texttt{H2T} \times \texttt{CALOT}) + (\ \texttt{H0B}\ \ldots\ )$	Main physics trigger. Requires a single track– top or bottom. Calorimeter req. to select leptons.
17	$\texttt{H0} > 8 \times (\texttt{H0B} \times \texttt{H1B} \times \texttt{H2B} \times \texttt{BCB})$ $\times(\texttt{2H0T} \times \texttt{2H1T} \times \texttt{2H2T} \times \texttt{2BCT})$	Selects three track events with two in top half, one in bottom.
27		As above, but two bottom, one top.
9	$(\texttt{LUMI} > 25\text{GeV}) \times (\texttt{!GMS})$	Selects elastic scattering.
18	$(\texttt{H1T} \times \texttt{H2T} \times \texttt{CALOT}) + (\ \texttt{H1B}\ldots)$	A calibration trigger for H0 which can be compared with Trigger 21.

Table 2.1: A sample of important physics and calibration triggers generated by different combinations of the hodoscopes, H0, H1, H2, calorimeter, CALO, back chambers, BC, and luminosity monitor, LUMI. B and T refer to bottom and top respectively. A number preceding a detector name represents the number of hits required in that instrument.

causes an avalanche of electrons which drift toward grounded sense wires. The time interval between the trigger signal and various sense wires in different planes picking up the signal provide precise position reconstruction of the track.

2.3.3 Particle Identification

There are several subsystems responsible for particle identification. While the technical details of making these discriminations will be left for the next chapter, the relevant detectors – those which have a different response for leptons and hadrons – are the following:

Calorimeter While we considered the calorimeter previously in it's capacity as a triggering detector, it also plays an important role in lepton/hadron separation. The lead nuclei in the calorimeter glass cause the light electron to deposit virtually all of its energy through radiation. $E/p \approx 1$ for electrons, where E is the energy measured in the calorimeter and p is the momentum determined through tracking. Heavier particles, hardly influenced by these high-z nuclei, will only deposit a minimal ~ 1 GeV minimum ionizing pulse and thus producing little response in the detector. Even in the case of a *hadronic shower*, a strong interaction between the hadron and the detector material causing many new hadrons to be produced, the number of photons created is still small.

Preshower Detector The preshower detector is a lead curtain combined with the H2 hodoscope described previously. For reasons similar to the electron's behavior in the calorimeter, it will produce bremsstrahlung in the lead curtain which begins an electromagnetic shower (pair production from radiated photons) which cause multiple hits in H2. Hadrons, being significantly heaver are unlikely to radiate in the lead and produce a single pulse in H2.

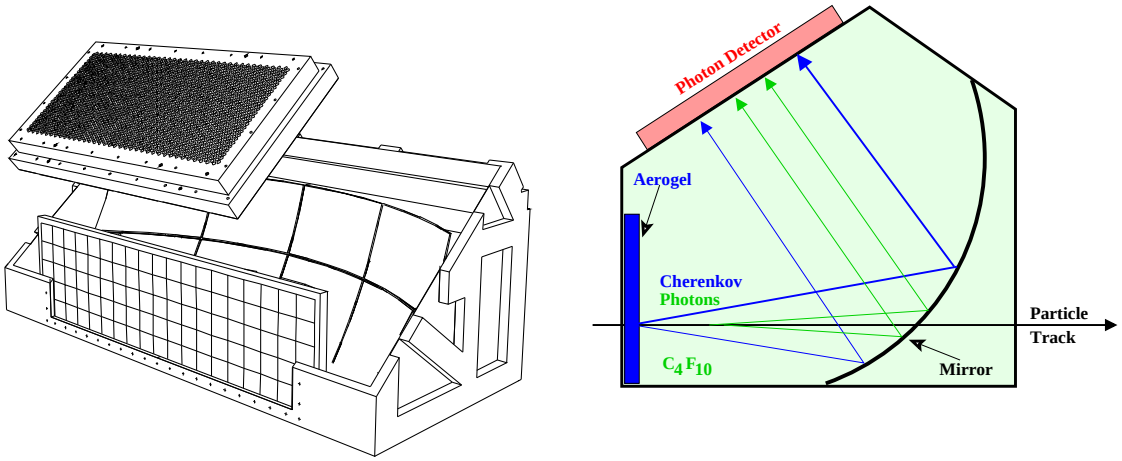

Figure 2.4: (Left) An illustration of one half of the Ring Imaging Čerenkov detector (RICH). (Right) A cutaway diagram showing the formation of rings in the PMT array via cones of Čerenkov light produced in the two radiator materials.

Transition Radiation Detector This detector is a volume packed with polyethylene fibers which are intended to produce *transition radiation*. When a particle crosses a threshold between different materials of differing refractive indices, it has a likelihood of radiating a photon which is roughly proportional to E/m, its energy divided by its mass. An electron produces many photons as it traverses the fiber-packed volume which pair produce and create a large signal in the six TRD wire planes. For hadrons, very little signal is produced.

Čerenkov Detector/RICH A final and particularly critical pair of detectors were the threshold Čerenkov counter which was used in 1996-1997 and the Ring Imaging Čerenkov (RICH) which replaced it in 1998 (and for all later years). In addition to providing a signal contributing to lepton/hadron discrimination, these detectors have the ability to distinguish hadrons from one another (which will be essential for our semi-inclusive analysis). They operate on the principle that when a charged particle exceeds the speed of light in a medium, it produces an electromagnetic shockwave or *Čerenkov light*. Both the number of photons produced and the opening angle of the cone are a function of the *speed* of the particle and become non-zero suddenly as a certain mass-dependant momentum threshold is crossed. Both of these detectors work by collecting Čerenkov light produced in a carefully selected medium and reflecting it into an array of PMTs. The threshold Čerenkov had only one radiator material and counted photons. Because of this, it was capable of separating pions from heavy hadrons in the momentum range of 4-13.6 GeV. The number of photoelectrons N_γ as a function of momentum can be seen in Figure 3.1 of the next chapter. The upper momentum cutoff is the result of the kaon threshold being crossed, at which point the detector can not discriminate pions from kaons.

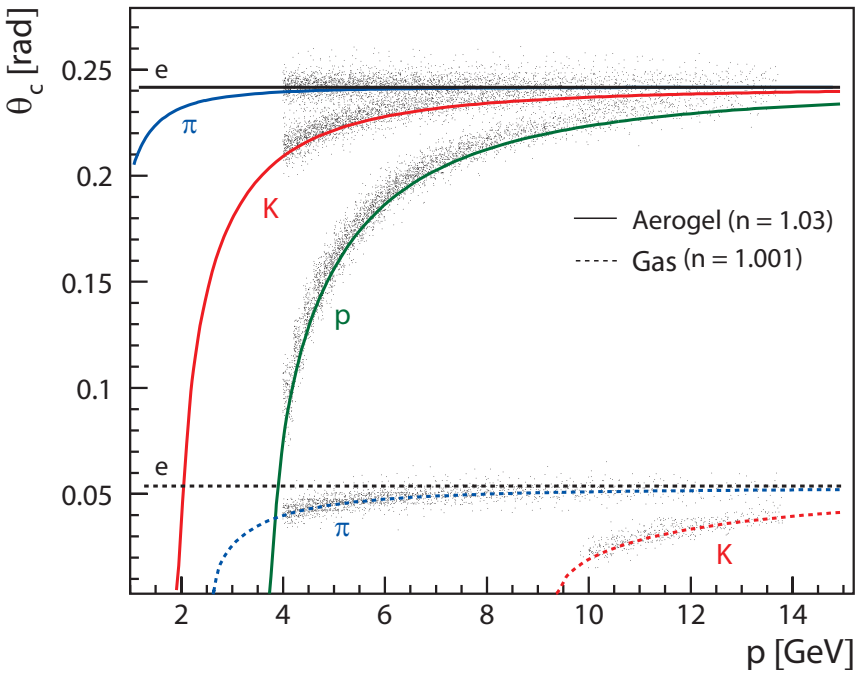

Figure 2.5: A scatter plot showing angular dependence of RICH photons as a function of hadron momentum. Theoretical curves are overlaid for each hadron type and radiator material. One can see that by imaging rings from each radiator material, a full pion, kaon, and proton discrimination can be made.

The RICH was designed with two carefully selected radiator materials, aerogel (the solid with the lowest refractive index, $n = 1.03$) and C_4F_{10} (the gas with the highest refractive index, $n = 1.0014$). Figure 2.4 gives a picture of one half of the RICH and also provides a cartoon indicating the way in which the rings are produced and imaged. As one can see in Figure 2.5, with two radiator materials, each particle type can be differentiated over the momentum range 2-15 GeV.

2.3.4 The Luminosity Monitor

Many measurements at HERMES are made by comparing two quantities. In our case, this will be two yields in different beam-target spin configurations. In order to properly normalize these samples, a measure of the relative luminosities of the two samples is necessary. This is accomplished with a pair of small calorimeters each with 12 blocks, placed along side the beam pipe. The purpose of this is to measure the rate of either Bhabha scattering (elastic $e^+e^- \to e^+e^-$) or Møller scattering (elastic $e^-e^- \to e^-e^-$) from atomic electrons, depending on the beam charge. As these processes have very well known cross sections, the luminosity can be determined. We will use the luminosity monitor rate in the next chapter (Section 3.4.1) to calculate the integrated luminosity for each of our samples.

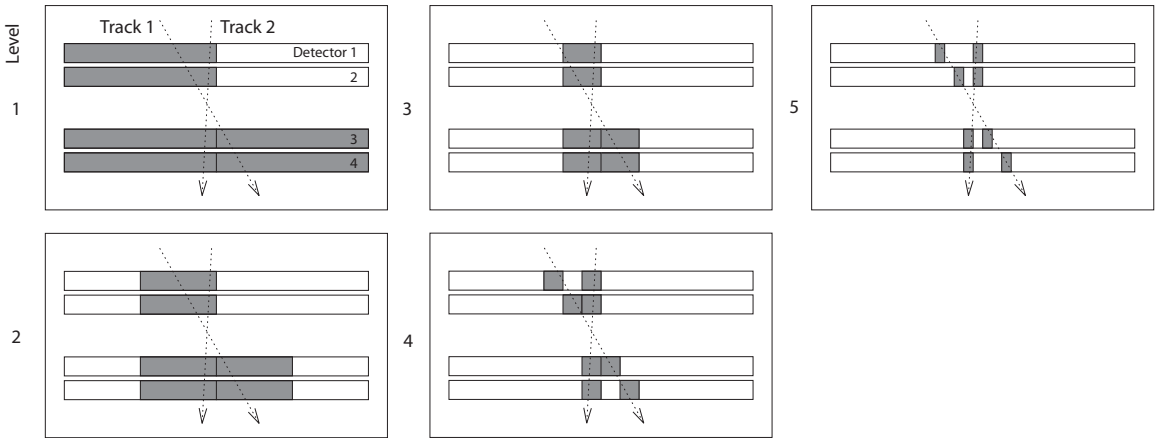

Figure 2.6: An illustration of the HERMES fast pattern recognition algorithm for track identification [14]. Tracking occurs rapidly through an iterative database lookup of possible track hit patterns at different levels of resolution.

2.4 Offline Data Production

The data that leaves the HERA East Hall is a relatively low-level readout of hits in the spectrometer and various other pieces of data related to running conditions. The offline data production is tasked with the job of organizing this information into convenient high-level (i.e. track, PID, momentum, trajectory) information. This job is divided into three sub-productions.

2.4.1 HRC Production

HRC, the HERMES event reconstruction package is responsible for processing event level data. This task involves interpreting hits in the various detector components as tracks and determining track momentum by connecting front and back tracks (up and downstream of the spectrometer magnet). This requires taking into account various calibrations, current magnetic field maps, and detector alignment measurements. Due to the large number of events to reconstruct and their complexity, this code must be highly efficient. Even carefully optimized, the HRC production can take several months to produce a year's data set.

The fast tree-search algorithm lies at the heart of the reconstruction code. Except for small variations in trajectory due to magnetic fringe fields and rescatterings, tracks on the front and back sides of the magnet are largely straight. The task of identifying an arbitrary number of tracks from hit patterns and discriminating them from background noise is challenging, particularly when efficiency is critical. Rather than trying to fit straight trajectories to the observed detector hits, the hit pattern is examined iteratively at increasingly refined resolution levels. This is depicted schematically in Figure 2.6. By matching the observed hit pattern to a small set of possible hit patterns, and then using that pattern to select a small set of possible daughter patterns, stored in an efficient tree-structure, the set of observed tracks can very quickly be arrived at through a very

Name	Length	Description
Fill	∼5 hours	Beam current reduced to where HERA must be dumped and refilled.
Run	>5 minutes	Time required to collect 500MB of data. Depends on beam current.
Burst	∼10 seconds	A unit of slow control time[1].
Event	∼None	Detector's response to a trigger. A single HRC reconstruction.

Table 2.2: Measurements of time at HERMES– from longest to shortest.

small number of calculations. For the purpose of track finding, this is accomplished in 11 steps (although it would require 14 to reach the full resolution of the spectrometer). Through symmetry considerations (translational, mirror image) the number of stored patterns can be greatly reduced– only ∼50,000 need be stored of a possible $\sim 10^8$ patterns.

2.4.2 Slow Production

The offline *Slow Production* is the compilation and synchronization of data that changes on a slow time scale with respect to the very fast event rate. Typically, slow data changes burst-by-burst which occurs on an $O(10\text{s})$ time scale. Table 2.2 provides a guide to different common time intervals used in the HERMES experiment and particularly around the offline production. Burst-level data includes (among other things) polarization measurements, target pressure, the luminosity monitor rate, various data quality and calibration information returned from their respective detectors, tracking efficiencies, high-voltage levels, and detector status data. Some of this data comes directly from the online slow production, some comes from other servers, and some must be processed by detector experts who perform analytic fits.

There is also a sizable data-quality aspect to the slow production. Many of these data streams must be checked, fill-by-fill to make sure the respective detector was operating normally and that any analytic fits to detector data are in adequate agreement with their underlying data points.

2.4.3 μDST Production

The μDST production is named after its final analyzable database files (`.udst`– for *small* Data Summary Tape). Several tasks are performed at this stage. Some of the functions of the μDST are to:

- Combine the final HRC and the slow files.
- Integrate more processed data from detector experts into the data stream.
- Eliminate unnecessary data from the HRC files and store the remaining data efficiently.

[1]Occasionally $O(5\text{ min})$ a burst is divided by a target polarization flip into a *split burst* which results in three sub-bursts. One sub-burst is produced for of each polarization and one for the short undefined state while flipping.

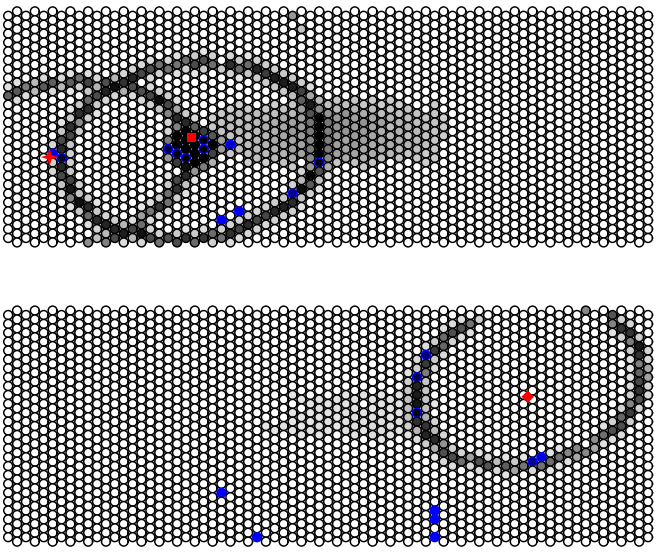

Run: 12345	Event: 57596924		
Particle (MType)	1	2	3
Momentum(GeV/c)	2.30	3.41	1.19
IRT Type	Pion- (B)	Pion- (B)	Pion+ (B)
IRT rqp	3.8	8.4	4.0
DRT Type	Pion-	Pion-	Pion+
DRT rqp	0.0	6.6	3.2
EVT Type	Antiproton	Pion-	---
EVT rQp	0.6	3.8	0.0
Position	Top	Top	Bottom

Figure 2.7: The RICH EVT algorithm's interpretation of a three track event. Track locations are indicated in red. The EVT algorithm generates hypothetical hit patters (gray) based on the possible hadron identities (dark grey bands) and a simulated background pattern (light gray haze). Hits in the RICH are indicated in blue. The hypothetical patterns are compared with the hit locations to select the most likely hadron identity.

- Perform additional processing such as running particle identification algorithms. An example of this is the RICH EVT algorithm whose output for an event can be seen in Figure 2.7. The algorithm simulates a hit pattern for each hadron identity hypothesis and compares them with observed RICH hits to determine the most likely particle identity .

The final `.udst` files contain relational database tables with records describing each burst, event, and track all linked in such a way that analyzers' analysis codes can easily and efficiently extract desired information. Before a μDST production is released, it must scrutinized by the Data Cops.

2.4.4 Data Cops

The Data Cops play a crucial role in integrating all available information about data quality producing a burst-by-burst list of various quality related attributes which analyzers use to accept or reject bursts in their analysis codes. These criteria are listed in Table 3.8 of the following chapter. In addition to scrutinizing many aspects of the final μdst files, they consider the run-by-run status information provided by the shift crew as well as logbook entries that could contain information about events that could jeopardize data quality.

Chapter 3

Data Analysis

This chapter describes the process by which the individual events and tracks contained in the HERMES μDST (micro Data Summary Tape) files are interpreted, selected or rejected, and ultimately counted in various kinematic bins to produce yield histograms of a particular data quality and particle identity. Furthermore, we will examine the kinematic selection criteria that constrain our data sample to a region in which incoherent interaction with a single parton and a factorizable fragmentation process are believed to be good descriptions of the underlying physics.

3.1 Particle Identification

As events at HERMES are well separated in time ($\sim 10^2$ Hz event rate vs. $\sim 10^7$ Hz bunch-crossing rate), track records in the μDST files are grouped into events. The first task then is to determine the species of each track in the event.

3.1.1 Lepton-Hadron Separation

Much of the data that is available in a DIS event is contained in the energy and momentum of the scattered beam lepton. HERMES data were collected with both electron and positron beams; the term lepton will be used hereafter for brevity. Additionally, *all* of the semi-inclusive information that we are interested in computing for the final state hadrons is ultimately dependent upon the scattered beam lepton to establish the q-vector of the virtual photon which provides a reference energy and orientation for the event. Because of this, a first critical step in the interpretation of a DIS event at HERMES is to distinguish lepton tracks from hadron tracks.

As described in Chapter 2, lepton-hadron discrimination is accomplished by combining responses from a number of different instruments. This identification is made by 1) the TRD, 2) the calorimeter, 3) the preshower detector, and 4) either by the threshold Čerenkov counter or by

the RICH depending upon the year.

The signals from these detectors are included in the data files for each track as a number of *PID* variables. These are defined for detector D:

$$PID_D \equiv \log_{10} \frac{P_(\ \mathcal{R}_D|\text{lepton}\ )}{P(\ \mathcal{R}_D|\text{hadron}\ )}, \tag{3.1}$$

where $P(\mathcal{R}_D|\text{lepton(hadron)}))$ is the *conditional probability* that the detector would produce response $\mathcal{R}_D$ given a track of a certain identity (lepton(hadron)). These conditional probabilities characterize the performance of the detectors and are termed *parent distributions*.

We are interested, however, in knowing the likelihood of a particular true particle species *given* the PID_D value returned by the detector. Using Bayes' theorem, this probability can be written:

$$P\,(\ \text{lepton}\,(\text{hadron})\,|\mathcal{R}_D\ ) = \frac{P\,(\ \mathcal{R}_D|\text{lepton(hadron)}\ )\ P\,(\ \text{lepton(hadron)}|p,\theta\ )}{\sum_{i=\text{lepton,hadron}} P(\ \mathcal{R}_D|i\ )\ P(\ i|p,\theta\ )}, \tag{3.2}$$

where $P(\ \text{lepton(hadron)}|p,\theta\ )$ is the probability that a track of a given momentum p and polar angle θ is a lepton(hadron) independent of the PID subsystem's response.

To compute $P(\ \text{lepton(hadron)}|\mathcal{R}_D\ )$, the hadron-lepton flux factor, $\Phi(p,\theta) \equiv \frac{P(\ \text{hadron}|p,\theta\ )}{P(\ \text{lep ton}|p,\theta\ )}$, is used. This factor is computed and made available in a set of tables for each year. These tables are computed by PID experts at HERMES using an iterative technique by which responses of the different PID subsystems are compared with one-another. The flux factor is determined through successive adjustments that ultimately bring the PID subsystems into agreement. Applying this process separately for each year's dataset helps to control uncertainties associated with the aging of the experimental apparatus.

Practically speaking, in addition to the aforementioned flux-factor, lepton-hadron discrimination is performed using two distinct PID values:

$$\text{PID3} \equiv \text{PID}_{Calo} + \text{PID}_{Pre} + \text{PID}_{Cer|RICH} \tag{3.3}$$

$$\text{PID5} \equiv \text{PID}_{TRD}. \tag{3.4}$$

These quantities are combined as follows:

$$\text{PID3} + \text{PID5} - \log_{10}(\Phi(p,\theta)) = \log_{10}\left[\frac{P(\ \mathcal{R}_{3+5}|\text{lepton}\ )\ P(\ \text{lepton}|p,\theta\ )}{P(\ \mathcal{R}_{3+5}|\text{hadron}\ )\ P(\ \text{hadron}|p,\theta\ )}\right] \tag{3.5}$$

$$= \log_{10} \frac{P(\ \text{lepton}|\mathcal{R}_{3+5}\ )}{P(\ \text{hadron}|\mathcal{R}_{3+5}\ )}. \tag{3.6}$$

One nice feature of this logarithmic definition is a simple interpretation of the resulting value. A positive value corresponds to a detector response more consistent with a lepton, while a negative

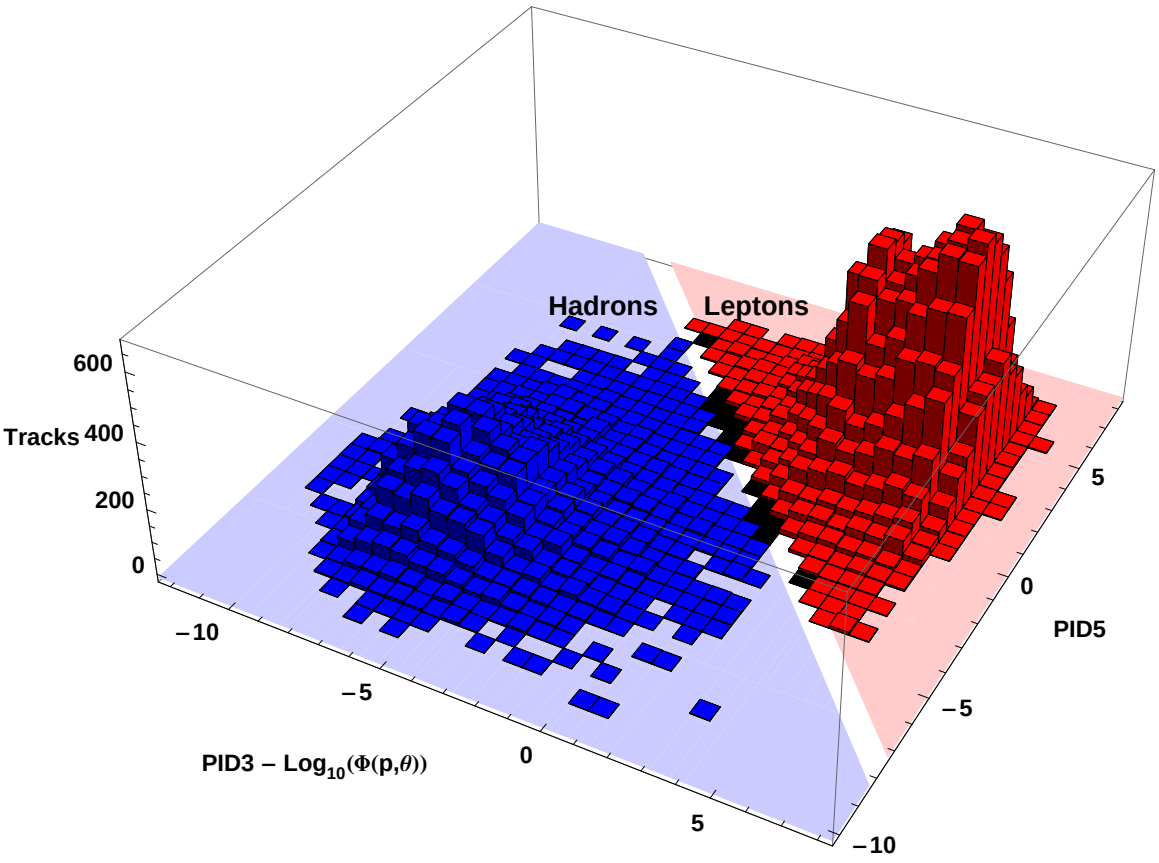

Figure 3.1: Histogram produced from a small sample of events from the 1996 dataset. Lepton tracks (red) are identified by the requirement that PID3 + PID5 - $\log_{10}(\Phi(p,\theta)) > 1$. Tracks in the region PID3 + PID5 - $\log_{10}(\Phi(p,\theta)) < 0$ are identified as hadrons (blue). The intermediate region contains a handful of events which are not well identified and are hence rejected from the data sample (black). This two-dimensional histogram also highlights the importance of combining the PID3 and PID5 signals as separation is considerably better than using either projection alone.

Year	Beam	Target	Hadron ID
1996	e^+	H_2	Threshold Čerenkov
1997	e^+	H_2	Threshold Čerenkov
1998	e^-	D_2	RICH
1999	e^+	D_2	RICH
2000	e^+	D_2	RICH

Table 3.1: Experimental configuration by year including beam and target species and hadron identification apparatus.

value represents a response more consistent with a hadron. It follows, then, that a zero value corresponds to a detector response equally constant with either hypothesis.

In this analysis, tracks for which $PID3 + PID5 - \log_{10}(\Phi(p,\theta)) > 1$ are taken to be leptons, those for which $PID3 + PID5 - \log_{10}(\Phi(p,\theta)) < 0$ are taken to be hadrons, and tracks falling into the intermediate region are rejected as they are not well differentiated. The lepton cut is somewhat more stringent than that for the hadron. Because an event can be generated by many different kinds of triggers (which are produced fairly liberally), many events contain no scattered lepton. The more stringent lepton requirement serves to clean up this somewhat dirty raw event stream. Additionally, it is generally unlikely to find more than one lepton in an event, so once a lepton is selected, the hadron criterion can be less stringent. Figure 3.1 provides a sample of the distribution of PID3 and PID5 values and indicates the boundaries used to differentiate tracks of different identities.

In this analysis, the highest-momentum beam-charged lepton track is taken to be the scattered beam lepton. One might alternatively consider analyzing and counting the event for *each* lepton in the event. In practice, however, the likelihood of two leptons occurring in an event with suitable inclusive kinematics is sufficiently small that the difference in particle yields is negligible.

3.1.2 Hadron Identification

As described previously, of the five years of running with longitudinally-polarized H and D targets, hadron identification was performed using a threshold Čerenkov detector for the first two and by the ring imaging Čerenkov detector (RICH) that replaced it for the latter three (Table 3.1).

The Threshold Čerenkov (1996-1997)

Interpreting the response of the threshold Čerenkov counter is relatively straightforward. Each track in the data files has an entry which corresponds to the number of photons, N_γ, in the Čerenkov associated with that track. As described in section 2.3.3, the number of photons produced by Čerenkov radiation is a function of the momentum and mass of a particle. Moreover, there is a characteristic threshold momentum for each type of particle below which no photons are

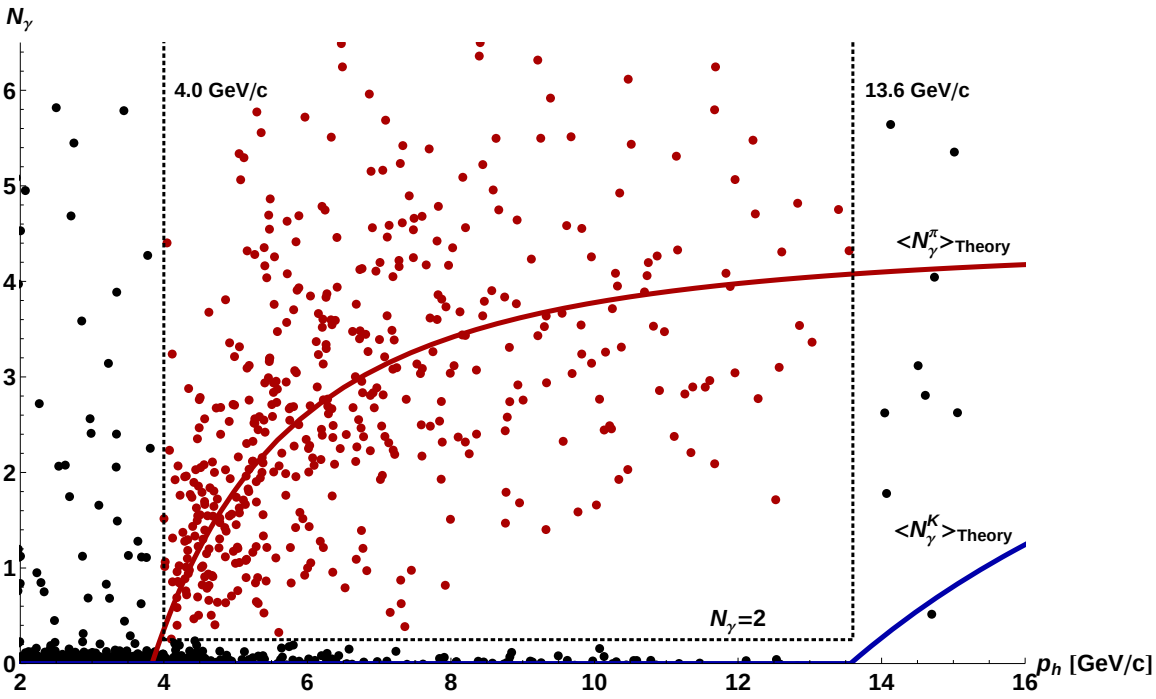

Figure 3.2: The threshold Čerenkov counter's response to a small sample of hadron tracks from 1996. Theoretical curves for $< N_\gamma^\pi >$ and $< N_\gamma^K >$ computed from the refractive index of the medium are superimposed. Their asymptotic values for $N_\gamma^{\max}$ come from measurements of the response to the highly relativistic electron sample. The dotted line represents the boundary of the region identified as pions.

produced. N_γ asymptotically approaches a maximum photon count above this threshold. The curve in figure 3.2 shows the theoretical mean of N_γ as a function of momentum produced using a measured refractive index for the medium. This is an *effective* refractive index as it is determined from the observed pion threshold which is also sensitive to detector efficiency and acceptance.

This detector was designed to distinguish pions from heavier hadrons. To do this, tracks (previously identified as hadrons) in a specific momentum range are selected. $p_h > 4$ GeV/c is required as this is just above the pion Čerenkov threshold. Below this value, the response, if any, would provide only very low-efficiency discrimination. $p_h < 13.6$ GeV/c is also required as above this, the kaon threshold is reached and the pion sample becomes contaminated. Finally, $N_\gamma > 0.25$ is required to select pion tracks that are well differentiated from the noise associated with heavy hadron tracks that produce little or no response in the detector. The box created by these three cuts can be seen in figure 3.2.

The RICH (1998-2000)

The dual-radiator ring imaging Čerenkov (RICH) detector replaced the threshold Čerenkov counter in 1998. Because of its carefully selected radiator materials, it has the ability to differentiate pions, kaons, and protons over the momentum range 2 GeV $< p_h <$ 15 GeV. Unlike

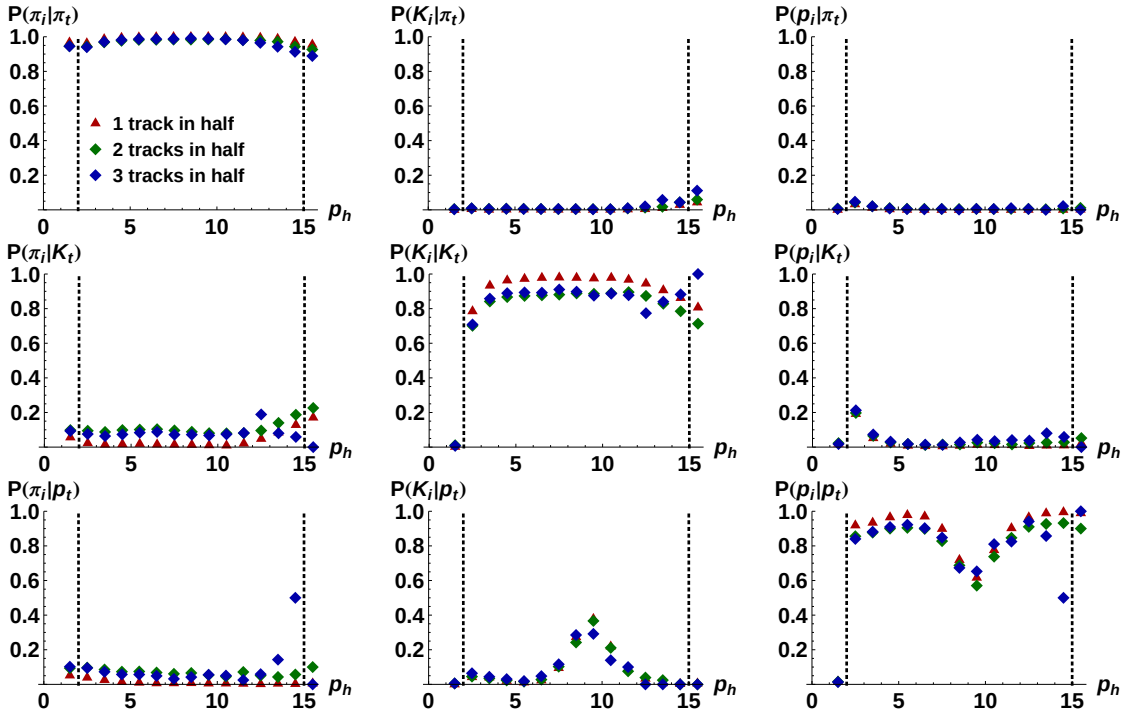

Figure 3.3: The P-matrix represents the conditional probability that a hadron of true type h_t will be identified by the RICH as type h_i. The distinct bumps in the kaon and proton probabilities are caused by misidentified kaons at the kaon gas-radiator threshold where N_γ is small.

the threshold Čerenkov, where a hadron track is designated *either* a pion or a heavier hadron, with the RICH, a probability is produced for each of the three possible hypotheses: pion, kaon, or proton. As described below, weights are calculated for each hypothesis and fractional counts are then recorded in yield histograms during data analysis.

While the RICH produces a single favored hypothesis for each track, a *P-matrix* is provided by the HERMES RICH group which is used to produce weights for all different hypotheses, providing more accurate yields. The P-matrix contains the conditional probabilities, $P(h_i|h_t)$ that a hadron of true identity, h_t, is identified by the RICH as being of type h_i. The P-matrix is produced by comparing RICH-identified Monte Carlo tracks with their true identities and is binned in the two variables on which it has been found to depend: track momentum, and the multiplicity of tracks in the relevant half of the detector. The probability entries of the P-matrix are plotted in figure 3.3.

Using the P-matrices, one can write:

$$\vec{N}_i = P\ \vec{N}_t, \tag{3.7}$$

where,

$$\vec{N}_i = \begin{pmatrix} N_i^\pi \\ N_i^K \\ N_i^p \end{pmatrix}, \ \vec{N}_t = \begin{pmatrix} N_t^\pi \\ N_t^K \\ N_t^p \end{pmatrix}, \text{ and } P = \begin{pmatrix} P(\pi_i|\pi_t) & P(\pi_i|K_t) & P(\pi_i|p_t) \\ P(K_i|\pi_t) & P(K_i|K_t) & P(K_i|p_t) \\ P(p_i|\pi_t) & P(p_i|K_t) & P(p_i|p_t) \end{pmatrix}, \tag{3.8}$$

$N^h_{i(t)}$ being an identified (true) yield of hadrons of type h. From equation 3.7, one can see then that a yield of identified hadrons can be mapped back to the true yield using the inverted P-matrix as follows:

$$P^{-1} \ \vec{N}_i = \vec{N}_t. \tag{3.9}$$

Because of this, the inverted P-matrix can be applied to the RICH's hypothesis (a yield vector, if you like, with a single one as it's only non-zero entry) to produce the vector of weights to be added to the final hadron yield histograms. It should be noted that unlike the P-matrix, its inverse P^{-1} (sometimes referred to as the *Q-matrix*) doesn't contain probabilities. Its entries need not be bounded by one and can also be negative.

The procedure for processing the RICH response for each track is as follows:

1. The `rQp` (RICH Quality Parameter) value is checked. `rQp` $\equiv \log_{10}(P(h_1)/P(h_2))$, where $P(h_1)$ and $P(h_2)$ are the probabilities of the RICH's first- and second-most-likely hadron hypotheses for the observed response pattern. Unless this value is zero, the RICH favors one hypothesis over another. If `rQp` is zero, more than one hadron type could have produced the observed pattern with equal likelihood. We reject the track in this case.

2. The `iType` value is checked. The value of this variable represents the hypothesis most favored by the response of the detector.

3. The inverted P-matrix is consulted to obtain the appropriate true pion, kaon, and proton weights for the observed `iType`, track momentum bin, and track multiplicity in detector half.

4. Finally, for each of the three possible hadron identities, kinematic variables that depend on the hadron's mass must be computed. This means that for certain semi-inclusive variables, z and x_F for example, the fractional counts for the different hadron hypotheses may be placed in different kinematic bins.

3.2 Data Selection

In addition to the responses of the PID detectors, the μDST files contain several parameters for each track including vertex position, vertex angle, momentum, charge, and the position and angle of the track leaving the spectrometer magnet. Once the lepton-hadron separation is complete and

a track is designated to be the scattered lepton, its momentum four-vector can be used to compute the kinematics of the hard-scattering vertex.

3.2.1 Inclusive Requirements

As described in Chapter 1, an inclusive DIS event is generally described as a function of two parameters. In fact, with a fixed beam energy, an inclusive event *can only be* a function of two variables. All parameters but the components of four-momentum of the scattered lepton are fixed, and two of those are constrained– the lepton mass constrains the energy and the magnitude of the three-momentum and azimuthal symmetry around the beam axis removes another degree of freedom. Q^2 and Bjorken-x are common choices and provide a fairly intuitive picture of the event.

Q^2 is defined to be the negative squared four-momentum carried by the virtual photon. It is calculated as follows:

$$\begin{aligned} Q^2 &\equiv -(k' - k)^2 \\ &\overset{lab}{=} 4\ E\ E'\ \sin^2(\frac{\Theta}{2}). \end{aligned} \tag{3.10}$$

The variable ν is defined to be the energy of the virtual photon: $\nu \equiv E' - E$. Using Q^2 and ν, one can calculate the parton momentum fraction, Bjorken-x:

$$x = \frac{Q^2}{2\ M_p\ \nu}. \tag{3.11}$$

y, the fraction of the beam's energy carried by the virtual photon and W^2, the invariant mass of the hadronic final state, are also computed.

$$y = \frac{E - E'}{E} \tag{3.12}$$

$$W^2 = 2M_p\nu + M_p^2 - Q^2 \tag{3.13}$$

These additional variables have particular physical meanings and while they are completely constrained by x and Q^2, allow us to place specific physical restrictions on our data sample.

The purpose of placing restrictions on these additional parameters is to ensure that the sample of events selected can be reasonably interpreted using the leading-order, leading-twist description of the interaction upon which we have constructed our analysis formalism and have defined our parton densities. An essential requirement is that the scattering event takes place *incoherently*, i.e., that the virtual photon probe is sufficiently energetic to interact with a single constituent of an otherwise frozen nucleon.

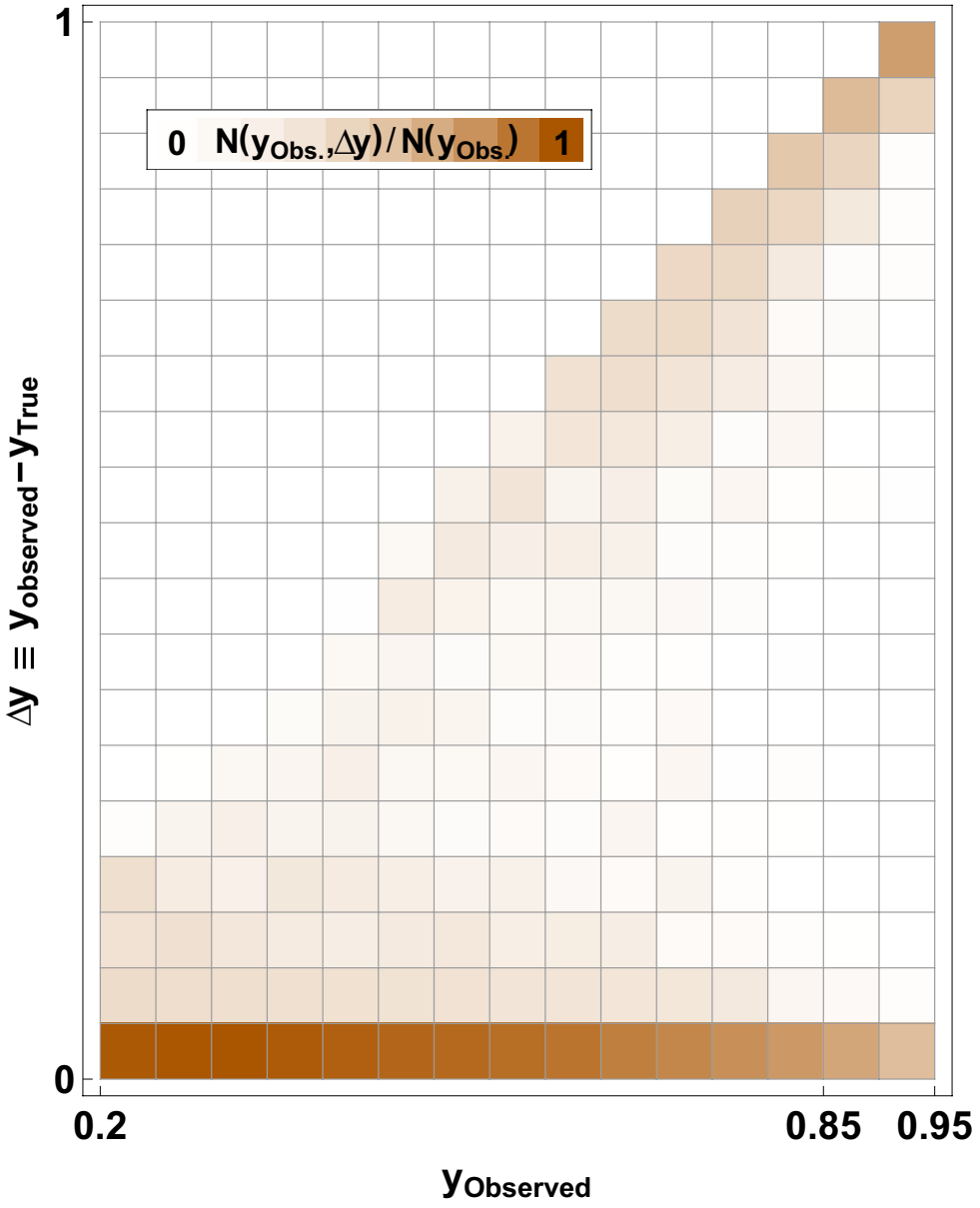

Figure 3.4: A Monte Carlo study showing the discrepancy between y_{true} and y_{observed} as a function of y_{observed}. QED radiation causes a pronounced discrepancy at large values of y_{observed}.

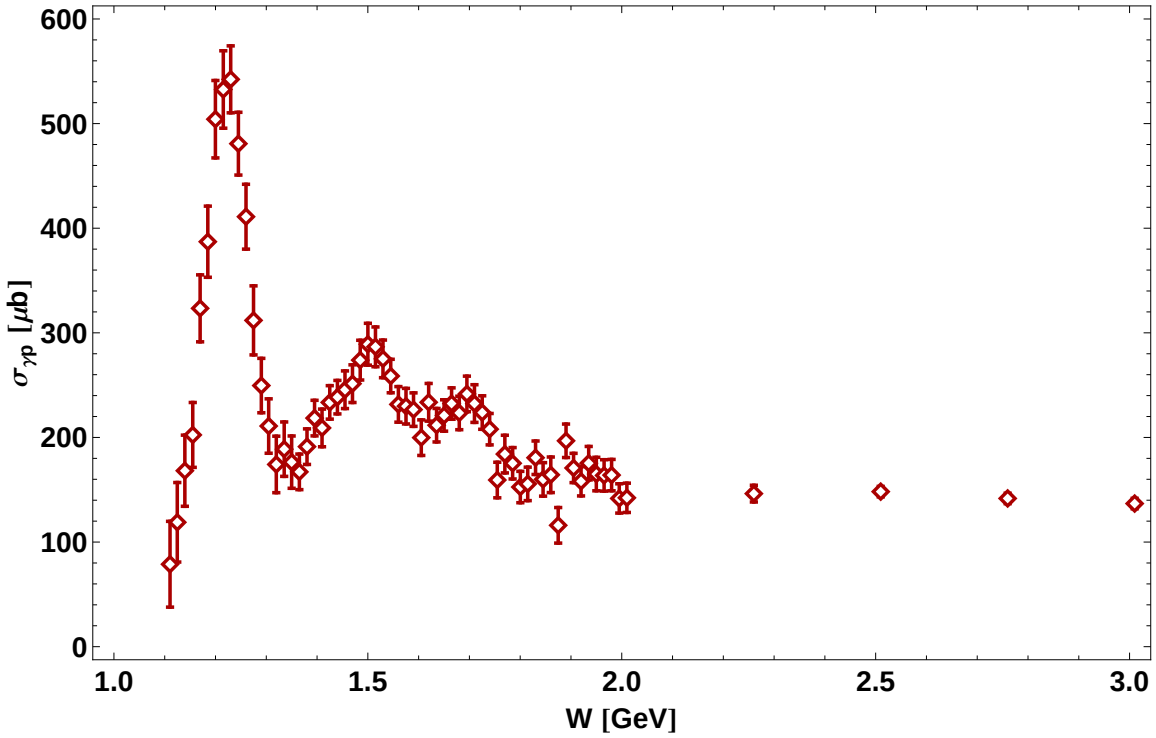

Figure 3.5: The γp cross section as a function of the final state invariant mass, W. The peaks represent coherent excitations of the proton. [18]

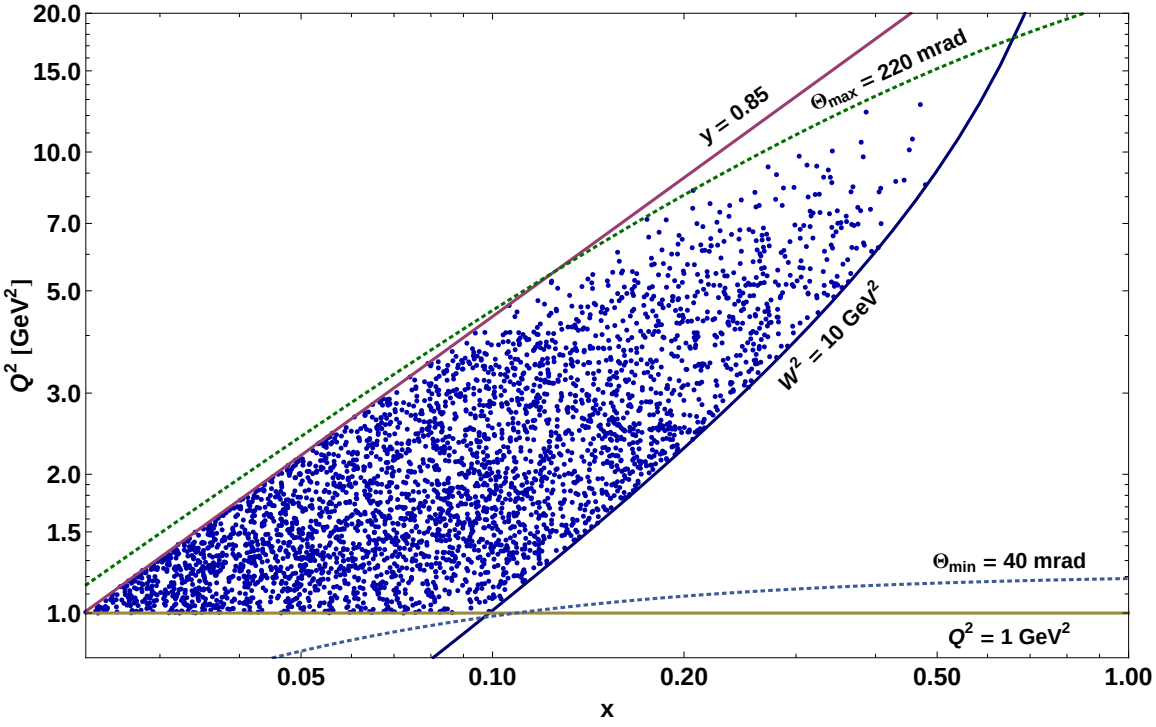

Figure 3.6: A sample of the x and Q^2 distribution of accepted DIS events. The dotted curves represent the maximum and minimum scattering angles in the acceptance of the HERMES spectrometer. The solid curves represent the various kinematic requirements for inclusive DIS events.

Variable	Requirement	Reason
Q^2	> 1 GeV^2	Virtual photon momentum of suitable scale to resolve the nucleon's substructure.
W^2	> 10 GeV^2	Exclude coherent resonances of the nucleon.
y	< 0.85	Large contribution from QED radiative effects at high-y.

Table 3.2: Inclusive kinematic requirements.

This requirement is first imposed through a $Q^2 > 1$ GeV^2 cut. Intuitively, this requirement guarantees that we have a probe of sufficiently small wavelength to resolve the substructure of the nucleon (whose mass and size correspond to ~ 1 GeV). More rigorously, perhaps, is that Q^2 represents the *scale* of the interaction. The larger this scale parameter is with respect to the characteristic energy of the nucleon, the better the hard-scattering (PDF dominated) part of this event is described by the non-interacting lowest order QCD process.

Secondly, we require $W^2 > 10$ GeV^2 to ensure that the final state mass is in the continuum region – well above the resonance region. The γP cross section as a function of W can be seen in Figure 3.5. Below W of 2 GeV or so, the spectrum shows the coherent excitation of nucleon resonances, such as the spin-3/2 Δ at 1.23 GeV and the Roper resonance at 1.44 GeV. As resonance excitation by the virtual photon is a coherent process, involving the entire substructure of the nucleon, it is not included in the single-parton scattering framework with which we interpret DIS events. A cut of $W^2 > 4$ GeV^2 rather than 10 GeV^2 was considered for the inclusive asymmetries in an effort to boost statistics, but it was found that the additional data was sufficiently depolarized (at the lepton–virtual-photon vertex) that its statistical influence was negligible. This will be discussed further in Section 4.1.2.

Finally, events for which $y > 0.85$ are rejected because of a significant contribution from QED radiative processes. Photons radiated from the lepton before or after the virtual photon is exchanged go unobserved and can cause significant miscalculations of event kinematics. Where these Bremsstrahlung effects are modest, a smearing correction will be made. At sufficiently large values of y, however, this contribution is large enough to warrant rejecting these events altogether. A Monte Carlo study of the accuracy of y_{observed} can be seen in Figure 3.4.

The inclusive requirements are summarized in Table 3.2. The kinematic region defined by these cuts can be seen in Figure 3.6 along with a sample of accepted events.

3.2.2 Geometric Requirements

Certain geometric requirements are placed on lepton tracks to ensure that they originate within the target cell and that the tracks before and after the spectrometer magnet are clear of obstructions (detector frames, magnetic field-clamps, and support structures) that might deflect

Variable	Requirement	Reason
$\lvert z_{vertex}\rvert$	< 18 cm	Lepton originated inside target cell.
r_{vertex}	< 0.75 cm	
p	> 0.5 GeV	Lower limit of spectrometer momentum acceptance.
x_{calo}	< 175 cm	Energy deposition inside of active calorimeter volume.
y_{calo}	> 30 cm	
y_{calo}	< 100 cm	
$x_{z\,=\,172\text{cm}}$	< 31 cm	Track inside front field clamp aperture.
$y_{z\,=\,181\text{cm}}$	> 7 cm	Track clears septum plate.
$x_{z\,=\,383\text{cm}}$	< 54 cm	Track inside rear field clamp aperture.

Table 3.3: Inclusive geometric requirements.

particles and contaminate the data sample. These requirements are termed fiducial volume cuts and are summarized in Table 3.3.

3.2.3 Semi-Inclusive Requirements

The constraints placed upon the hadrons are generally motivated by the desire to to have a sample in which the correlation between the observed hadron and a struck quark of a particular flavor is strong. When we extract the quark helicity densities in Chapter 6, the strength of this struck-quark, hadron-species correlation will play a central role in our ability to separate the quark polarizations by flavor. While the purity formalism we will employ makes no specific requirement for the degree to which the hadron sample contains leading hadrons – those which contain the struck quark itself – it will become clear that it is of substantial benefit if the connection to the struck quark can be strengthened without giving up many events. Our choice of semi-inclusive selection criteria, which are summarized in Table 3.4, will have a sizable impact on the precision of the final result.

Our primary means of enhancing this correlation is to select a fragmentation regime in which the *target* and *current fragmentation regions* – the regions containing or closely related to the target remnant and struck quark respectively – are well separated. In practice, since the HERMES detector is fairly insensitive to the recoiling target remnant (due to its geometry), this selection suppresses contamination by occasional remnant and remnant-related hadrons and serves to exclude ambiguous central hadrons, leaving behind a sample with a strong struck quark association.

The selection of the current region hadrons is accomplished through the application of two cuts:

z is the ratio of the energy carried by the hadron to that of the virtual photon:

$$z = \frac{E_h}{\nu} = \frac{\sqrt{p_h^2 + M_h^2}}{\nu}. \tag{3.14}$$

Variable	Requirement	Reason
z	> 0.1	Select a sample strongly correlated with struck quark.
	< 0.8	Reject exclusive events – not DIS.
x_F	> 0.1	Further emphasis on current fragmentation region.
z_{vertex}	> -18 cm	Exclude tracks originating behind the target cell.
z_{vertex}	< 100 cm	Include hadrons produced from downstream decays (e.g. K_s).
r_{vertex}	*none*	
$p_{\check{\text{C}}\text{erenkov}}$	> 4 GeV	Momentum cuts for hadrons defined by capabilities of identification apparatus.
$p_{\check{\text{C}}\text{erenkov}}$	< 13.8 GeV	
p_{RICH}	> 2 GeV	
p_{RICH}	< 15 GeV	

Table 3.4: Semi-inclusive requirements. The geometric cuts from Table 3.3 also apply to hadron tracks unless superceeded by values in this table.

We expect that the more energetic the final state hadron, the more strongly correlated it is with the struck quark. As z is a function of the mass of the hadron, it cannot be determined without hadron identification. For the case of the deuterium sample (1998-2000) when identification was performed by the RICH and a weight was provided for each of the hadron types, z was recomputed for each of the three hadron hypotheses. We require $z > 0.1$ to remove contamination from the poorly differentiated intermediate fragmentation which is weakly correlated with either the target or the remnant. Additionally, we exclude $z > 0.8$ as hadrons carrying all or most of the available energy are likely exclusive hadrons (a single hadron representing the entire final state). Exclusive hadron production, while a rich subject in itself, tends to be a coherent process which is fundamentally different from DIS – a process in which interacting with a single quark is of primary importance.

x-Feynman or x_F, computed

$$x_F \equiv \frac{p_{||}^{\text{cm}}}{|\vec{q}|} \overset{\text{lab}}{\approx} \frac{2P_h^{||\ CM}}{W}, \tag{3.15}$$

is a measure of which direction of the momentum a final state hadron points in the center of mass reference frame of the virtual photon target system; in the direction of the q-vector or of the target nucleon's velocity vector. x_F ranges from -1 to 1 and values greater than 0 are considered to be *forward* – in the direction of the q-vector and more associated with the struck quark. An $x_F > 0.1$ cut serves to eliminate hadrons in the intermediate region of ambiguous origin.

Bin	x_{low}	x_{high}
1	0.023	0.040
2	0.040	0.055
3	0.055	0.075
4	0.075	0.100
5	0.100	0.140
6	0.140	0.200
7	0.200	0.300
8	0.300	0.400
9	0.400	0.600

Table 3.5: 1-Dimensional x-Binning.

3.3 Binning

A major goal of this analysis was to explore different possibilities for bin selection in different combinations of variables. This was done both with the intent to extract as-yet-unexplored observables like $A_1^h(p_{h_\perp})$ and to enhance our statistical leverage on quantities which had been extracted in the past – $\Delta q(x)$, in particular.

The selection of bin widths and edges was motivated by three factors. First, some degree of uniformity in the number of counts in each bin is desirable. This allows us to present data with error bars that are of a similar scale though this is also a function of the quantity being computed from the yields. Second, bins weren't allowed to become so large that the average kinematics varied significantly from one side of the bin to the other. If this does occur, computing necessary kinematic quantities for large, sparsely populated bins can become inaccurate. Finally, for the case of the x-binning, there is a desire to produce results that can be compared easily to those produced in the past by other HERMES collaborators. Where reasonable, the x-binning is unchanged from prior analyses.

Ultimately, yields (and their associated asymmetries) are binned in three different ways.

Traditional: The first of these is the 1-dimensional, or *traditional*, x-binning. This binning is identical to that used in HERMES' prior 5-flavor $\Delta q(x)$ extraction [16]. It is described in Table 3.5.

Three-Dimensional Semi-Inclusive: A major goal of this analysis was to take advantage of semi-inclusive variables to better isolate hadrons whose identity is strongly correlated with the struck-quark flavor. In order to accomplish this, a Monte Carlo quark polarization extraction study was performed in order to identify which semi-inclusive variables, if any, would provide additional statistical leverage. This study, described in Section 6.1.4, indicated that when used in combination, adding z and $P_{h_\perp}$ dimensions to the traditional x-binning described previously would have just this effect. The additional semi-inclusive bin edges are

given in Table 3.6. The semi-inclusive yields thus have 81 bins each (9 $x \times 3$ $z \times 3$ $p_{h_\perp}$) while the inclusive yields still retain the nine traditional x bins.

Two-Dimensional x-$p_{h_\perp}$: This binning was used to produce semi-inclusive yields with 18 bins (3 $x \times 6$ $p_{h_\perp}$) mainly for computing the $p_{h_\perp}$ dependence of the A_1^h. Because x and $p_{h_\perp}$ are strongly correlated, without plotting these asymmetries in x-slices, there is a potentially misleading x-dependence in plots of $A_1^h(p_{h_\perp})$. The $p_{h_\perp}$ binning was selected because it distributes the statistics fairly well among the bins and gives as much of an opportunity as possible to see any $p_{h_\perp}$ dependence of the asymmetry. The bin edges are given in Table 3.7

3.4 Burst-Level Data Selection

The coarsest level of data selection occurs at the burst level. As described in the prior chapter, this provides data quality and luminosity information for intervals of approximately ten seconds at a time. Failure to meet any of the data quality criteria listed in Table 3.8 causes a burst to be rejected from the data set in all respects. All events from that burst are rejected and that burst's luminosity contribution is ignored.

3.4.1 Calculation of Luminosity

The *asymmetry* is the "bread and butter" of the HERMES experiment. By comparing yields in which a single feature of the beam-target configuration is switched back and forth, many systematic uncertainties – those that affect both configurations equally – cancel out. In addition, unlike when measuring a cross section, a perfectly calibrated, absolute measurement of the luminosity is unnecessary. However, for measuring asymmetries, knowing the *relative luminosity* of the data collected in the two beam-target spin configurations is essential for properly balancing yields.

The calculation of the luminosity is carried out using the response of the luminosity monitor described in Section 2.3.4. The following formula is used to calculate the luminosity for each burst:

$$\mathcal{L} \;=\; < R_{\text{lumi}} > \;\times\; C_{\text{lumi}}(\text{year}) \;\times\; A(\text{target}) \;\times\; \tau_{\,\text{DAQ-up-\%}} \;\times\; t_{\text{burst}}. \tag{3.16}$$

Here $< R_{\text{lumi}} >$ is the average rate measured by the luminosity monitor, C_{lumi} is a proportionality

z-Bin	z_{low}	z_{high}
1	0.10	0.35
2	0.35	0.50
3	0.50	0.80

$p_{h_\perp}$-Bin	$p_{h_\perp\ low}$ [GeV^2]	$p_{h_\perp\ high}$ [GeV^2]
1	0.0	0.3
2	0.3	0.5
3	0.5	2.0

Table 3.6: The the z and $P_{h_\perp}$ bin edges added to form a 3D binning.

x-Bin	x_{low}	x_{high}
1	0.023	0.55
2	0.55	0.10
3	0.10	0.60

$p_{h\perp}$-Bin	$p_{h\perp\ low}$ [GeV]	$p_{h\perp\ high}$ [GeV]
1	0.0	0.15
2	0.15	0.30
3	0.30	0.40
4	0.40	0.50
5	0.50	0.60
6	0.60	2.0

Table 3.7: The the x and $P_{h\perp}$ bin edges that form the 2D x-$p_{h\perp}$ binning.

Data Quality Flag	Burst Selection Criterion
0	Target spin parallel or antiparallel to beam.
1	Smoothed beam polarization $> 30\%$.
2	Reasonable DAQ deadtimes.
3	Reasonable burst lengths.
4	Beam current reasonably large.
5	Varies by year. Count rates or target density fluctuations reasonable.
6	First burst of each run rejected.
7	Last burst of each run and bursts with undefined DAQ state rejected.
8	Varies by year. Nominal DAQ or PID detector states.
9	Runs marked analyzable by shift crew.
10	Polarized target mode.
15	Polarized target mode (determined from valve state of target).
16	Target state good.
17	All calorimeter blocks good.
18	Hodoscope H2 pr Luminosity monitor are good.
19	TRD data quality good.
20	No high-voltage trips in wire chambers.
21	Various problems by year (target, tracking, calorimeter, or RICH).
22	No trips in RICH.
23	α_0 value is reasonable.
24	α_R value is reasonable.
25	Čerenkov or RICH data quality good.
26	Various. Either bad VC synchronization or target in tensor state.
27	Valid target polarization measurement by BRP.
28	Beam polarization measurement not older than five minutes.
29	Target magnet current in reasonable range.
30	Deadtime in reasonable range.
31	Varies by year. Reasonable α or middle calorimeter blocks good.

Table 3.8: Burst-level data quality requirements.

Year	DIS Events	Total Luminosity [pb^{-1}]	$\mathcal{L}_{\uparrow\uparrow}/\mathcal{L}_{\uparrow\downarrow}$
1996	485,350	12.42	0.999
1997	1,365,436	37.81	0.999
1998	905,796	24.72	1.020
1999	1,000,676	28.88	0.996
2000	5,116,184	139.47	0.999

Table 3.9: DIS event totals, approximate luminosity, and spin state comprison by year.

Year	$< P^{\text{targ}}_{\uparrow\uparrow} >$	$< P^{\text{targ}}_{\uparrow\downarrow} >$	$\delta P^{\text{targ}}/P^{\text{targ}}$	$< P^{\text{beam}}_{\uparrow\uparrow} >$	$< P^{\text{beam}}_{\uparrow\downarrow} >$	$\delta P^{\text{beam}}/P^{\text{beam}}$
1996	75.9	75.9	0.055	52.8	52.8	0.034
1997	85.0	85.0	0.038	52.9	52.9	0.034
1998	85.6	85.6	0.075	51.5	51.5	0.034
1999	83.2	83.2	0.070	53.4	53.4	0.018
2000	85.1	84.0	0.035	53.1	53.7	0.019

Table 3.10: The magnitude of the average percentage target and beam polarization for each spin state and their fractional uncertainties by year. These target polarization numbers were provided by the target group and used as such in this analysis. The yearly beam polarizations were calculated as a burst-by-burst sum of the product of beam polarization and luminosity and then divided by the total luminosity for each year (i.e. $< \mathcal{L} P^{\text{beam}}_{y\ s} > / < \mathcal{L}_{y\ s} >$ of Eq. 3.18).

constant which varies year-to-year relating the rate to the luminosity per nucleon, A is the number of nucleons per nucleus, $\tau_{\text{DAQ-up-\%}}$ is the fractional live-time of the DAQ, and t_{burst} is the length of the burst.

3.5 Polarimetry

Beam and target polarization values are another essential burst-level-measured ingedient of this analysis. While we take the beam polarization burst-by-burst from the `rPolFit` record of the `g1Beam` table of the μDST files, a single target polarization value for each year is provided to us by the HERMES target group. The yearly average polarization of beam and target are given in Table 3.10.

The actual polarization-related quantity required in the analysis will be $\mathcal{L}_s \times < P_s >$, the luminosity weighted polarization for each spin state s. This is computed:

$$\mathcal{L}_s < P_s >= \sum_{\text{y:\{years\}}} < P^{\text{targ}}_{y\ s} >< \mathcal{L} P^{\text{beam}}_{y\ s} > \tag{3.17}$$

where

$$< \mathcal{L} P^{\text{beam}}_{y\ s} >= \sum_{b:\{\text{bursts}_{ys}\}} \mathcal{L}_b\ P^{\text{beam}}_b. \tag{3.18}$$

Chapter 4

Asymmetries

The asymmetry is the core component of this analysis as well as many others at HERMES. Two important things are accomplished by taking the ratio of the difference of two quantities to the sum rather than looking at a difference alone. First, most systematic uncertainties, particularly those unrelated to the property being compared in the asymmetry, will cancel out in the ratio. Second, the denominator, which serves as a normalizing factor for the difference, can often be equated to the results of other experiments which are specifically designed to measure precise cross sections. This alleviates the need to measure the luminosity precisely at HERMES, allowing physical quantities to be extracted by making a precise, but purely relative measurement.

This chapter will describe the process by which several different sets of asymmetries are computed. The first of these is the longitudinal double-spin asymmetries $A_1(x)$ (inclusive) and $A_1^h(x)$ (semi-inclusive) from which $\Delta q(x)$ will be extracted. The second is the hadron charge-difference asymmetries. These quantities can be shown under certain fragmentation symmetry assumptions to equal the ratio of the sum of the valence helicity densities to the sum of the unpolarized valence PDFs. While interesting alone, they also provides a useful comparison to the same quantity produced via the purity extraction. This comparison will help to reveal the impact of various fragmentation model assumptions made in these two methods. The third will be the largely unexplored $A_1(p_{h\perp})$. This interesting result provides a glimpse into sources of transverse momentum inside the nucleon and in the fragmentation process. Finally, we will describe the method by which asymmetries binned in three dimensions x, z, $p_{h\perp}$, which are included in the appendices, are produced.

As a final note, while we will spend the following two chapters deriving further quantities and, albeit with strong support, assuming various models through which we interpret these data, it seems worthwhile to remind ourselves that the asymmetries represent *the measurement*. Whether or not one believes the model-assumptions we will make later, the asymmetries presented in this

chapter are, barring (ever possible) experimental errors, indisputable empirical results.

4.1 The Longitudinal Double-Spin Asymmetry

The longitudinal double-spin asymmetry:

$$A_1(x) \equiv \frac{\sigma_{1/2} - \sigma_{3/2}}{\sigma_{1/2} + \sigma_{3/2}} = \frac{g_1}{F_1} \stackrel{\text{LO}}{=} \frac{\sum_q e_q^2 \Delta q(x)}{\sum_q e_{q'}^2 q'(x)}, \tag{4.1}$$

and its siblings, the semi-inclusive double-spin asymmetries,

$$A_1^h(x) \equiv \frac{\sigma_{1/2}^h - \sigma_{3/2}^h}{\sigma_{1/2}^h + \sigma_{3/2}^h} \stackrel{\text{LO}}{=} \frac{\sum_q e_q^2 D_q^h(x, z, p_{h_\perp}) \Delta q(x)}{\sum_{q'} e_{q'}^2 D_{q'}^h(x, z, p_{h_\perp}) q'(x)}, \tag{4.2}$$

where the superscript h denotes the hadron species observed in the final state, will ultimately grant access to the individual quark flavor contributions to the nucleon spin, $\Delta q(x)$, by way of parameterized spin-independent structure functions, $q(x)$ and modeled fragmentation functions, $D_q^h(x, z, p_{h_\perp})$. The qualified equality, $\stackrel{\text{LO}}{=}$, reminds us that this particular factorization of PDF and fragmentation function is true in leading-order QCD. $\sigma_{1/2}$ and $\sigma_{3/2}$ are the photoabsorption cross sections with the photon and nucleon polarizations antiparallel ($J_z = 1/2$) and parallel ($J_z = 3/2$) respectively.

4.1.1 Experimental Asymmetries

The first step is to relate the experimental yields to the definition of $A_1(x)$ provided above. There are two main issues that must be addressed to accomplish this. The first will be to relate the yields produced with a particular experimental configuration of beam and target to yields of a particular lepton and nucleon polarization. The second will be to relate the lepton-nucleon (or experimental) asymmetry, $A_{||}$, to the photoabsorption asymmetry A_1 defined above.

Because an imperfect polarization of beam and target means that some fraction of the beam is unpolarized (i.e. evenly composed of both states) we must interpret each experimental spin configuration as a combination of *both* physical spin states.

Let $+$ denote the condition when the spins of the beam electron and target nucleon are antiparallel, and let $-$ denote the parallel state. (The symbols represent the product of the beam and target helicities in the center of mass frame.) In contrast, we will use the symbols $\uparrow\downarrow$ ($\uparrow\uparrow$) and $\uparrow\uparrow$ ($\uparrow\downarrow$) to denote the relative orientation of the *polarizations* of beam and target (which is all that one can control experimentally). If we let σ^e denote the spin-independent *lepton-nucleon* cross section ($(\sigma_+^e + \sigma_-^e)/2$) and $\Delta\sigma^e$ denote the spin-dependent lepton-nucleon cross section ($(\sigma_+^e - \sigma_-^e)/2$), the yield for a particular *experimental* configuration can be written:

$$
\begin{aligned}
N_{\uparrow\downarrow(\uparrow\uparrow)} &= L_{\uparrow\downarrow(\uparrow\uparrow)}\left(\sigma^e + P_{\uparrow\downarrow(\uparrow\uparrow)}\Delta\sigma^e\right) \\
&= L_{\uparrow\downarrow(\uparrow\uparrow)}\left(\sigma^e_{+(-)}\frac{1+P_{\uparrow\downarrow(\uparrow\uparrow)}}{2} + \sigma^e_{-(+)}\frac{1-P_{\uparrow\downarrow(\uparrow\uparrow)}}{2}\right).
\end{aligned} \tag{4.3}
$$

Here L is the luminosity and P is the average polarization of a particular experimental spin state ($-1 < P < 1$). Note that in the limit of perfect beam and target polarization and identically balanced luminosities of the two spin states, these two sets of notation would be redundant as the experimental configuration $\uparrow\downarrow$ ($\uparrow\uparrow$) would *always* correspond to lepton-nucleon configuration $+(-)$. One can then use yields of both spin states to arrive at the following expression for the (semi-)inclusive experimental asymmetry, $A_{||}^{(h)}$,

$$
A_{||}^{(h)}(x) \equiv \frac{\sigma_+^{e(h)} - \sigma_-^{e(h)}}{\sigma_+^{e(h)} + \sigma_-^{e(h)}} = \frac{L_{\uparrow\uparrow}N_{\uparrow\downarrow}^{(h)} - L_{\uparrow\downarrow}N_{\uparrow\uparrow}^{(h)}}{L_{\uparrow\uparrow}P_{\uparrow\uparrow}N_{\uparrow\downarrow}^{(h)} + L_{\uparrow\downarrow}P_{\uparrow\downarrow}N_{\uparrow\uparrow}^{(h)}}. \tag{4.4}
$$

The next step is then to relate the experimental lepton-nucleon asymmetry, $A_{||}(x)$, to the photoabsorption asymmetry $A_1(x)$ in which we are interested. The primary difference is the "depolarization" that occurs at the lepton-photon vertex: the imperfect transfer of polarization from the lepton beam to the virtual photon. This kinematic-dependent depolarization is well understood and allows one to write $A_1(x)$ as a function of the measured yields:

$$
A_1(x) = C_{\phi_h}\frac{1}{f_D}\frac{1}{D(1+\eta\gamma)}A_{||}^B(x) \tag{4.5}
$$

where,

$$
D = \frac{1-(1-y)\epsilon}{1+\epsilon R}, \tag{4.6}
$$

$$
\epsilon = \left[1 + \frac{2\vec{q}^2}{Q^2}\tan^2\frac{\theta}{2}\right]^{-1} = \frac{1-y-\frac{1}{4}\gamma^2y^2}{1-y+\frac{1}{4}y^2(\gamma^2+2)}, \quad \text{and} \tag{4.7}
$$

$$
\eta = \frac{\epsilon\gamma y}{1-(1-y)\epsilon}. \tag{4.8}
$$

ϵ is the ratio of longitudinal to transverse photon flux, γ is a kinematic factor characterizing the virtual photon which is computed $\sqrt{Q^2/\nu^2}$, and R, finally, is the ratio σ_L/σ_T of the photoabsorption cross sections for longitudinally and transversely polarized virtual photons. The R1999 parameterization is used [19] for R. While a purely inclusive parameterization, it represents our best knowledge to date of σ_L/σ_T. Any dependence of this ratio on produced hadron type – i.e. the semi-inclusive version of this ratio – is unknown. One could argue that if kinematics provide a reasonable factorization of the PDFs and fragmentation functions, that any dependence on produced hadron type must be small. In this analysis, R1999 is applied to both inclusive and

semi-inclusive asymmetries. f_D is a target polarizability (dilution) factor that will be described in Section 4.2.

In section 4.3 will see in detail how the experimental Born-level asymmetry, $A_{||}^B(x)$, is produced from the measured asymmetry $A_{||}$ of Equation 4.4 through an unfolding procedure that corrects for radiative and detector smearing. Finally, we have assumed up to this this point that our spectrometer provides us with a perfectly uniform acceptance. As we will see in Section 4.4, this is not entirely the case. An additional azimuthal correction factor C_{ϕ_h} is included for the semi-inclusive asymmetries. It corrects for the product of the spectrometer's non-uniform azimuthal acceptance (with respect to the scattered lepton) with the non-zero azimuthal modulation of hadron production which becomes entangled when integrating over ϕ_h.

4.1.2 Choosing the Inclusive W^2 Cut

As discussed in Section 3.2.1, it is *a priori* unclear where exactly to cut on W^2 for inclusive events. The standard $W^2 > 4$ GeV^2 cut, which operationally defines the deep-inelastic scattering region, serves to exclude the coherent excitation of nucleon resonances in the target. For semi-inclusive analyses at HERMES, however, a more stringent cut of $W^2 > 10$ GeV^2 is imposed. The reasons are twofold. First, the HERMES detector acceptance for SIDIS hadrons falls off rapidly below this W^2 limit, and second, larger W^2 provides a greater kinematic separation between the current and target fragmentation regions. Selecting the current fragmentation region is important for SIDIS, where one hopes to describe the hadronic final state with a simple quark-fragmentation picture, but for the inclusive yields, it would be reasonable to include the additional range $4 - 10$ GeV^2 to increase statistics. The decision was made strictly on the statistical impact on the asymmetries of including this extra data. The comparison of the effect of these two cuts on the inclusive asymmetries can be seen in Figure 4.1.

It was observed that although lowering the W^2 cut to 4 GeV^2 increases the statistical precision of the experimental asymmetry, $A_{||}(x)$, the additional events are plagued with a large depolarization factor (i.e. low polarization transfer between the lepton and virtual photon). By comparing the photon asymmetry $A_1(x)$ measured with these two minimum W^2 cuts, it is clear that any positive impact of the improvement in statistics from this relaxed cut is lost in the increased average depolarization of the sample. This causes the precision of A_1 to be equivalent or even worse in some bins than it was with the more selective $W^2 > 10$ GeV^2 cut.

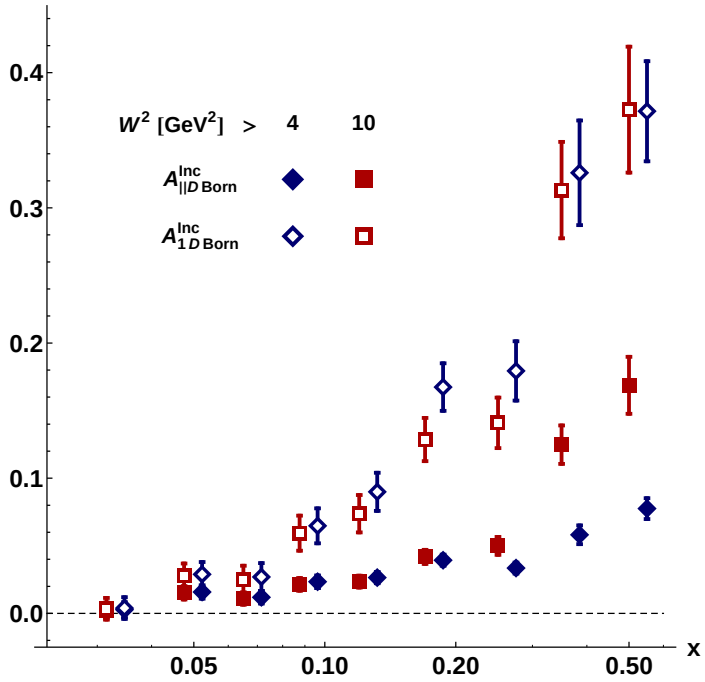

Figure 4.1: Inclusive asymmetries $A_{||}(x)$ and $A_1(x)$ from the deuteron target with two different minimum W^2 cuts. While one might try to improve statistical precision by including inclusive events from lower W^2 (compare the precision of the $A_{||}(x)$ points), the depolarization of the additional events is significantly higher providing practically no additional precision (loss in some bins!) to the physics asymmetry (compare $A_1(x)$ points).

4.2 Nucleon Polarizability

The quantity f_D represents the polarizability of the nucleons in the target.[1] For hydrogen with its single nucleon, $f_D = 1$. Because deuterium ($J^P = 1^+$) has two nucleons, it is somewhat more complicated (all angular momenta are given in units of $\hbar$). The parity quantum number of the deuteron (+) requires the spins of the nucleons to be aligned, so total spin $S \neq 1$ is forbidden. While the deuteron spends the majority of its time in an S-state ($L = 0$, $S = 1$), it can reside in the D-state ($L = 2$, $S = 1$) at times. If we require $M = 1$ (the projection of the total angular momentum, J, to be polarized), one can write down an angular momentum wave function describing the total spin projection m_S and orbital angular momentum projection m_L composition of the deuteron using the appropriate $L + S = 2 \otimes 1$ Clebsch-Gordan coefficients:

$$|\psi\rangle = \sqrt{\frac{3}{5}}\,|m_L = 2, m_S = -1\rangle - \sqrt{\frac{3}{10}}\,|m_L = 1, m_S = 0\rangle + \sqrt{\frac{1}{10}}\,|m_L = 0, m_S = 1\rangle\,. \tag{4.9}$$

From this, one can see that the nucleon spins are antiparallel to M 50% of the time ($\frac{3}{5} - \frac{1}{10}$). This means that in the D-state, the nucleons have a 50% polarization opposite to the deuteron polarization. The final polarizability of the nucleons can then be found by dividing the number of nucleons with spins parallel to the angular momentum of the nucleus by the total number of nucleons:

$$\begin{aligned} f_D &= \frac{1}{N}\left(N_S - \frac{1}{2}N_D\right) \\ &= \frac{1}{N}\left(N - \frac{3}{2}N_D\right) \\ &= 1 - \frac{3}{2}P_D. \end{aligned} \tag{4.10}$$

N_S and N_D are the numbers of nucleons in the S and D states respectively. P_D is the probability of finding the nucleus in the D-state, which has been estimated from a number of different models to be 0.0490 ± 1.04, giving us a final value for $f_D = 0.926 \pm 0.016$[20].

4.3 Unfolding and the Born Asymmetry

Recall the definition of the leading-order DIS process which was introduced in Chapter 1. The physical asymmetry of interest is the *Born* asymmetry, A_1^B, which is produced by the lowest order QED diagram. Experimentally, DIS events are produced from both Born events and other, often indistinguishable, events of higher orders. These events, most notably the emission of initial state or final state QED radiation, tend to distort the true kinematics of the Born event. Furthermore,

[1] The use of the term "polarizability" to describe the maximum nucleon polarization within the target is not to be confused with the (perhaps more common) use of the word to describe an induced dipole moment.

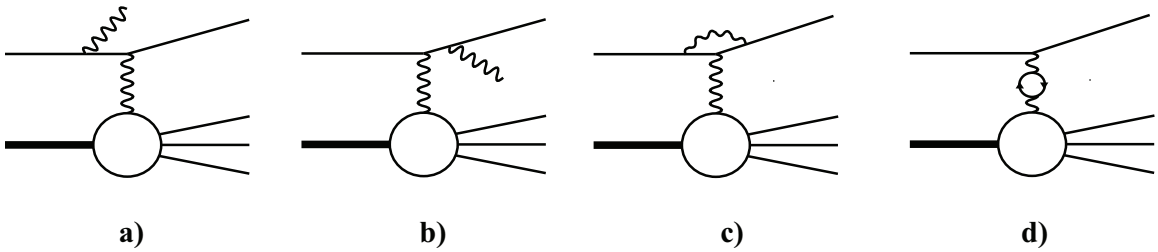

Figure 4.2: Higher order QED Feynman diagrams contributing to the DIS cross section. These contributions are not taken into account in the Born approximation.

instrumental effects tend to further distort true event kinematics. A single unfolding correction will remove the kinematic smearing produced by these two effects.

4.3.1 Radiative Effects

Of the higher order diagrams shown in Figure 4.2, a) initial state Bremsstrahlung and b) final state Bremsstrahlung present the most significant challenge. Because a radiated real photon is rarely observed, a) and b) can cause significant miscalculation of the correct *Born level* event kinematics. In particular, non-DIS events, which would typically be rejected on measured kinematic criteria, can be mistakenly accepted due this shift in kinematics. Many of these events are elastic (the lepton beam scatters off the nucleus as a whole, leaving it intact) or quasi-elastic (elastic scattering from a single nucleon within a nucleus). Clearly quasi-elastic scattering is only a possibility for the deuteron target.

These radiative events always cause an overestimate in ν, the energy transferred to the virtual photon, as the unobserved radiated photon carries energy away from the event. Because of this, radiative events are concentrated at large values of observed $y = \nu/E_{\text{beam}}$ as we saw in Figure 3.4. Another consequence is that radiative corrections always move events from large to small $x = Q^2/2M\nu$.

Radiative smearing is greatly reduced for the semi-inclusive yields: as elastic or quasi-elastic scattering cannot produce an additional final state hadron, elastic and quasi-elastic radiative tails are absent from the SIDIS samples. This can be seen clearly by comparing the Monte Carlo event migration plots on the left and right of Figure 4.3.

4.3.2 Detector Smearing

Additional kinematic smearing is produced by instrumental effects. Multiple scattering of particles as they pass through the detector materials can cause small errors in track angles. This can lead to discrepancies between front and back tracks which distort the true track momenta. Smearing can also be caused by small miscalibrations in instruments. In general, detector smearing, unlike

radiative smearing, can cause tracks to migrate to nearby kinematic bins in any direction.

4.3.3 The Unfolding Correction

In order to correct for these two smearing effects, a single kinematic unfolding procedure is applied. The central idea of this correction method is that by using a Monte Carlo model, which includes both radiative and detector effects, one can build a migration matrix that contains the correlations between Born and final observed kinematic bins. This matrix can be inverted and applied to the observed yields. Simulated events are produced using a Monte Carlo generator, gmc_disNG, which contains the PEPSI4 event generator and RADGEN [21] which produces radiative processes. While the CTEQ6 PDF parameterization is consulted to select the struck quark flavor in each event, it is not used to produce event kinematics as it doesn't reproduce the cross section at HERMES kinematics well. Because of this, the unpolarized inclusive cross section is provided by the ALLM97 [22] parameterization of the F_2 structure function which is more successful at this task. RADGEN can produce any of the higher-order process depicted in Figure 4.2. Events are then propagated through a detailed GEANT3 detector model to generate a detector response which can be reconstructed using HRC, the standard HERMES event reconstruction software.

In most recent analyses at HERMES, the unfolding correction was formulated to be applied directly to raw experimental asymmetries. Though rather elegant, the generalization of that method to the hadron difference asymmetries – one of the goals of this work – was unclear. In order to address this, a more general unfolding algebra was necessary. The method presented here will allow us to unfold the experimental *yields* and then form asymmetries from them. This makes it obvious how to compute complex asymmetries requiring an arbitrary number of smearing matrices (rather than the single one afforded by the more traditional method).

The starting point for this unfolding calculation is the following relationship between the experimentally observed and Born yields,

$$N^X(i) = \sum_j \left[S(i,j)N^B(j)\right] + N_0(i). \tag{4.11}$$

N^X and N^B are experimental and Born yields respectively. N_0 is the vector of events smeared into acceptance (both geometric and kinematic) which should otherwise be cut. The *smearing matrix*, $S(i,j) \equiv M(i,j)/N^B(j)$, where $M(i,j)$ is a migration matrix – a two-dimensional histogram correlating each event's observed (i) and Born (j) kinematic bins. It follows from Equation 4.11 that,

$$N^B(j) = \sum_i S^{-1}(i,j)\left[N^X(i) - N_0(i)\right]. \tag{4.12}$$

In order to carry out this calculation, we begin by applying the preceding formula to the observed

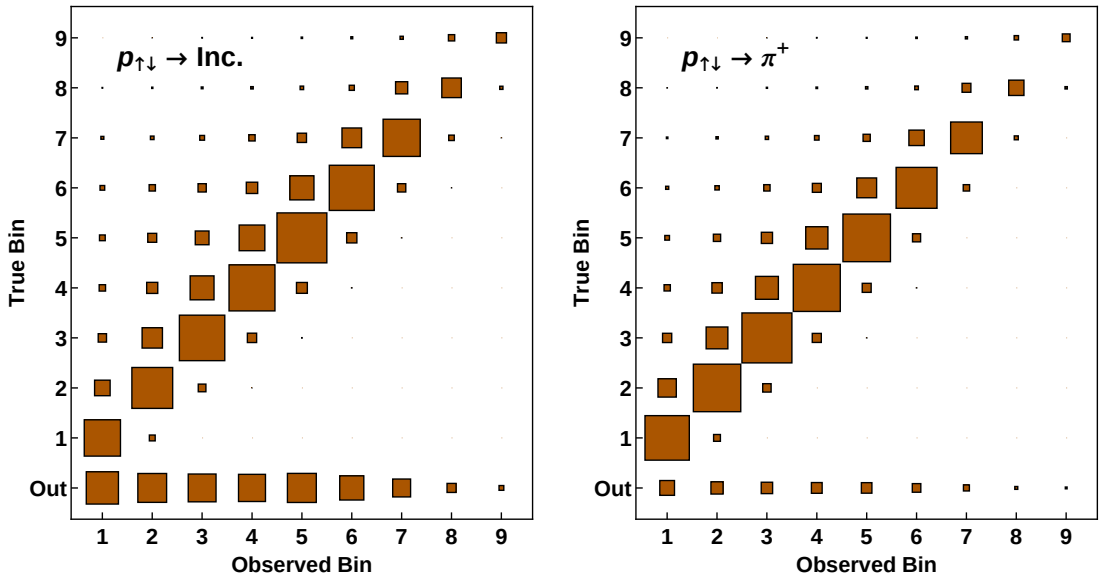

Figure 4.3: Monte Carlo migration matrices for inclusive events (left) and semi-inclusive π^+ production (right) binned in the "traditional" 9 x-bins. The "True"-"Out" bin represents events smeared into experimental acceptance by QED radiation and detector effects.

spin-dependent lepton-nucleon yields of section 4.1.1. Equation 4.3 can be solved (using: $N^X_{-(+)} = L_{-(+)}\sigma^e_{-(+)}$) to give:

$$N^X_{-(+)} = N^X_{\uparrow\uparrow(\uparrow\downarrow)} L_{\uparrow\downarrow(\uparrow\uparrow)}(1 + P_{\uparrow\downarrow(\uparrow\uparrow)}) - N^X_{\uparrow\downarrow(\uparrow\uparrow)} L_{\uparrow\uparrow(\uparrow\downarrow)}(1 - P_{\uparrow\uparrow(\uparrow\downarrow)}), \tag{4.13}$$

which results in the following formula for the unfolded Born yields:

$$N^B_{-(+)}(j) = \sum_i \mathcal{S}^{-1}_{-(+)}(i,j) \left[N^X_{-(+)}(i) \frac{\mathcal{N}^X_u}{N^X_u}(i) - \mathcal{N}_0(i) \right]. \tag{4.14}$$

The quantities $\mathcal{S}$, $\mathcal{N}^x_u$, and $\mathcal{N}_0$ will come from Monte Carlo simulation and have been denoted with calligraphic symbols which will be used for all Monte Carlo quantities. Two Monte Carlo sets will be used here – one including RADGEN, used to produce the migration matrices, and a Born Monte Carlo to produce Born yield vectors. Both samples are produced with 100% polarization. The subscript u represents unpolarized variables– i.e. the sum of the quantity from each spin state. The fraction $\frac{\mathcal{N}^X_u}{N_u}(i)$ serves as a normalization factor, scaling the experimental luminosity to that of the Monte Carlo sample. One side effect of this normalization is that the yields themselves can no longer be interpreted as simple counts. This arbitrary normalization, however, cancels in asymmetries.

Finally then, using this result and Equation 4.4, one can write down the expression for the

experimental Born asymmetry:

$$A_{||}^{B}(x) = \frac{N_{+}^{B} - N_{-}^{B}}{\mathcal{N}_{+}^{B} + \mathcal{N}_{-}^{B}}. \tag{4.15}$$

While it might appear at first glance that we've done something suspicious with the unpolarized experimental yield (and more specifically, its uncertainty) in the denominator by choosing the high-statistic Monte Carlo values, rest assured that the unpolarized data denominator resides safely in our expression for $N^B-(+)$ (i.e. N_u^X in 4.14). Its contribution to the uncertainty of the Born yield and asymmetry will be included in the next section. That being said, A_1^B can then be computed using the same depolarization and kinematic factors applied in Equation 4.5.

In order to address a common source of confusion, it seems important to point out that we are not making an *acceptance correction*, that is, we are not attempting to take a result in detector acceptance and unfold it to 4π, as we require both Monte Carlo samples used to be in acceptance. The resulting experimental Born asymmetries, $A_{||}^B$, are in acceptance– which means *only* that they are provided at the measured (and quoted) x and Q^2. In fact, attempting to unfold to 4π is both unnecessary, as the asymmetries are meaningful functions of any choice of kinematics, and problematic, as the shift in average kinematics variables from acceptance to 4π is difficult to propagate through the unfolding procedure. This would make the calculation of the depolarization factor practically impossible.

It is true, however, that the procedure of placing cuts on the true geometric track variables, which constrains the data sample to a region free of detector obstructions and away from edges, means that this is a correction "box acceptance" – a well defined, experimentally clean, geometric volume defined by the cuts of Table 3.3 and which closely resembles the acceptance of the HERMES spectrometer. Furthermore, since the unfolding correction maps observed aggregate yields back to their Born level origin, this procedure (in principle) corrects the data sample to a uniform 100% detector efficiency. Unlike a 4π-acceptance correction, the difference in bin-averaged kinematics between box and detector acceptance is negligible.

As can be seen in Figure 4.4, there are significant differences between asymmetries in acceptance and 4π. However, there are also significant differences in average x and Q^2 of the bins. For the inclusive case, which can *only* depend on two variables, this kinematic difference is the only possible source of the discrepancy. As we provide data points with bin-averaged kinematics, this causes no confusion. While the semi-inclusive asymmetries could potentially depend on z and $p_{h\perp}$ as well, 1) they show discrepancies of similar scale and kinematic behavior to the inclusive asymmetries and 2) the final asymmetries (Figure 4.18, for example) show very little dependence on these semi-inclusive variables. These reasons suggest that we can safely provide semi-inclusive asymmetries (and further derivative results) in box acceptance as long as average x and Q^2 are provided.

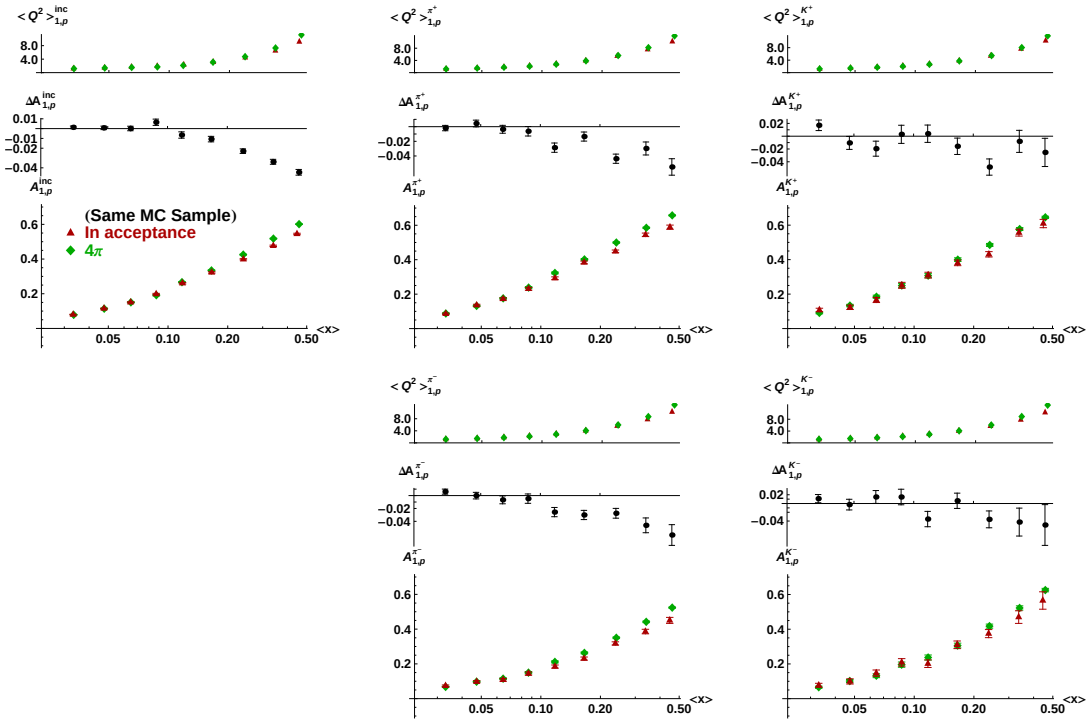

Figure 4.4: Monte Carlo asymmetries for the proton in HERMES acceptance and in 4π. The differences in the asymmetries can be attributed to entirely to the difference in average kinematics.

4.3.4 Statistical Uncertainties of the Born Asymmetries

The calculation of the statistical uncertainties follows from the standard error propagation formula (which can be found among other places in the Particle Data Book [5]). The notation $\sigma(A, B)$ will be used to denote the statistical covariance of A and B. The variance of A, $\sigma^2(A) \equiv \sigma(A, A)$, is equivalent to $(\delta A)^2$, or the square of the statistical uncertainty of A.

We will begin by computing the (co)variance of the Born yield. Hadron indices have been omitted, but can be applied trivially to all symbols.

$$\sigma\left(N^B_{s_1}(i), N^B_{s_2}(j)\right) = \sum_k \sum_l \frac{\partial N^B_{s_1}(i)}{\partial N_k} \frac{\partial N^B_{s_2}(j)}{\partial N_l} \, \sigma\big(N_k, N_l\big). \tag{4.16}$$

s_1 and s_2 can each take either value of the physics spin state, $+$ or $-$. The summation variables k and l index all possible configurations of spin-state and kinematic bin (i.e., N_k is shorthand for $N_{k_{\text{spin}}}(k_{\text{kin}})$). By choosing to express N^B in terms of the experimental spin states $\uparrow\uparrow$ and $\uparrow\downarrow$ (i.e. by substituting 4.13 into 4.14), k and l run over only the experimental, *statistically uncorrelated*, states. A result of this choice is that $\sigma\big(N_k, N_l\big)$ becomes $\sigma^2(N_k)\ \delta_{k,l}$. The preceding formula can be simplified:

$$\sigma\left(N^B_{s_1}(i), N^B_{s_2}(j)\right) = \sum_k \frac{\partial N^B_{s_1}(i)}{\partial N_k} \frac{\partial N^B_{s_2}(j)}{\partial N_k} \, \sigma^2(N_k). \tag{4.17}$$

We now take the derivative of the Born yield element, $N_s^B(j)$. Since the k index represents both a spin configuration and kinematic bin, k_{spin} and k_{kin} will be used to denote the spin and bin respectively. Notice that the derivative with respect to N_k picks out the k^{th} element of the sum in 4.14.

$$\frac{\partial N_{s_1}^B(j)}{\partial N_k}\sqrt{\sigma^2(N_k)} = \left\{ \begin{array}{rcrr} k_{\text{spin}} & = & \uparrow\downarrow: & 1 \\ k_{\text{spin}} & = & \uparrow\uparrow: & -1 \end{array} \right\} \times \frac{1}{2}\, \mathcal{S}^{-1}(k_{\text{kin}}, j)\, \mathcal{N}_u^X(k_{\text{kin}})\, F(k_{\text{kin}}), \tag{4.18}$$

where,

$$F(k) \;=\; (L_{\uparrow\downarrow}LP_{\uparrow\uparrow} + L_{\uparrow\uparrow}LP_{\uparrow\downarrow})\, \frac{\sqrt{N_{\uparrow\uparrow}(k)^2\; \sigma^2\left(N_{\uparrow\downarrow}(k)\right) +\; N_{\uparrow\downarrow}(k)^2\; \sigma^2\left(N_{\uparrow\uparrow}(k)\right)}}{\left(LP_{\uparrow\downarrow}N_{\uparrow\uparrow}(k) + LP_{\uparrow\uparrow}N_{\uparrow\downarrow}(k)\right)^2}, \tag{4.19}$$

which contains only the experimentally determined quantities.

Finally, tidying up, we rewrite 4.17,

$$\sigma\left(N_{s_1}^B(i), N_{s_2}^B(j)\right) = \left\{ \begin{array}{rr} s_1 = s_2: & 1 \\ s_1 \neq s_2: & -1 \end{array} \right\} \times\; \frac{1}{4} \sum_l\; \mathcal{S}_{s_1}^{-1}(l,i)\; \mathcal{S}_{s_2}^{-1}(l,j)\; \mathcal{N}_u^X(l)^2\; F(l)^2, \tag{4.20}$$

where the index, l, runs over kinematic bins.

Uncertainty of the Longitudinal Double-Spin Asymmetry

Using 4.20, computing the covariances of the asymmetries themselves becomes relatively straightforward. For the longitudinal double-spin asymmetry:

$$\begin{aligned} \sigma(A_{||}^B(i), A_{||}^B(j)) \;&=\; \sum_k \sum_l \frac{\partial A_{||}^B(i)}{\partial N_k^B} \frac{\partial A_{||}^B(j)}{\partial N_l^B}\; \sigma\left(N_k^B, N_l^B\right) \\ &=\; \left(\frac{1}{\mathcal{N}_u^B(i)\; \mathcal{N}_u^B(j)}\right) \left[\sigma\left(N_+^B(i), N_+^B(j)\right) + \sigma\left(N_-^B(i), N_-^B(j)\right)\right. \\ &\qquad \left. -\; 2\; \sigma\left(N_+^B(i), N_-^B(j)\right)\right] \end{aligned} \tag{4.21}$$

Once again, k and l range over all spin-state–kinematic-bin combinations. Because $A_{||}^B(i)$ depends *only* on the i^{th} bins of N_+^B and N_-^B, the i and j kinematic bins are picked out in the derivative. The result is that the summation (and covariances of the N^B) only depends then on the two spin states of the kinematic bins i and j.

The statistical uncertainty on a single bin of the Born asymmetries is the square-root of the

variance.

$$\begin{aligned}\sigma^2(A_{||}^B(i)) &\equiv \sigma(A_{||}^B(i), A_{||}^B(i)) \\ &= \left(\frac{1}{\mathcal{N}_u^B(i)}\right)^2 \left[\sigma^2\left(N_+^B(i)\right) + \sigma^2\left(N_-^B(i)\right) - 2\sigma\left(N_+^B(i), N_-^B(i)\right)\right]. \end{aligned} \tag{4.22}$$

While we've assumed that the size of the Monte Carlo sample is significantly larger than that of the data, which allows us to omit statistical uncertainties on the Monte Carlo yields, the uncertainty on the unfolded asymmetry *should not* and *does not* depend on the size of the Monte Carlo sample. This can be seen easily as both linearly dependant references to the size of the Monte Carlo sample, $\mathcal{N}_u^B$ in the denominator of Equation 4.22 and $\mathcal{N}_u^X$ of Equation 4.20, appear in canceling positions in the final expression.

Uncertainty of the Hadron Charge Difference Asymmetry

Unfolding the hadron charge-difference asymmetries follows without further complication from what was developed above. The asymmetry is defined as follows:

$$A_{||}^{h^+-h^-}(x) = \frac{\left(\sigma_+^{h^+}(x) - \sigma_+^{B\ h^-}(x)\right) - \left(\sigma_-^{h^+}(x) - \sigma_-^{h^-}(x)\right)}{\left(\sigma_+^{h^+}(x) - \sigma_+^{h^-}(x)\right) + \left(\sigma_-^{h^+}(x) - \sigma_-^{h^-}(x)\right)}, \tag{4.23}$$

where σ is the cross section (and not the variance). Just as above, in order to obtain the Born charge difference asymmetry, we rewrite it in terms of Born yields and Monte Carlo quantities.

$$A_{||}^{B\ h^+-h^-}(x) = \frac{\left(N_+^{B\ h^+}(x) - N_+^{B\ h^-}(x)\right) - \left(N_{B\ -}^{h^+}(x) - N_{B\ -}^{B\ h^-}(x)\right)}{\mathcal{N}_u^{B\ h^+}(x) - \mathcal{N}_u^{B\ h^-}(x)}. \tag{4.24}$$

Finally, computing the covariance of the charge difference asymmetry is performed as in Eq. 4.21.

$$\begin{aligned}\sigma\left(A_{||}^{B\ h^+-h^-}(i), A_{||}^{B\ h^+-h^-}(j)\right) = &\left(\frac{1}{\mathcal{N}_u^{B\ h^+}(i) - \mathcal{N}_u^{B\ h^-}(i)}\right)\left(\frac{1}{\mathcal{N}_u^{B\ h^+}(j) - \mathcal{N}_u^{B\ h^-}(j)}\right) \\ &\times\Big[\ \sigma\left(N_+^{B\ h^+}(i), N_+^{B\ h^+}(j)\right) \ + \ \sigma\left(N_-^{B\ h^+}(i), N_-^{B\ h^+}(j)\right) \\ &+ \ \sigma\left(N_+^{B\ h^-}(i), N_+^{B\ h^-}(j)\right) \ + \ \sigma\left(N_-^{B\ h^-}(i), N_-^{B\ h^-}(j)\right) \\ &- 2\ \sigma\left(N_+^{B\ h^+}(i), N_-^{B\ h^+}(j)\right) \ - 2\ \sigma\left(N_+^{B\ h^-}(i), N_-^{B\ h^-}(j)\right)\Big]. \end{aligned} \tag{4.25}$$

In practice, only the variances of the difference asymmetry are used in this work (i.e. $i = j$). For the standard single-hadron double-spin asymmetries, however, their covariances will play an essential role in the extraction of the quark helicity densities.

4.3.5 Error Bar Inflation

Prior to the development of bin-to-bin unfolding, many analyses at HERMES [23, 24] depended on an iterative approach to correcting for unwanted QED radiation[25]. This correction was based upon modeled cross sections and was applied to each bin individually. The drawback of this technique was that there was an implicit assumption of smoothness being made when this correction was applied. In principle, then, while the size of the statistical uncertainties remained largely unchanged, a significantly correlated model-dependent systematic uncertainty was introduced.

Our more rigorous bin-to-bin unfolding technique was developed in order to provide a model-independent correction. A drawback, however, is that because no assumption of smoothness is made, the uncertainty on each individual error bar increases in size. We are, in effect, adding pieces of all the neighboring error bars together when applying this correction. Though the *mean* number of events to "unmigrate" from one bin to another is very accurately known from our simulated smearing matrix, the *actual* number to relocate is subject to Poisson statistics and its $\sqrt{N}$ uncertainty. The phrase *error bar inflation* describing this effect has become all too familiar in the HERMES collaboration's vocabulary. Nothing is lost, however: the inflation of the errors is accompanied by an increased correlation between them. This correlation occurs entirely in the *statistical* uncertainties, and can be propagated through further calculations and fits using well-understood, robust error propagation methods which recover the full statistical precision of the data.

The point that we (the HERMES collaboration) have attempted to emphasize in papers and conference presentations is that although uncertainties appear inflated in plots – where only the diagonal elements of the error matrix are depicted – they have become statistically correlated in the unfolding process. By properly computing quantities like quark polarizations and curve fits from the asymmetries (compare for example the error bars to the fit error bands in Figure 4.18), one recovers the true statistical power of the data. We continue to encourage the community – world data fitters in particular – to include the full covariance of these results in their calculations. A fit to the x-dependant asymmetries will be provided in Section 4.5.1. The full covariance matrix will be utilized and the impact of assuming a smooth functional form will be demonstrated.

4.3.6 Generalizing Unfolding to Multiple Kinematic Dimensions

While the unfolding procedure discussed so far has been described in terms of a single kinematic variable, it can be easily generalized to unfold asymmetries of higher dimensionality. In fact, the formulae reference only kinematic bins *in general* and the migration-matrix correlations between them.

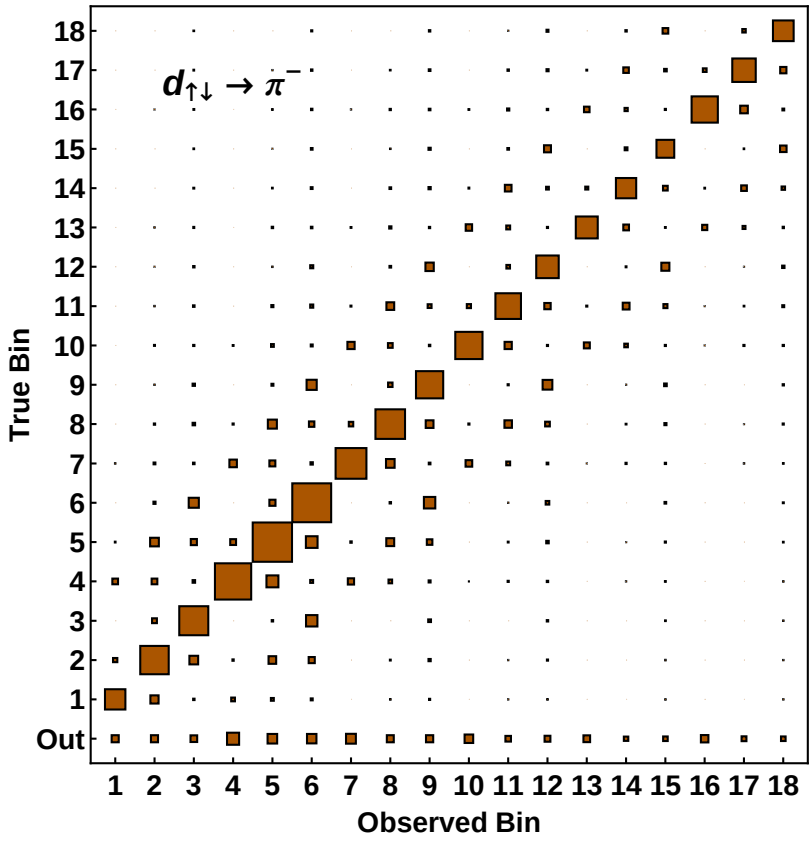

Figure 4.5: A Monte Carlo migration matrix for π^- from the deuteron target in x and p_T. The more complex migration structure visible is a result of the hybrid binning.

The natural extension of the migration matrix to higher dimensions is to create a *hybrid binning*. This means only that the bins of two or more kinematic variables are indexed by a single bin-index variable. For example, in the 2D case of x and $p_{h\perp}$, the index $i \equiv 6 \times (x_j - 1) + p_{h\perp\ k}$ supplies a variable that indexes the 18 combined $x_j - p_{h\perp}$ $k$bins ($3x \times 6p_{h\perp}$).This allows one to build a migration matrix which accounts for correlations of any two kinematic bins. An example of such a migration matrix is given in Figure 4.5 which depicts the event migration between hybrid x-$p_{h\perp}$ bins from the anti-parallel beam-target polarized deuteron. One can clearly see the more complicated migration structure which is created by the multidimensional binning.

4.4 Azimuthal Correction for Semi-Inclusive Asymmetries

At fixed beam energy, we've seen that inclusive scattering can ultimately be described by any two the of the numerous physically meaningful inclusive parameters (x, y, Q^2, W^2, ν, etc...). An equivalent and simple way to understand this is that there are two degrees of freedom in the final state. Since only the scattered lepton is being considered and the beam-target configuration has axial symmetry, the final-state lepton scattering distribution can be described by a polar angle and

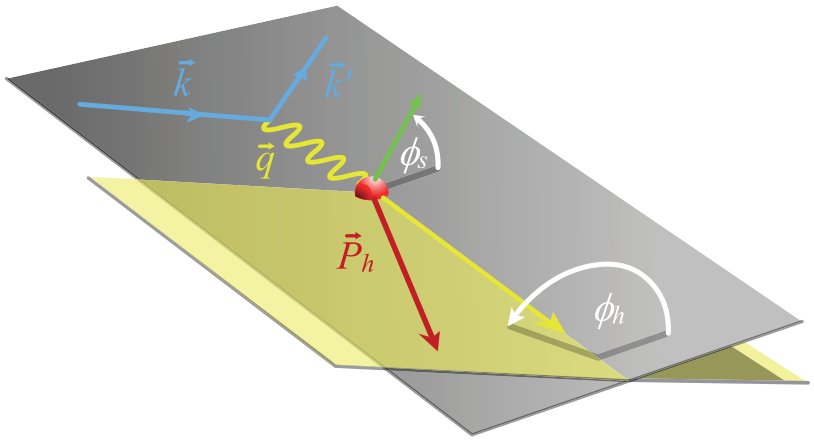

Figure 4.6: The azimuthal angle of the hadron, ϕ_h, is defined to be the angle between the hadron and lepton scattering planes.

a total momentum *or* any two momentum components, as the symmetry removes the need for one and the energy is constrained knowing the momentum and the lepton's fixed mass.

In semi-inclusive scattering, we have a second particle in the final state to consider. The azimuthal symmetry of the inclusive case is broken for the scattered hadron by the direction of the scattered lepton's momentum vector. Because of this, the hadron adds three more degrees of freedom to its distribution. Once again the hadron's energy (which would be a fourth degree of freedom!) is constrained since its identity is known and mass is fixed.

Strictly speaking, while an inclusive cross section can be written as a function of two variables, $\sigma(x, Q^2)$ for example, the semi-inclusive cross section must be written as a function of five: $\sigma^h(x, Q^2, z, p_{h\perp}, \phi_h)$. The azimuthal angle ϕ_h of the hadron relative to the lepton scattering plane is illustrated in Fig. 4.6.The Cahn Effect [26] is an example of a well known mechanism producing non-zero ϕ_h dependence of the unpolarized semi-inclusive cross section.

All of the results presented here will be integrated over a range of some, if not all of these semi-inclusive variables. While our result may contain theoretically reproducible kinematic constraints, it must not contain HERMES-specific acceptance features. As we quote the accepted ranges in all of these variables, or for ϕ_h integrate over all angles, this provides no additional difficulty *as long as* the spectrometer's acceptance is uniform in that variable. For z and $p_{h\perp}$, this is largely the case. For ϕ_h however, the spectrometer is known to have a non-uniform acceptance. Since the scattered lepton is required in an event (and is hence always in acceptance), one can imagine for example that for some values of ϕ_h, the hadron will have a greater likelihood of being lost down the beampipe.

We can write the semi-inclusive asymmetry explicitly including all these variables,

$$A_1^h = \frac{\int d\phi_h \ \Delta\sigma(x, Q^2, z, p_{h\perp}, \phi_h) \ \epsilon(\phi_h)}{\int d\phi_h \ \sigma(x, Q^2, z, p_{h\perp}, \phi_h) \ \epsilon(\phi_h)}, \tag{4.26}$$

where ϵ represents the spectrometer acceptance. This ϕ_h modulation can be decomposed completely [27] into $\cos(\phi)$ and $\cos(2\phi)$ moments as follows:

$$\begin{aligned}\frac{d\sigma}{dx\ dQ^2\ dz\ dp_{h\perp}\ d\phi_h} \propto \quad & \sigma_{UU}(x,Q^2,z,p_{h\perp}) \\ + \quad & \sigma_{UU}^{\cos(\phi)}(x,Q^2,z,p_{h\perp})\ \cos(\phi) \\ + \quad & \sigma_{UU}^{\cos(2\phi)}(x,Q^2,z,p_{h\perp})\ \cos(2\phi) \\ + \quad & P_b\ P_t\ \sigma_{LL}(x,Q^2,z,p_{h\perp})^2. \end{aligned} \tag{4.27}$$

The subscript UU of the first three coefficient functions denotes unpolarized beam and unpolarized target, while the subscript LL denotes longitudinally polarized beam and longitudinally polarized target. P_b and P_t represent the longitudinal polarizations of beam and target – which are zero in the unpolarized case.

In light of this expansion, if we rewrite 4.26, we can see that the unpolarized ϕ_h dependence of the numerator disappears since $\Delta\sigma = \sigma_{1/2} - \sigma_{3/2}$, leaving only the desired σ_{LL} term. What we measure can then be written as follows:

$$\tilde{A}_1^h = \frac{\Delta\sigma(x,Q^2,z,p_{h\perp})}{\int d\phi_h\ \sigma(x,Q^2,z,p_{h\perp},\phi_h)\ \epsilon(\phi_h)}, \tag{4.28}$$

where we seek,

$$A_1^h = \frac{\Delta\sigma(x,Q^2,z,p_{h\perp})}{\sigma(x,Q^2,z,p_{h\perp})}, \tag{4.29}$$

which is independent of the HERMES acceptance. To accomplish this, we make the following correction:

$$A_1^h = C_\phi^h \tilde{A}_1^h, \tag{4.30}$$

where,

$$C_\phi^h = \frac{\mathcal{A}_1^h}{\tilde{\mathcal{A}}_1^h}. \tag{4.31}$$

Once again calligraphic characters are used to denote quantities which we will estimate using Monte Carlo. We will take advantage of 1) the $\cos(\phi)$ dependence of the acceptance present in the Monte Carlo and 2) a parameterization of the unpolarized $\cos(\phi)$ moments which are otherwise missing from the Monte Carlo to achieve this. These $\cos(\phi)$ and $\cos(2\phi)$ moments have been extracted in another recent HERMES analysis. Using them we can construct this correction factor by producing asymmetries with and without $\cos(\phi)$ weighting.

[2]Strictly speaking, there are potentially $\sigma_{LL}^{\cos(\phi)}$ and $\sigma_{LL}^{\cos(2\phi)}$ terms in the polarized cross section as well. There are, however, no known or proposed mechanisms for producing such a spin-dependent ϕ_h modulation, and any ϕ_h dependence is as of yet completely unexplored.

4.4.1 ϕ_h Moments of the Unpolarized Cross Section

The parameterization of the cosine moments of the unpolarized cross section is a recent development at HERMES[28, 29]. While the preceding references describe a charge-separated parameterization for all hadrons, documentation of the (procedurally similar) fully hadron-separated sample used in this work are expected to follow shortly.

In order to create this parameterization, unpolarized semi-inclusive data were binned in five kinematic dimensions (x, y, z, $p_{h\perp}$, and ϕ_h) and unfolded (as in Section 4.3) in all of these dimensions simultaneously. The benefit of this technique is that, as none of the variables are integrated out, there is no convolution of the kinematic dependence with the acceptance of the spectrometer. The difficulty, however, is that in five dimensions – or 6000 kinematic bins (5-x $\times$ 4-y $\times$ 5-z $\times$ 5-$p_{h\perp}$ $\times$ 12-ϕ), even large Monte Carlo statistics yield migration matrices sparsely populated in its corners. Significant challenges relating to binning and matrix invertibility were at the forefront of the azimuthal analysis and the were the primary reason that we treat the azimuthal dependence as a correction and not part of our own unfolding.

The unfolded Born yields were fit with $\sigma_{UU}^{h\ \phi}\cos(\phi_h)$ and $\sigma_{UU}^{h\ 2\phi}\cos(2\phi_h)$ where,

$$\begin{aligned}
\sigma_{UU}^{h\ (2)\phi} \;=\; & A_1^{h\ (2)\phi} + A_2^{h\ (2)\phi}\, x + A_3^{h\ (2)\phi}\, y + A_4^{h\ (2)\phi}\, z + A_5^{h\ (2)\phi}\, p_{h\perp} \\
& + A_6^{h\ (2)\phi}\, x^2 + A_7^{h\ (2)\phi}\, z^2 + A_8^{h\ (2)\phi}\, p_{h\perp}^2 + A_9^{h\ (2)\phi}\, x\, z \\
& + A_{10}^{h\ (2)\phi}\, x\, p_{h\perp} + A_{11}^{h\ (2)\phi}\, z\, p_{h\perp} + A_{12}^{h\ (2)\phi}\, y\, p_{h\perp} \\
& + A_{13}^{h\ (2)\phi}\, x\, y + A_{14}^{h\ (2)\phi}\, y\, z + A_{15}^{h\ (2)\phi}\, y^2,
\end{aligned} \tag{4.32}$$

in order to extract coefficients parameterizing the ϕ moments for each hadron, h. Projections of resulting moments for combined hadrons of each charge can be seen in Figure 4.7. Plots for the separated hadrons samples used in this analysis are not available at this time, but preliminary results show that they are similar.

To compute the correction factor C_{ϕ_h} then, Monte Carlo yields in both spin states are produced with and without the track-by-track $\cos(\phi_h)$ weighting provided in the parameterization above. One can see in Figure 4.8, where the Monte Carlo was run in 4π, i.e. without imposing any geometric acceptance requirements, that the $\cos(\phi_h)$ modulation integrates out completely leaving only the unweighted result. In Figure 4.9, however, one can see that with the (ϕ dependent) acceptance imposed, the $\cos(\phi_h)$ weighting changes the integral of the $\cos(\phi)$ and thus the value of the asymmetry. As given in Eq. 4.31, the ratio of these two Monte Carlo asymmetries is the necessary acceptance correction, C_{ϕ_h}.

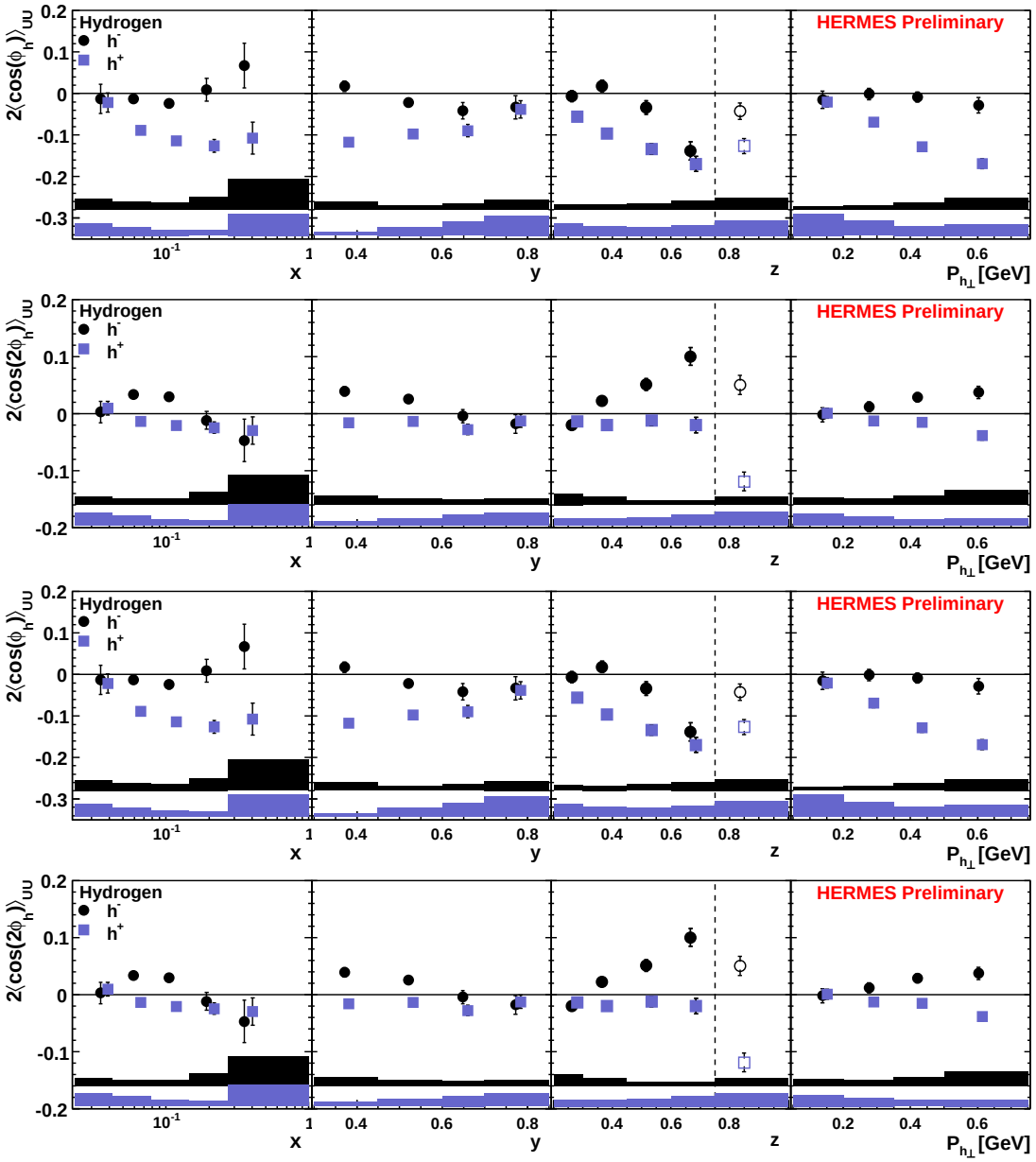

Figure 4.7: Projections of $\cos(\phi_h)$ and $\cos(2\phi_h)$ moments in each of the four other kinematic dimensions for the proton and deuteron targets and for positive and negative hadrons. (From [28])

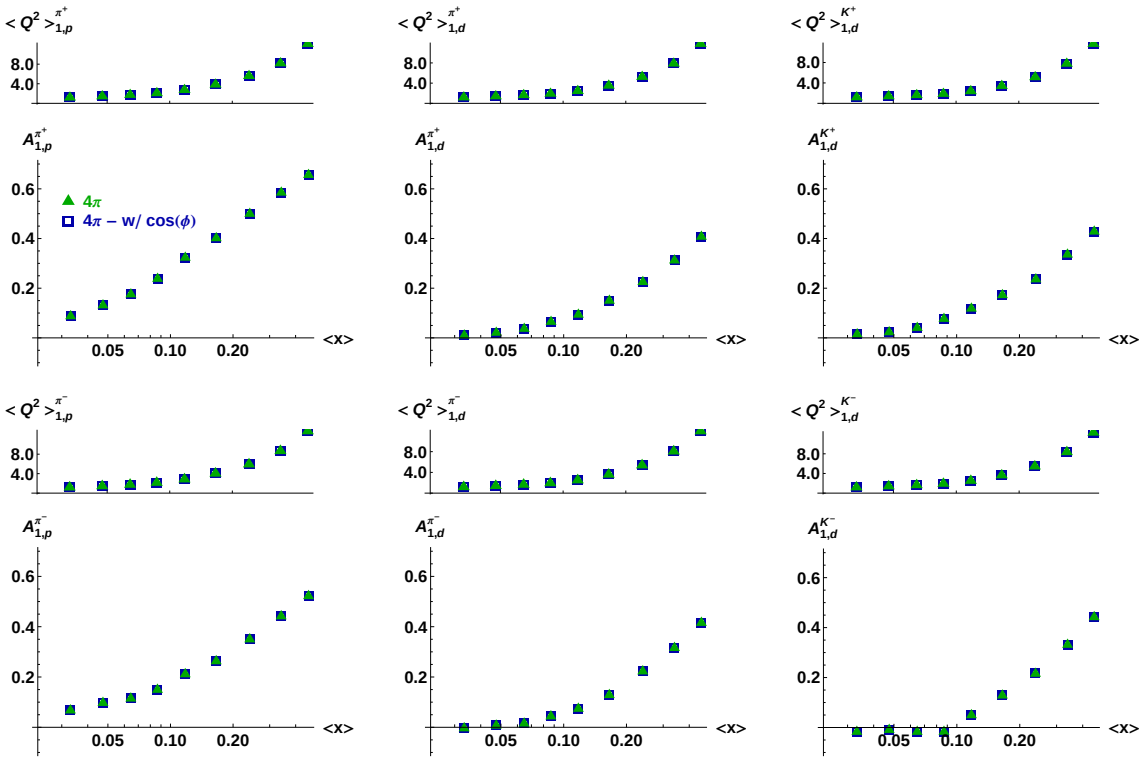

Figure 4.8: Comparison of 4π Born Monte Carlo samples with and without $\cos(\phi_h)$ weighting. Asymmetries for charged pions from the proton target and both pions and kaons from the deuteron target are shown. Since there is no ϕ_h-dependent acceptance included, the cosine moments of the unpolarized cross section integrate out over the full ϕ_h range.

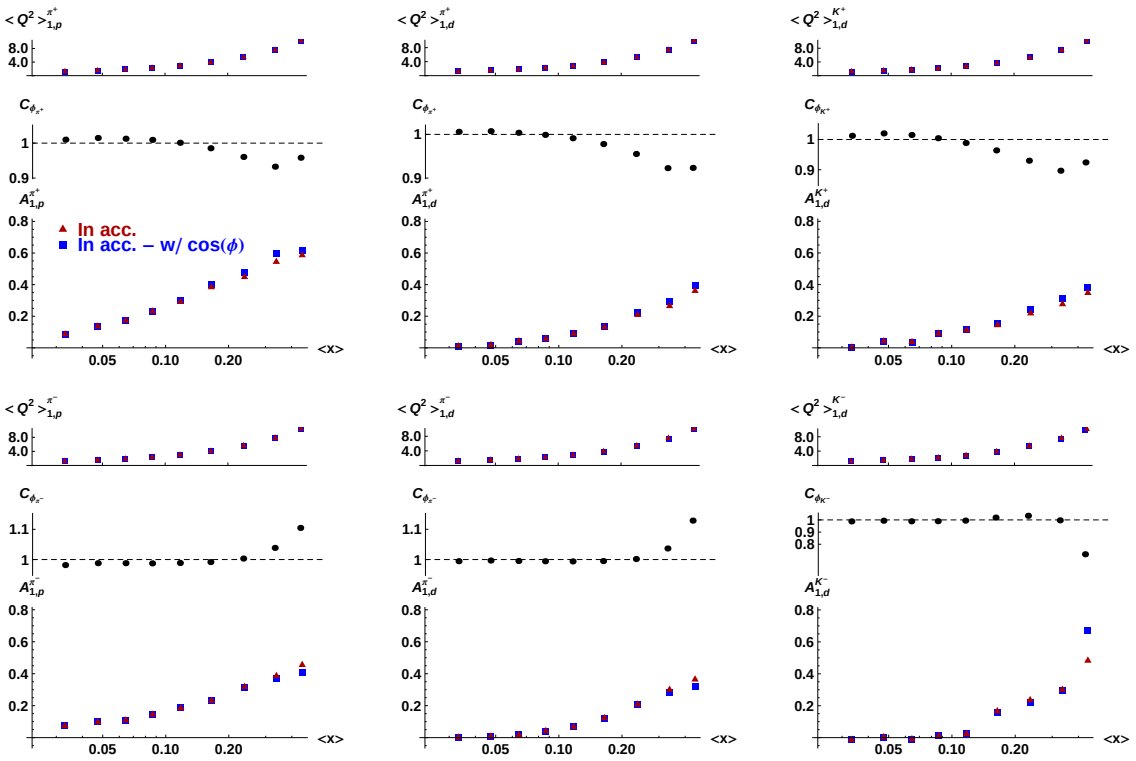

Figure 4.9: Comparison of Born Monte Carlo samples with and without $\cos(\phi_h)$ weighting in acceptance. Unlike the 4π comparison shown in Figure 4.8, the nonuniform acceptance of the spectrometer in ϕ_h creates significant differences between the weighted and unweighted asymmetries. The azimuthal correction factor C_{ϕ_h}, which is simply the ratio of the two asymmetries, is also shown.

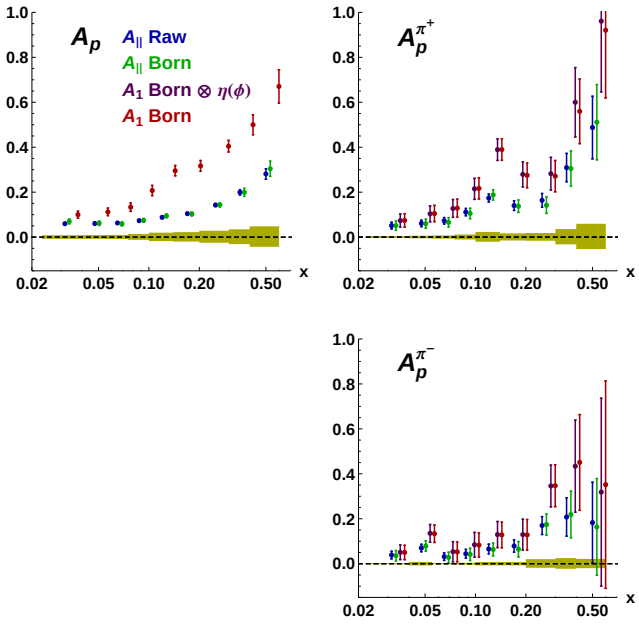

Figure 4.10: A_{1p} in stages. The four stages shown for each x-bin represent the inclusion of, 1) kinematic unfolding, 2) depolarization at the lepton–virtual-photon vertex, and 3) the azimuthal correction (which is only relevant for the semi-inclusive asymmetries). The yellow band represents the systematic uncertainty.

4.5 Final Born Asymmetries

We now have all of the ingredients required to take observed experimental yields, $N^h_{\uparrow\uparrow(\uparrow\downarrow)}$, and produce azimuthally corrected Born photon-nucleon asymmetries, A_1^h. For each of the asymmetries that follow, two sets of plots will be given: one that demonstrates the step-by-step construction of the asymmetry and one that can be considered a final result plotted in some cases with relevant comparison data.

4.5.1 $A_1(x)$

Figures 4.10 and 4.11 give the step-by-step construction of inclusive A_1 and semi-inclusive A_1^h in nine x bins. One can see the apparent error bar inflation incurred during the unfolding step (comparing $A_{||}$-Raw to $A_{||}$-Born). As was suggested in Section 4.3.5, by properly taking into account statistical covariances, the full statistical strength will be recovered. This is exactly what will be done in Chapter 6 when we use these asymmetries to extract the quark polarizations. Generally speaking, the unfolding and azimuthal corrections have only a small impact on the central values of the asymmetry.

The final nine-bin x-dependent asymmetries for the proton and deuteron targets are plotted in Figures 4.12 and 4.13 and compared with the results from the prior HERMES $\Delta q(x)$ analysis [16]. As expected, the most significant improvement can be seen in the precision of the

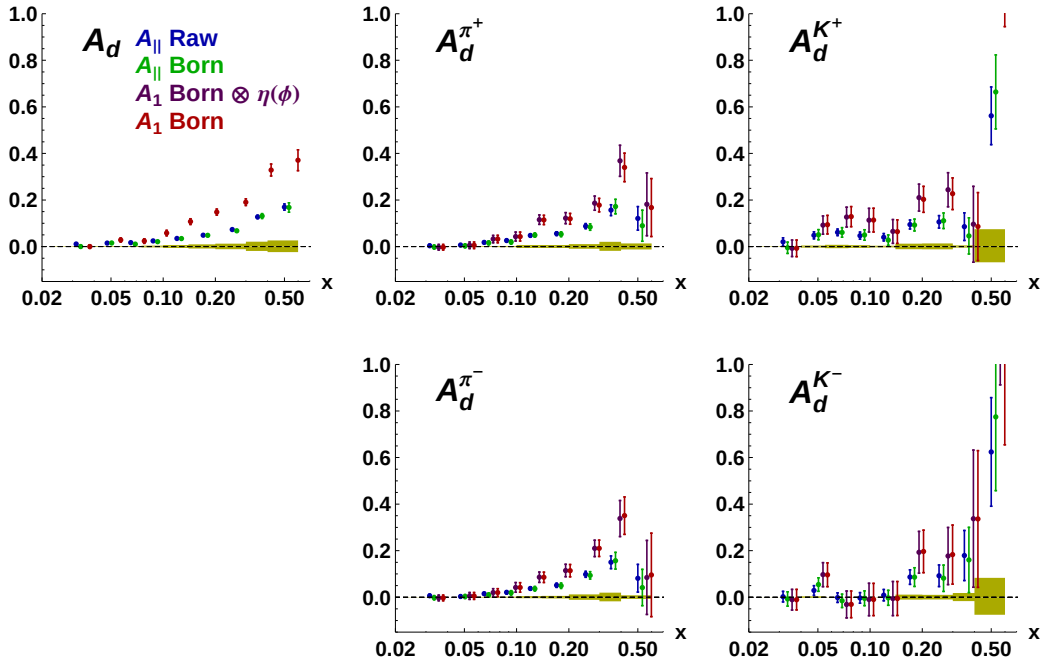

Figure 4.11: A_{1d} in stages. See Fig. 4.10 for further description.

semi-inclusive asymmetries from the deuteron target. This is a result of the additional events gained by including the previously excluded semi-inclusive data in the 2-4 GeV momentum range. Also, reducing the lower z cut from 0.2 to 0.1 has improved statistics to some degree on the semi-inclusive asymmetries for both targets.

Differences in the central values can be attributed to several different causes. First, improved data productions with better tracking and calibrations were used. Second, a different and somewhat less robust azimuthal correction was applied to the semi-inclusive asymmetries of the published result. Third, the improved EVT RICH algorithm, which is significantly more successful at identifying hadrons in multi-hadron events, was not previously available.

Finally, analytic fits to these data are shown in Figures 4.14 and 4.15. The simple linear $A_1^{(h)}(x) = A + Bx$ provides a acceptable goodness-of-fit. A quadratic fit (not shown) seems provides little improvement in χ^2/DoF values, improving it for some asymmetries and worsening it (overparameterizing) for others. Furthermore, without data constraining the fit at high-x, the quadratic fit has a tendency to peak and turn over in that region.

4.5.2 Asymmetries in Three Dimensions – $A_1(x, z, p_{h\perp})$

A major thrust of this reanalysis was to explore the benefit of binning in semi-inclusive variables in addition to the traditional inclusive x.

Unlike the 2D $x - p_{h\perp}$ asymmetries of the next section, the individual values for the 3D

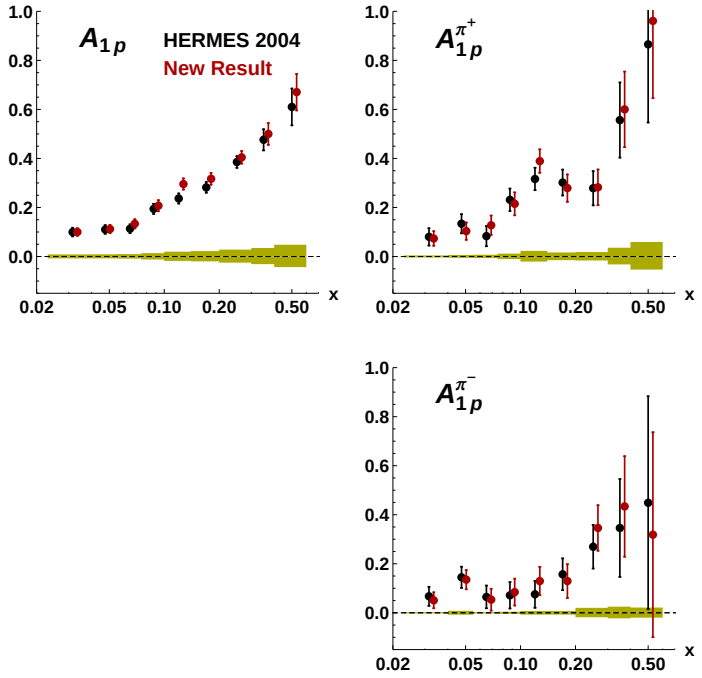

Figure 4.12: $A_{1p}(x)$ (red) compared with the previously published HERMES result [16] of 2004 (black). The yellow band represents the systematic uncertainty which is detailed in Section 4.6.

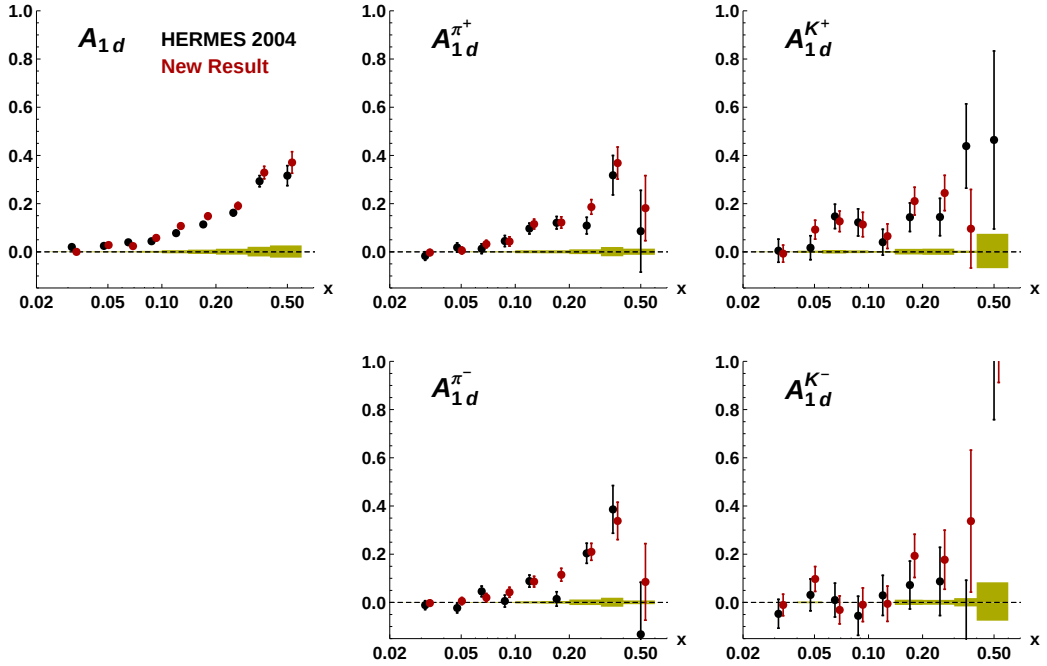

Figure 4.13: $A_{1d}(x)$ (red) compared with the previously published HERMES result [16] of 2004 (black). The highest-x bins for kaons of both charges are off-scale.

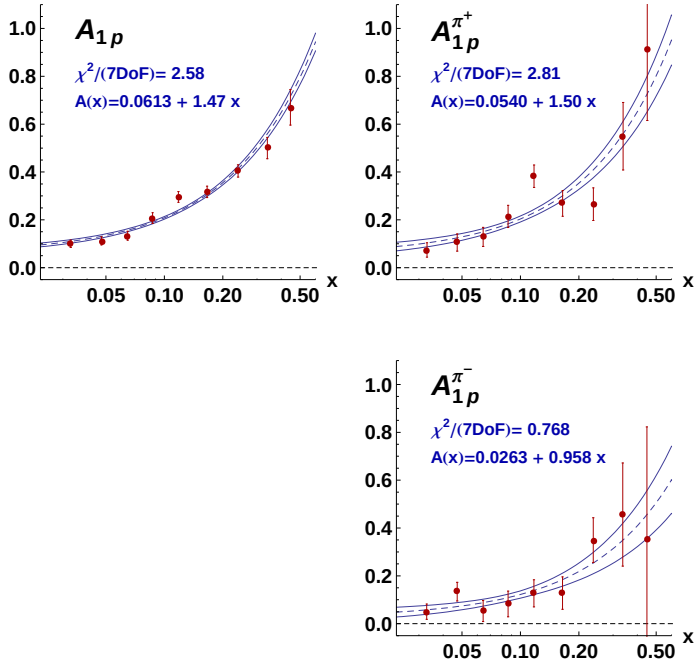

Figure 4.14: The measured $A_{1p}(x)$ points and a linear fit performed using full covariance matrix of the data. The perceived uncertainty is significantly reduced by assuming 1) a smooth model and 2) taking into account the correlations in the data point uncertainties. An acceptable goodness-of-fit was achieved with this simple function (reported in each panel).

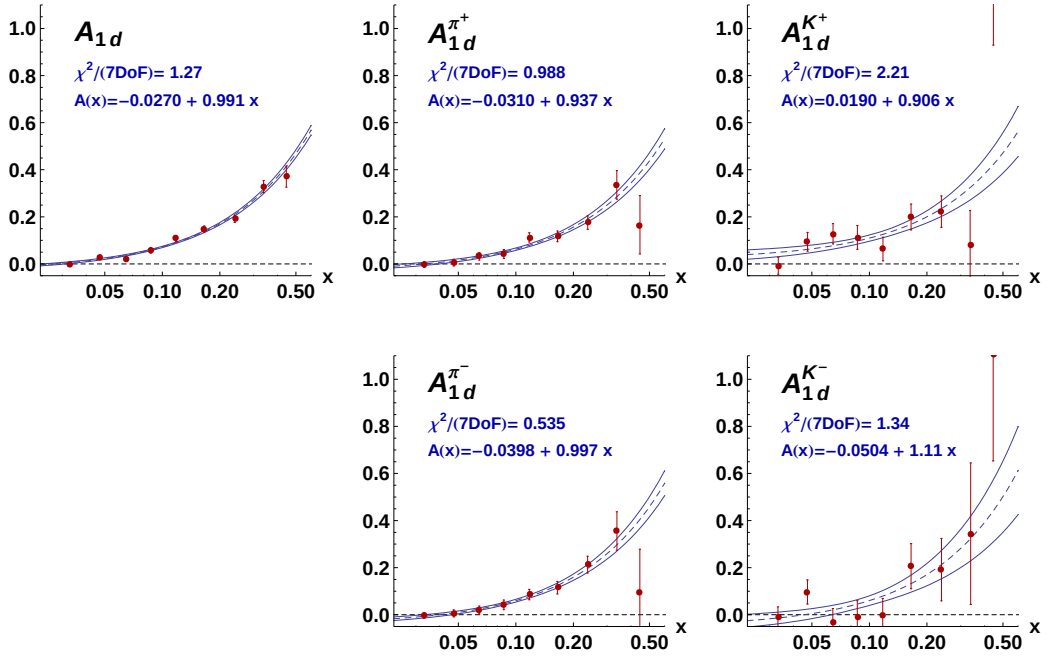

Figure 4.15: The measured $A_{1d}(x)$ points and a linear fit performed using full covariance matrix of the data.

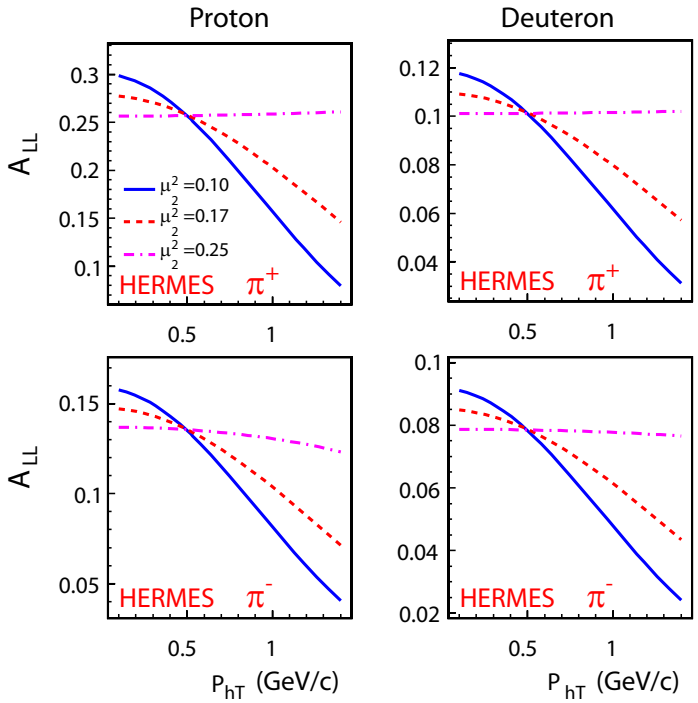

Figure 4.16: Reproduced from [30]. Projections for $A_1(p_{h\perp})$ ("$A_{LL}(p_{hT})$", here) at HERMES kinematics for different scenarios of spin-dependant Gaussian p_T width, μ_2^2. Gaussian widths are assumed for the spin-idependant PDF and fragmentation contributions to the $p_{h\perp}$ dependence.

semi-inclusive asymmetries have error bars large enough that plots of the asymmetries themselves convey very little. Their significance will become more clear in Chapter 6 when they are used to extract the quark polarizations. The values of the 3D binned asymmetries, their uncertainties, and their covariances will be available shortly in publication.

4.5.3 $A_1(x, p_{h\perp})$

The potentially interesting and largely unexplored dependence of A_1 on hadron transverse momentum $p_{h\perp}$ has become a recent source of interest in the SIDIS community. The dependence is expected to be related to the combination of the unknown intrinsic parton k_T and fragmentation-related p_T distributions. Theorists have begun to make calculations of this dependence based on Gaussian-distributed sources of transverse momentum with various widths [30] which have been reproduced in Figure 4.16. First experimental results have begun to appear at conferences by HERMES members and our JLAB colleagues [31, 32].

One potential complication that we've tried to address is that x and $p_{h\perp}$ are significantly correlated. Because of this, it becomes difficult in a 1-dimensional plot of $A_1(p_{h\perp})$ to distinguish the strong dependence of the asymmetry on x from a possible dependence on $p_{h\perp}$. In order to address this issue, we've binned in both variables simultaneously, allowing us to keep x in a much narrower range within each $p_{h\perp}$ bin. The step-by-step construction of the Born asymmetries for

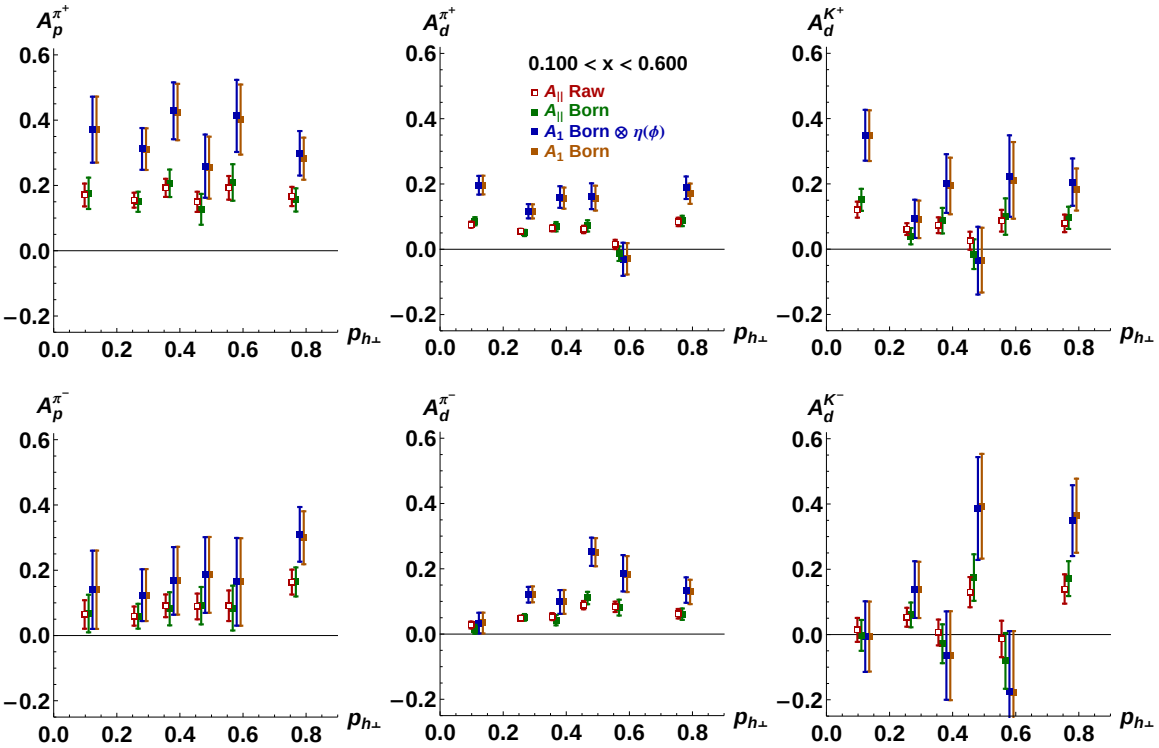

Figure 4.17: Pion and kaon asymmetries binned in $p_{h\perp}$ for the $0.1 < x < 0.6$ x-bin. This is provided to demonstrate the impact of each of the analysis steps. A_1-Born (orange) represents the final acceptance-independent virtual-photon–nucleon asymmetry. $A_1(x, p_{h\perp})$ for all three x-bins is provided in Figure 4.18.

the largest x-bin are provided for all available hadrons from both targets in Figure 4.17. These data, particularly with the combined x-$p_{h\perp}$ binning provided, should allow theorists (the authors of [30], for example) to better constrain the widths of these underlying distributions.

In order to provide a quantitative statement about any potential $p_{h\perp}$ dependence, the final plots have been fit with a number of functional forms with and without this dependence. Their total χ^2 values can be seen in Table 4.1. The fit functions themselves are included in the plots of the final Born asymmetries, Figures 4.18, 4.19, and 4.20, along with their reduced χ^2 (i.e. $\frac{\chi^2}{\text{degree of freedom}}$). These values indicate that a strong $p_{h\perp}$-dependence is excluded by the data.

4.5.4 Hadron Charge Difference Asymmetries

Because of its simple and symmetric structure – one proton and one neutron – the deuteron target provides a number of opportunities to extract otherwise algebraically buried quantities by employing certain symmetry assumptions. The deuteron is *isoscalar*, meaning that when one maps the partons to their isospin conjugates ($u \to d$, $d \to u$, $\bar{u} \to \bar{d}$, and, $\bar{d} \to \bar{u}$), the result remains a deuteron.

The hadron charge difference asymmetry of the deuteron, $A_{1\,d}^{h^+-h^-}$, is one way to take

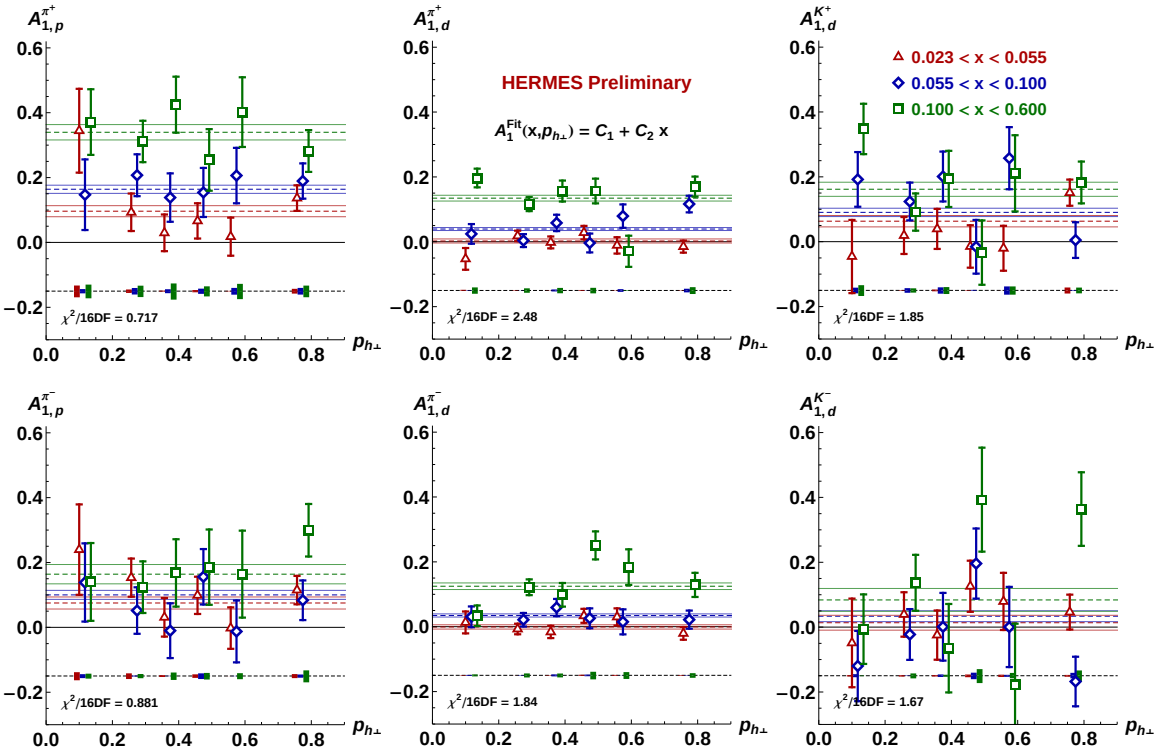

Figure 4.18: Final result for $A_1(x, p_{h\perp})$ fit with a simple linear function in x (dashed) with no $p_{h\perp}$ dependence. Each fit curve is bounded by a 1-σ error band of the same color. The small solid rectangles represent the systematic uncertainty for the associated data point. The reduced χ^2 values given suggest that this parameterization is adequate to describe the data. Within the precision available, A_1 has no $p_{h\perp}$ dependence.

	$p \to \pi^+$	$p \to \pi^-$	$d \to \pi^+$	$d \to \pi^-$	$d \to K^+$	$d \to K^-$
$\chi^{2\ (NDF=16)}_{C_1^h+C_2^h x}$	11.5	14.1	39.7	29.5	29.5	26.7
$\chi^{2\ (NDF=15)}_{C_1^h+C_2^h x+C_3^h p_{h\perp}}$	11.5	13.8	38.2	27.9	29.1	24.4
$\chi^{2\ (NDF=12)}_{C_1^h+C_2^h x+C_3^h p_{h\perp} +C_4^h x^2+C_5^h p_{h\perp}^2+C_6^h x p_{h\perp}}$	7.78	5.31	36.4	14.9	20.1	16.9

Table 4.1: Total χ^2 for each functional form fit to the $A_1(x, p_{h\perp})$ data points for each target–final-state-hadron combination (see Figures 4.18, 4.19, and 4.20). The higher-order fit functions yield little improvement over a constant fit suggesting little or no $p_{h\perp}$ dependence of the asymmetry. As one would expect, the total χ^2 is reduced when additional polynomial coefficients are added while in this case χ^2 per degree of freedom remains relatively constant (see plots).

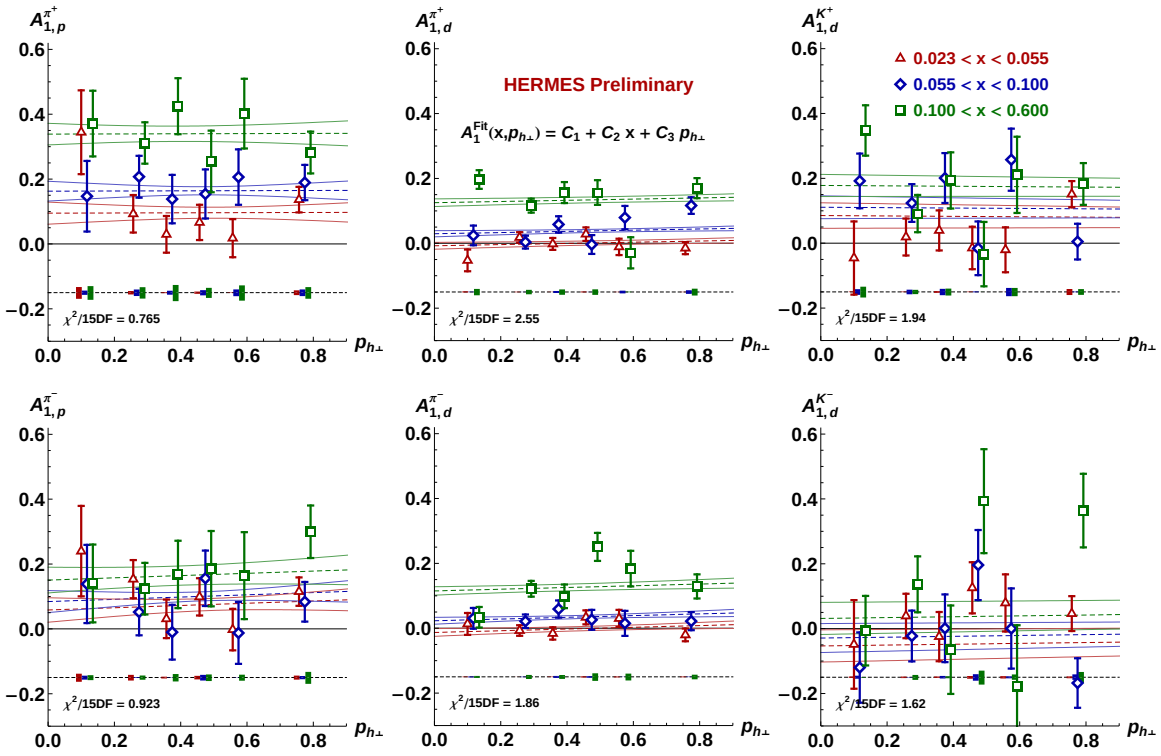

Figure 4.19: Final $A_1(x, p_{h\perp})$ fit with a linear function of both x and $p_{h\perp}$ (dashed). Each fit curve is bounded by a 1-σ error band of the same color. The reduced χ^2 visible in each panel suggests (when compared to Fig 4.18) that within the precision of the data, no $p_{h\perp}$ dependence is indicated.

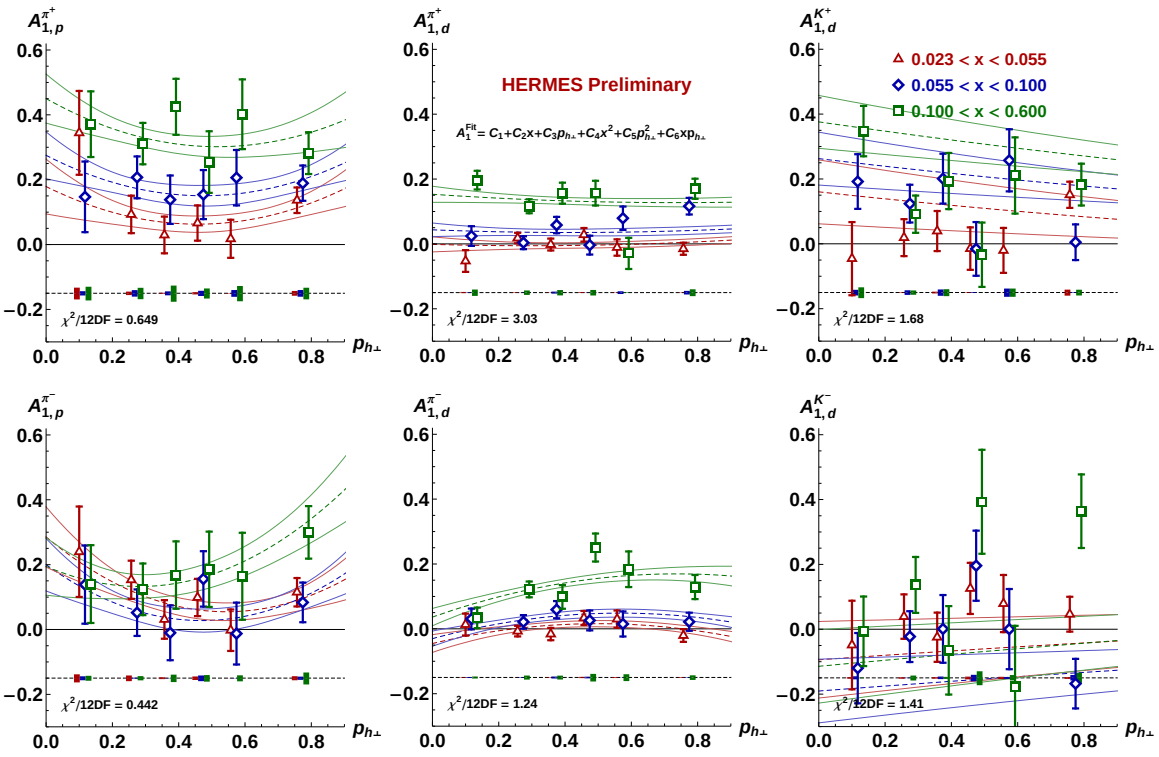

Figure 4.20: $A_1(x, p_{h\perp})$ fit with a quadratic function of both x and $p_{h\perp}$ (dashed). Each fit curve is bounded by a 1-σ error band of the same color. With the exception of the π^- from the deuteron target, there is no improvement in the reduced χ^2 of this fit compared to either of the simpler fits.

advantage of this symmetry. Under certain symmetry assumptions, particularly charge-conjugation invariance in the fragmentation functions, $A_{1\,d}^{h^+-h^-}$ is equal to the polarization of the valence quarks, $(\Delta u_v + \Delta d_v)/(u_v + d_v)$. The charge difference asymmetry not only provides a Monte-Carlo–free crosscheck of the same quantity which will be computed in Chapter 6 using the purity method, but will also allow us to make a critique of the assumptions involved. The recent HERMES isoscalar $\Delta s(x)$ analysis [33] is based on a similar concept. Increasingly, these types of analyses are being proposed in order to make precision measurements [34, 35] – at times with limited consideration of the model-dependences involved.

Ah– the Symmetry!

Under the assumption of charge conjugation invariance in fragmentation, the hadron charge-difference asymmetry of the deuteron is equal to the quotient of the sums of the polarized and unpolarized valence parton distributions. To see this, we write the asymmetry:

$$A_{1\ d}^{h^+-h^-}(x) = \frac{\Delta\sigma_d^{h^+-h^-}(x)}{\sigma_d^{h^+-h^-}(x)} \equiv \frac{\Delta\sigma_d^{h^+}(x) - \Delta\sigma_d^{h^-}(x)}{\sigma_d^{h^+}(x) - \sigma_d^{h^-}(x)}. \tag{4.33}$$

Let us focus our attention on the denominator. For the deuteron:

$$\begin{aligned}
\sigma^{h^+-h^-}(x) &= \sum_q e_q^2\ q(x)\ \left(D_q^{h+} - D_q^{h-}\right) + \sum_q e_q^2\ q_n(x)\ \left(D_q^{h+} - D_q^{h-}\right) \\
&= \tfrac{1}{9}\Big[\\
\text{proton} \quad &\Big\{ \quad 4u(x)\left(D_u^{h+} - D_u^{h-}\right) + d(x)\left(D_d^{h+} - D_d^{h-}\right) \\
&\quad + 4\bar{u}(x)\left(D_{\bar{u}}^{h+} - D_{\bar{u}}^{h-}\right) + \bar{d}(x)\left(D_{\bar{d}}^{h+} - D_{\bar{d}}^{h-}\right) \\
&\quad + \ \ s(x)\left(D_s^{h+} - D_s^{h-}\right) + \bar{s}(x)\left(D_{\bar{s}}^{h+} - D_{\bar{s}}^{h-}\right) \\
\text{neutron} \quad &\Big\{ \quad + 4d(x)\left(D_u^{h+} - D_u^{h-}\right) + u(x)\left(D_d^{h+} - D_d^{h-}\right) \\
&\quad + 4\bar{d}(x)\left(D_{\bar{u}}^{h+} - D_{\bar{u}}^{h-}\right) + \bar{u}(x)\left(D_{\bar{d}}^{h+} - D_{\bar{d}}^{h-}\right) \\
&\quad + \ \ s(x)\left(D_s^{h+} - D_s^{h-}\right) + \bar{s}(x)\left(D_{\bar{s}}^{h+} - D_{\bar{s}}^{h-}\right) \quad \Big],
\end{aligned} \tag{4.34}$$

where q_n are the isospin-rotated neutron PDFs ($u_n = d, d_n = u, \bar{u}_n = \bar{d}, \bar{d}_n = \bar{u}$). We now apply charge-conjugation to all of the antiquark fragmentation functions: we assume $D_q^{h^+} = D_{\bar{q}}^{h^-}$.

$$\begin{aligned}
&= \tfrac{1}{9}\Big[\quad 4u(x)\left(D_u^{h+} - D_u^{h-}\right) + d(x)\left(D_d^{h+} - D_d^{h-}\right) \\
&\quad - 4\bar{u}(x)\left(D_u^{h+} - D_u^{h-}\right) - \bar{d}(x)\left(D_d^{h+} - D_d^{h-}\right) \\
&\quad + \ \ s(x)\left(D_s^{h+} - D_s^{h-}\right) - \bar{s}(x)\left(D_s^{h+} - D_s^{h-}\right) \\
&\quad + 4d(x)\left(D_u^{h+} - D_u^{h-}\right) + u(x)\left(D_d^{h+} - D_d^{h-}\right) \\
&\quad - 4\bar{d}(x)\left(D_u^{h+} - D_u^{h-}\right) - \bar{u}(x)\left(D_d^{h+} - D_d^{h-}\right) \\
&\quad + \ \ s(x)\left(D_s^{h+} - D_s^{h-}\right) - \bar{s}(x)\left(D_s^{h+} - D_s^{h-}\right) \quad \Big]
\end{aligned} \tag{4.35}$$

The reader should be cautioned at this point that this *reasonable sounding* symmetry may be significantly violated due to the influence of the target remnant. This topic will be addressed in some detail in Chapter 5.

Collecting like terms and assuming that $s(x) - \bar{s}(x)$ is small with respect to the non-strange

PDFs we get:

$$\begin{aligned}\sigma^{h^+-h^-}(x) &= \frac{1}{9}\left[\left(u(x)-\bar{u}(x)+d(x)-\bar{d}(x)\right)\times\left(\,4\left(D_u^{h+}-D_u^{h-}\,\right)+\left(D_d^{h+}-D_d^{h-}\right)\right)\right] \\ &= \frac{1}{9}\left[\left(u_v(x)+d_v(x)\right)\times\left(\,4\left(D_u^{h+}-D_u^{h-}\right)+\left(D_d^{h+}-D_d^{h-}\right)\right)\right]. \end{aligned} \tag{4.36}$$

Following the same algebra,

$$\Delta\sigma^{h^+-h^-}(x) = \frac{1}{9}\left[\left(\Delta u_v(x)+\Delta d_v(x)\right)\times\left(\,4\left(D_u^{h+}-D_u^{h-}\right)+\left(D_d^{h+}-D_d^{h-}\right)\right)\right], \tag{4.37}$$

leaving us with:

$$\begin{aligned}A_{1\,d}^{h^+-h^-}(x) &= \frac{\Delta\sigma_d^{h^+-h^-}(x)}{\sigma_d^{h^+-h^-}(x)} \\ &= \frac{\Delta u_v(x)+\Delta d_v(x)}{u_v(x)+d_v(x)}. \end{aligned} \tag{4.38}$$

Results

The hadron charge difference asymmetries are given step-by-step in Figure 4.21. The final Born asymmetries are plotted with results from the COMPASS collaboration in 4.22. As previously mentioned, the interpretation of the results and the validity of the symmetry assumptions will be discussed in Chapter 5 and a comparison of these asymmetries with the purity-extracted valence quark polarization can be found in Section 6.4.

4.6 Systematic Uncertainties

When compared to the systematic uncertainties that we will consider in the following chapters for the quark polarizations, the systematic uncertainties of asymmetries are relatively straightforward. They are first of all dominated by the uncertainty in the average polarizations of beam and target. Though we will check the size of each potentially significant source of uncertainty, they will all prove to be negligible contributions when added in quadrature to the polarization uncertainty.

4.6.1 Polarization

The average uncertainty on the beam and target polarization as estimated by their respective experts at HERMES are summarized in Table 4.2. As the beam and target polarization appear everywhere as a product, their *fractional* uncertainties can be combined in quadrature. Furthermore, as the average polarization always appears in combination with the luminosity we

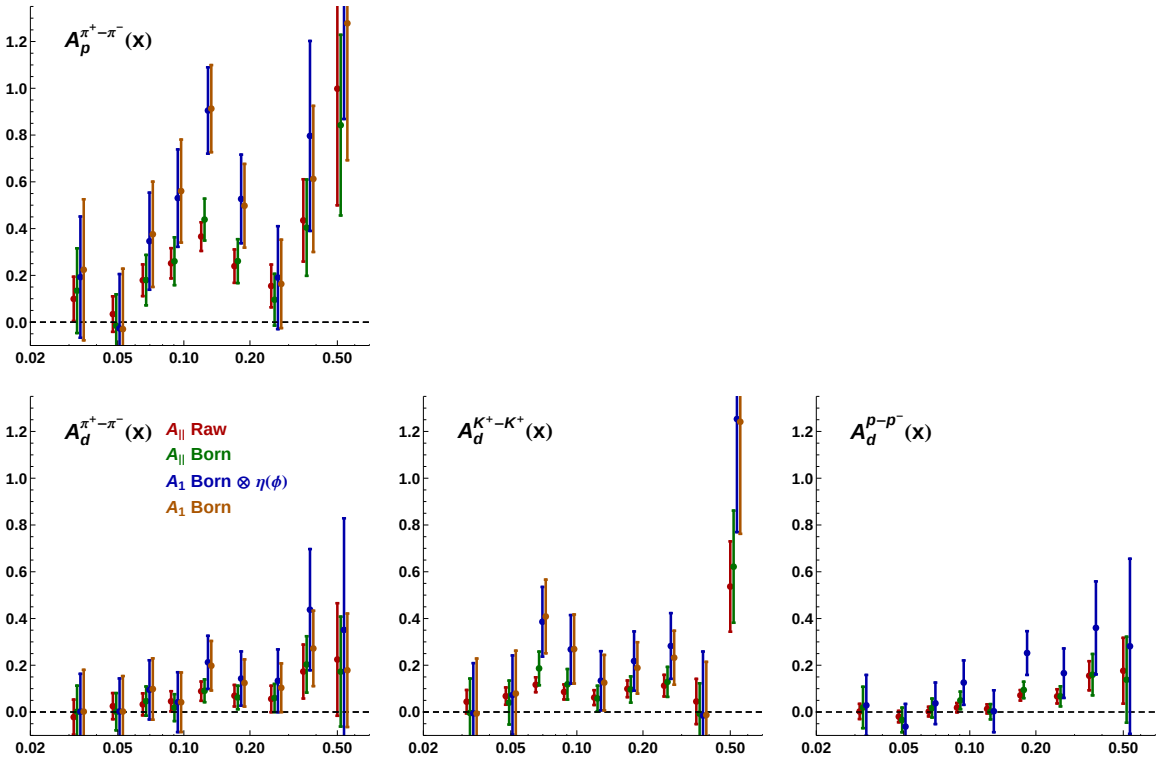

Figure 4.21: The hadron charge-difference asymmetries for all available targets and final state hadrons. They are plotted at several different stages of analysis so that the effect of kinematic unfolding, kinematic/depolarization corrections, and the azimuthal acceptance correction can be seen individually. Note that there are as of yet no $\cos(\phi)$ moments available for the proton production asymmetry so no azimuthal correction is applied.

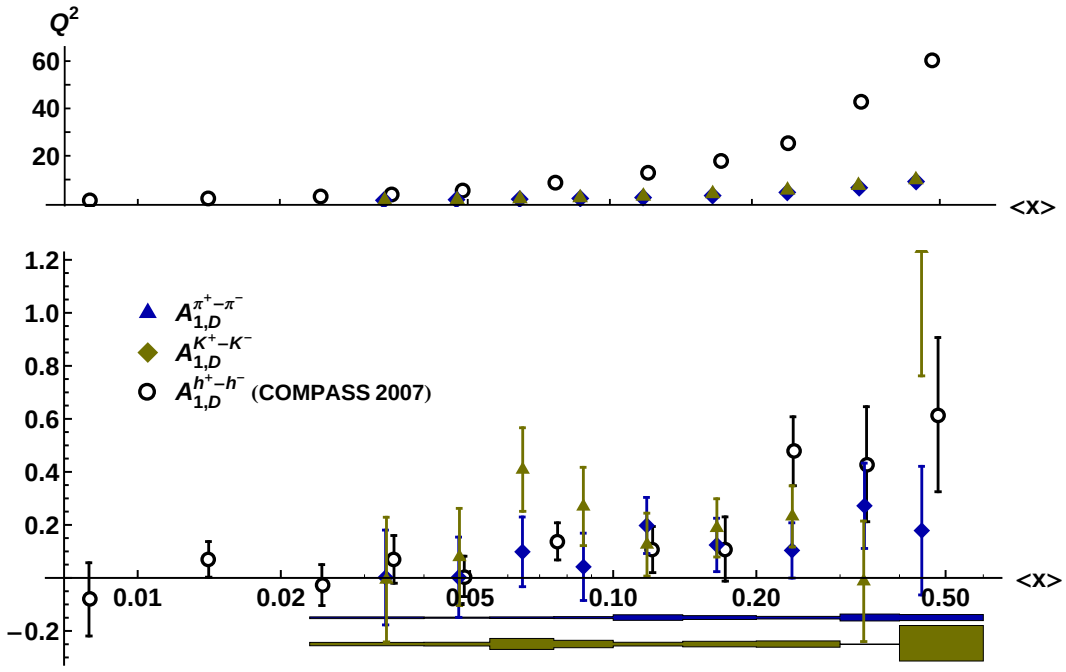

Figure 4.22: Pion and kaon charge difference asymmetries of the deuteron compared with COMPASS results for mixed hadrons [36]. The bands at the bottom of the plot represent the systematic uncertainty on each asymmetry.

	1996	1997	1998	1999	2000
$\delta P_T/P_T$	0.055	0.038	0.075	0.070	0.035
$\delta P_B/P_B$	0.034	0.034	0.034	0.018	0.019
$(\delta P/P)_{\text{tot}}$	0.065	0.051	0.082	0.072	0.040

Table 4.2: Fractional uncertainties of beam and target and their quadrature sum by year.

can write the total polarization-weighted luminosity as follows:

$$\left(L\ P_{\uparrow\uparrow(\uparrow\downarrow)}\right)_{\text{tot}} \;=\; \sum_{i:\{\text{years}\}} L_{i\ \uparrow\uparrow(\uparrow\downarrow)}\ P_i\ \left(\ 1 \pm (\delta P/P)_{\text{tot}\ i}\right). \tag{4.39}$$

The systematic error band is produced by computing azimuthally-corrected Born asymmetries for both values of $\left(L\ P_{\uparrow\uparrow(\uparrow\downarrow)}\right)_{\text{tot}}$.

4.6.2 RICH Unfolding

As with many systematic uncertainties, the RICH systematic is produced by exploring ambiguities in the analysis procedure. For RICH hadron identification there are two such ambiguities:

1. A Monte Carlo event generator is necessary to build the P-matrices. Neither `disNG` nor `PYTHIA` perfectly reproduces HERMES data multiplicities. As either generator adequately populates the momentum and track-multiplicity phase space on which it's believed that the

P-matrices should depend, either should be acceptable. To characterize any difference between these two generators, P-matrices are generated using both.

2. There is ambiguity in the source of the background file which characterizes the likelihood of hits from untracked particles for each PMT. The default file is tabulated from PMT hits in data events where there are no tracks in the detector half. Alternative background files are generated from Monte Carlo – either `disNG` or `PYTHIA`. P-matrices are generated with each of these background files.

The `disNG_ownBKG` file is the standard P-matrix used in this analysis and is expected to be the most accurate. By generating asymmetries using each of these alternative P-matrices and comparing to `disNG_ownBKG`, one can estimate the systematic uncertainty from RICH unfolding which can be seen in Figure 4.23. This source of uncertainty is found to contribute negligibly to the total systematic uncertainty of the asymmetry.

4.6.3 Azimuthal Correction

Systematic uncertainties on the semi-inclusive asymmetries from the azimuthal correction are tricky to compute exactly. While the $\cos(\phi)$ and $\cos(2\phi)$ moments used are provided with uncertainties and covariances, it is not immediately clear how to propagate them to the multiplicative correction, C_ϕ^h, which was computed by taking the ratio of Monte Carlo asymmetries with and without this $\cos(\phi)$ weighting.

A reasonable estimate can be made by observing that in Fig. 4.7, and the x-projections in particular, the uncertainty is at worst approximately 50% of the value of the moment. Considering that the size of the azimuthal correction (in 4.10, for example) is quite small, one can expect that a 50% uncertainty on the correction would have little effect on the final asymmetries. It is particularly clear that the impact of this uncertainty is negligible when one considers that it should be added to the total systematic in quadrature.

4.6.4 Charge Symmetric Background

A large fraction of the non-DIS background events are produced in equal parts e^+ and e^-. Monte Carlo studies indicate that these leptons primarily originate from decays of π^0 but can also be produced through pair production from high-energy radiated photons. These charge symmetric sources were shown to dominate asymmetric sources – misidentified hadrons, for example. While these leptons can be misidentified as coming from DIS events, by accumulating events containing leptons of charge *opposite* to that of the beam and exploiting the charge symmetry of the background sources, we can easily estimate or remove the contribution from their like-charged counterparts. Fractional yields for charge symmetric contributions are given in Table 4.3. These

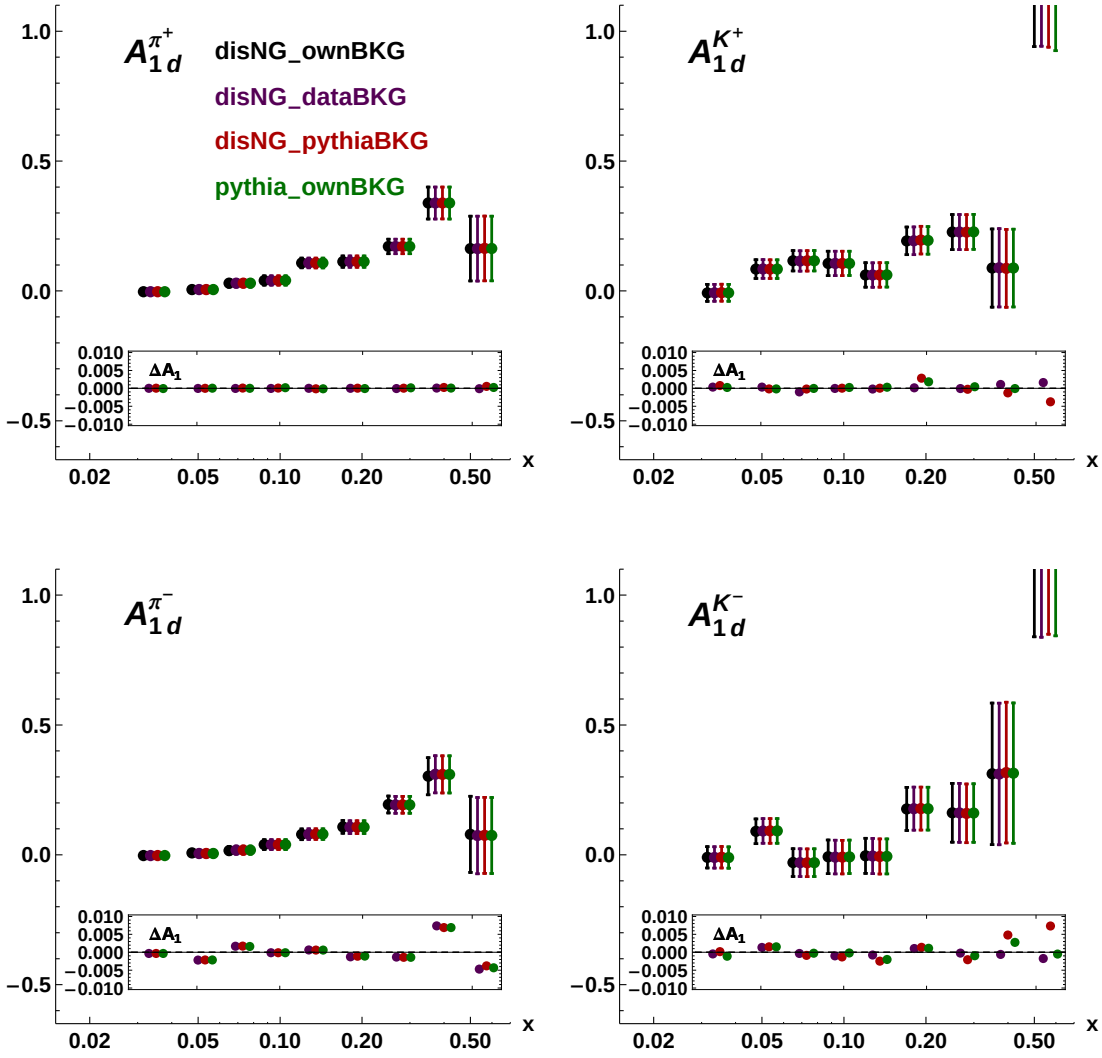

Figure 4.23: Comparison of semi-inclusive asymmetries of the deuteron produced using four different sets of P-matrices in order to establish a systematic uncertainty for the RICH unfolding. As the differences are tiny, ΔA_1 in the inset panel is provided which is the difference between "disNG_ownBKG", the standard P-matrix, and the three variations.

x-bin	1	2	3	4	5	6	7	8	9
$N^{\mathrm{BK}}_{\uparrow\uparrow}/N_{\uparrow\uparrow}$	0.062	0.027	0.013	0.005	0.002	0.001	0	0	0
$N^{\mathrm{BK}}_{\uparrow\downarrow}/N_{\uparrow\downarrow}$	0.064	0.027	0.013	0.006	0.002	0	0	0	0

Table 4.3: Fractional charge symmetric background contribution to yields.

processes contribute at worst 6% to the yields (at lowest x) and make virtually no contribution in the asymmetry.

Chapter 5

Fragmentation and the Purity Method

Unlike e^+e^- scattering, which always provides fragmentation functions $D_q^h(z)$ and $D_{\bar{q}}^h(z)$ in combination, or Drell-Yan scattering ($p\bar{p} \to l^+l^-$), which always provides parton distributions $q(x)$ and $\bar{q}(x)$ in combination, DIS gives us the unique opportunity to study fragmentation functions and parton distributions from a individual struck quark or antiquark. The inevitable trade-off is that we are always provided with the fragmentation function and parton distribution function in combination – and unlike the clean, unbiased fragmentation of e^+ e^-, fragmentation in DIS is plagued by a memory of the contents of the target, potentially breaking the pristine symmetries offered by pure QCD.

This chapter will explore the various methods by which one can attempt to disentangle the fragmentation and parton distribution functions that come intertwined in the structure functions $F_1^h h$ and g_1^h which we measure through experimental spin asymmetries.

5.1 Untangling the Complexity: Three Complementary Strategies

There have been several strategies developed to help us disentangle the fragmentation functions from the parton distributions that we seek to extract. Each of these methods requires certain assumptions, which impose model-dependent systematic uncertainties on extracted parton distributions.

Assumptions of Fragmentation Symmetry As we've seen with the hadron charge-difference asymmetries of Chapter 4, certain symmetry assumptions about the fragmentation process

can cause useful cancellations of fragmentation functions. This grants access to combinations of parton distributions. The work of Christova and Leader [34, 35] and other earlier work [37] has motivated very straight-forward leading-order analyses of semi-inclusive data which take advantage of these assumptions. The reader is urged hoverer to approach these often mild-sounding assumptions with a degree of caution. As we will see in section 5.2, even the often trusted *charge-conjugation symmetry* is potentially broken in ways that make it difficult to recover with the application of simple kinematic restrictions (i.e. large-W^2 or moderate-z). That being said, making such calculations is perfectly acceptable provided that these assumptions are made clear and that a reasonable attempt at estimating the assumption-related uncertainty is made.

Modeled Fragmentation The *Purity Method*– the backbone of the HERMES 5-flavor $\Delta q(x)$ extraction which will make up the final chapter of this work, depends upon the physically, but also phenomenologically motivated Lund-String fragmentation model to *flavor-tag* semi-inclusive events by correlating struck-quark flavors with final-hadron types through a leading-order formalism. This Lund-String model, `JETSET`, is tuned to reproduce the unpolarized multiplicities observed at HERMES. While the model doesn't assume to reproduce the dynamics of the actual fragmentation process (if it could, no tuning would be required!), it is not unreasonable to believe that when properly tuned, the purities it produces resemble reality at HERMES kinematics. Furthermore, no explicit assumption of any fragmentation symmetry is necessary meaning that this method produces fragmentation with a reasonable degree of target-remnant related symmetry breaking. As we will see in Section 5.3.3, assessing the systematic uncertainty of this model is a complex problem requiring an evaluation of the correlated multi-parameter tune uncertainty and of its impact on the final extracted result.

NLO Analysis At next-to-leading order in QCD, the spin-dependent gluon distribution $\Delta g(x)$ is explicitly included with the quark helicity distributions in the formulation of $g_1(x, Q^2)$. By combining *inclusive* DIS (avoiding fragmentation issues completely) with results from hyperon beta decay, combinations of spin-dependent parton distributions like the total quark spin, $\Delta\Sigma$, and combined quark-antiquark distributions, $\Delta q + \Delta\bar{q}$, can be extracted [38, 13]. Additionally, NLO formulations of the experimentally observable structure functions necessarily contain arbitrary (though theoretically well defined) choices of scale and scheme.

5.2 Limitations of Fragmentation Symmetries

As mentioned before, it is a common strategy to make assumptions about fragmentation symmetry as they are motivated by symmetries of QCD, are known to hold at suitably high Q^2, and can

cause considerable algebraic simplification often leading to observables that can be related directly to combinations of parton distributions. The first example is *charge conjugation symmetry* in the fragmentation functions:

$$D_q^{h^+}(z) \approx D_{\bar{q}}^{h^-}(z). \tag{5.1}$$

Another common symmetry is *isospin symmetry*, which is the assumption that fragmentation functions should be invariant under the exchange of 1) u and d and 2) $\bar{u}$ and $\bar{d}$, including the valence composition of the final state hadron observed. This gives us

$$\begin{aligned} D_u^{\pi^+}(z) &\approx D_d^{\pi^-}(z), \\ D_u^{\pi^-}(z) &\approx D_d^{\pi^+}(z), \\ D_{\bar{u}}^{\pi^-}(z) &\approx D_{\bar{d}}^{\pi^+}(z), \quad \text{and} \\ D_{\bar{u}}^{\pi^+}(z) &\approx D_{\bar{d}}^{\pi^-}(z). \end{aligned} \tag{5.2}$$

The scheme of *favored* and *disfavored* fragmentation – that is, identical fragmentation to a hadron with or without the struck quark in its valence composition respectively – is the most presumptive of these fragmentation assumptions. It includes both the charge-symmetry and isospin fragmentation assumptions. The favored/disfavored symmetry for pion fragmentation functions can be summarized as follows:

$$D_{\text{fav}}(z) = D_u^{\pi^+}(z) \approx D_d^{\pi^-}(z) \approx D_{\bar{u}}^{\pi^-}(z) \approx D_{\bar{d}}^{\pi^+}(z) \tag{5.3}$$

$$D_{\text{disfav}}(z) = D_u^{\pi^-}(z) \approx D_d^{\pi^+}(z) \approx D_{\bar{u}}^{\pi^+}(z) \approx D_{\bar{d}}^{\pi^-}(z) \tag{5.4}$$

The fragmentation process, while presumably governed by the QCD Lagrangian, occurs in its long-range, non-perturbative limit. The result of this is that first-principle calculations become virtually impossible and hence a measure of the validity of these symmetries is theoretically inaccessible. While the charge-conjugation symmetry is obeyed by both QED and QCD, and hence in the $e^+e^-(\rightarrow q\bar{q})$ scattering, in ep scattering, the presence of the proton remnant as an initial state of the fragmentation process breaks that symmetry for the fragmentation functions.

Consider for a moment the extreme case of the single pion production, i.e. $z \sim 1$. While a π^+ can easily be created leaving a stable neutron, single π^- production is impossible as it would likely leave the unstable Δ^{++} (which by virtue of having an additional decay hadrons is inconsistent with the π^- carrying all the virtual photon's energy). Even with more relaxed kinematic requirements, the quark content of the target remnant places significant constraints on the energy requirements for the production of various final state hadrons. These effects clearly diminish as scattering scale

increases, however the scale at which they become insignificant is the subject of ongoing debate.

The Hadron Charge Difference Asymmetry

It seems the opportune moment then to consider the validity of the symmetry assumptions we made in Section 4.5.4 for the hadron charge difference asymmetries – assumptions that encouraged us to equate

$$A_{1\ d}^{h^+-h^-} \quad \text{and} \quad \frac{\Delta u_v(x) + \Delta d_v(x)}{u_v(x) + d_v(x)}. \tag{5.5}$$

As many fragmentation functions in DIS are poorly constrained (particularly in a model-independent way), and what is known from e^+e^- can't be applied without making symmetry assumptions, it is difficult to quantify the degree of symmetry breaking.

We can, however, attempt to estimate the approximate degree of symmetry breaking using our Lund Monte Carlo model (which will be described in more detail in Section 5.3.1). While the Monte Carlo is designed around assumptions of its own and *tuned* to reflect HERMES kinematics, it *does not* assume any fragmentation function symmetry related to charge-conjugation invariance or any of the other symmetries appearing in the previous section.

Figure 5.1 shows hadron charge-difference asymmetries computed from Born Monte Carlo deuteron yields subject to SIDIS kinematic requirements (but generated without HERMES acceptance requirements). The presumably equivalent quantity, $\frac{\Delta u_v(x)+\Delta d_v(x)}{u_v(x)+d_v(x)}$, computed from the GRSV [39] polarized and CTEQ6 [40] unpolarized parton distributions, which are the inputs to the Monte Carlo, is overlaid. One can see that both the pion and kaon charge-difference asymmetries are systematically lower than the PDF combination formed from their own PDF inputs. Furthermore, this discrepancy seems unaffected by either increasing average Q^2 or increasing the minimum W^2 requirement. One might expect either of these parameters to reduce the fragmentation process' "memory" of the target, and hence increase the fragmentation symmetry which is required for Equation 5.5 to hold.

Fortunately, the amount of symmetry breaking suggested by this Monte Carlo study is sufficiently small compared to the statistical precision of the final measured hadron charge-difference asymmetries of 4.5.4 that we can comfortably compare them directly to the purity-extracted valence distribution ratio in chapter 6. One should, however, approach skeptically the work of those proposing to base precision measurements on such symmetry assumptions.

Symmetry Breaking in the Fragmentation Functions Themselves

Using `JETSET`, we can estimate the fragmentation functions themselves in order to get a more direct estimate of the charge-conjugation symmetry breaking. Using our knowledge of the identity of the struck quark available in Monte Carlo events, we can compute the fragmentation functions

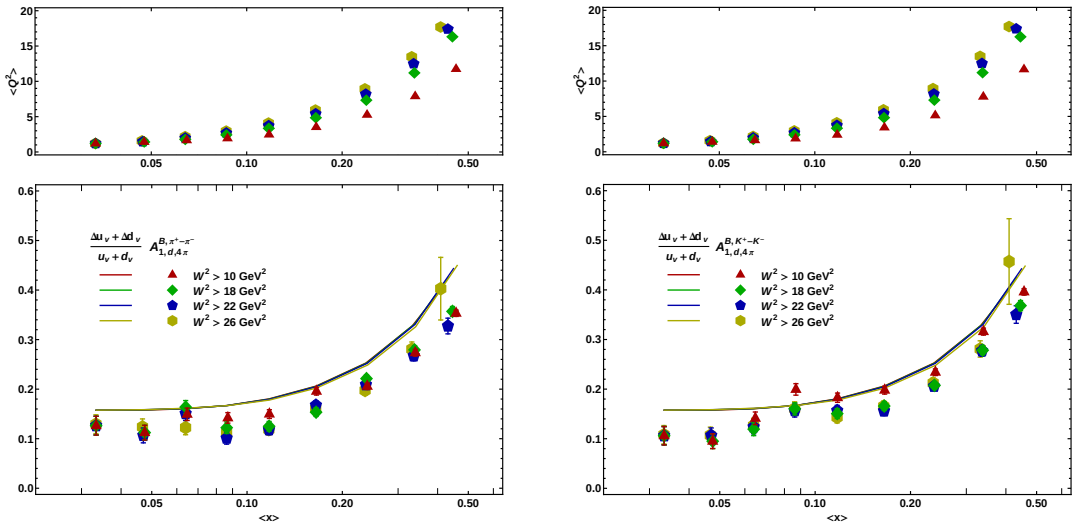

Figure 5.1: The pion (left) and kaon (right) charge-difference asymmetries of the deuteron computed from Monte Carlo yields compared with the which the ratio of the polarized to unpolarized valence distributions computed from the MC input distributions. The difference asymmetry (points) and valence distribution ratio (lines) should be identical under perfect charge-conjugation symmetry in fragmentation. They are provided at several values of the minimum W^2 cut which is typically expected to improve these symmetries.

themselves as follows:

$$\mathcal{D}_q^h(x,z) = \frac{\mathcal{N}_q^h(x,z)}{dz\ \mathcal{N}_q(x,z)}, \tag{5.6}$$

where $\mathcal{N}$ represents a yield, dz is the z-bin width, and once again calligraphic script reminds us that these are Monte Carlo quantities. Figure 5.2 presents two tests of the charge conjugation symmetry. The upper panels compare (the favored) $\mathcal{D}_u^{\pi^+}$ and $\mathcal{D}_{\bar{u}}^{\pi^-}$, the lower (the disfavored) $\mathcal{D}_u^{\pi^-}$ and $\mathcal{D}_{\bar{u}}^{\pi^+}$. The plots on the left show the z-dependence of these fragmentation functions and their ratios.

Looking at the ratios of these charge-conjugation pairs, one can see several interesting features. First, as one might expect from our previous example, the symmetries are most strongly broken at high-z. In this regime, semi-exclusive processes begin to dominate, with very few string breaks separating the struck quark from the target remnant.However, the ratio also deviates from one significantly at low-z. For both charge-conjugate fragmentation function pairs, the symmetries are only reasonably observed (at the 5% level) over a narrow range in z. Furthermore, according to our model *the favored (upper) and disfavored (lower) symmetries are symmetric over different and non-overlapping ranges in* z. To the author's knowledge, this possibility has never been considered in the literature where suitable symmetry-preserving kinematic cuts are estimated.

Just as we saw with the Monte Carlo difference asymmetries of Figure 5.1, there is no obvious choice of kinematic cuts which safely excludes regions of symmetry violation. Increasing the minimum W^2 improves the symmetry in the most violated regions (high and low z), but only

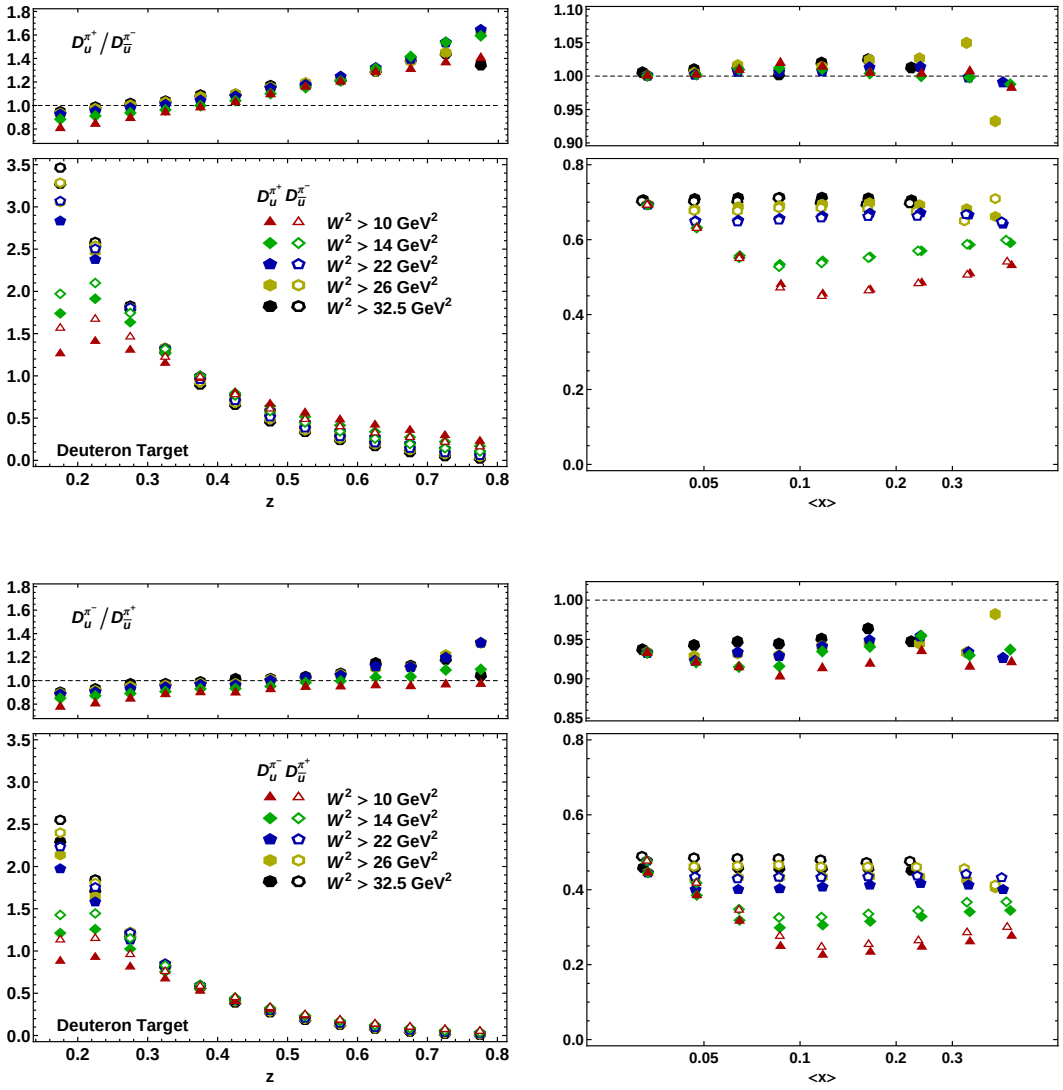

Figure 5.2: Comparisons of charge-symmetric favored $\mathcal{D}_u^{\pi^+}$ and $\mathcal{D}_{\bar{u}}^{\pi^-}$ (above) and disfavored $\mathcal{D}_u^{\pi^-}$ and $\mathcal{D}_{\bar{u}}^{\pi^+}$ (below). The fragmentation functions are plotted as functions of z (left) and x (right) and ratios are provided which directly reflect the degree of charge conjugation symmetry. Points are provided for several values of the minimum W^2 cut generally expected to improve these symmetries.

up to a point.

It should be pointed out that while cutting into z significantly on both the high and low ends may restore symmetry when integrated over z, because the narrow regions of symmetry differ between the favored and disfavored case one would almost certainly have difficulty finding a range of symmetry for both and would likely err on the side of including compensating regions of symmetry breaking.

Finally, looking to the functions plotted vs. x, they appear almost flat. It is interesting to note that as a function of x, the favored comparison appears almost symmetric – suggesting either that the bulk of the events come from the range, $0.3 < z < 0.5$, or, more likely, that some of the broken symmetry on either side of that z-range is canceling. The disfavored comparison is also flat as function of x but the ratio clearly deviates significantly from one – which suggests, as one would expect, that the majority of the disfavored fragmentation occurs at low-z.

5.3 The Purity Method

The Purity Method lies at the heart of the 5-flavor $\Delta q(x)$ extraction which will be the subject of Chapter 6. It takes advantage of the identity of final state hadrons and the event and track kinematics to recover information about the struck quark. We write the leading order expression for the measured semi-inclusive asymmetry as follows:

$$A_{1\ t}^{h}(x) = \frac{\sum_q \ e_q^2 \ \Delta q(x) \ D_{q\ t}^{h}(z, p_{h\perp})}{\sum_{q'} \ e_{q'}^2 \ q'(x) \ D_{q'\ t}^{h}(z, p_{h\perp})} = \sum_q \ P_{q\ t}^{h}(x, z, p_{h\perp}) \frac{\Delta q(x)}{q(x)}, \tag{5.7}$$

where,

$$P_{q\ t}^{h}(x, z, p_{h\perp}) = \frac{e_q^2 \ q(x) \ D_{q\ t}^{h}(z, p_{h\perp})}{\sum_{q'} \ e_{q'}^2 \ q'(x) \ D_{q'\ t}^{h}(z, p_{h\perp})} \tag{5.8}$$

and t represents the target type. When the target is the deuteron and the struck nucleon is the neutron, the struck quark is isospin rotated ($u \rightleftharpoons d$ and $\bar{u} \rightleftharpoons \bar{d}$). This is done as we are interested in extracting the PDFs of the proton and not those of the proton and neutron combined.

The purity contains all the information about fragmentation and will allow us to disentangle the sum over quark flavors contained in the measured asymmetry. Fragmentation functions, and hence the purities, are as we've discussed incalculable from first principles and are for most quark flavors largely unknown in DIS in the HERMES kinematic regime. The purities then will be estimated using a standard HERMES Monte Carlo package, `gmc_disNG`, which contains the `JETSET` model of the fragmentation process.

5.3.1 JETSET and the Lund-String Model

The Lund-String model, which motivates the fragmentation process within JETSET, describes color-confinement and fragmentation in terms of *color-strings* – rubber band or spring-like structures which create a linear potential between like-colored quark-antiquark (or quark-diquark) pairs which is an increasing function of distance. By selecting points at which to break these strings (creating quark-antiquark, or diquark-antidiquark pairs), modeling gluons as kinks in the string, and conserving momentum and energy, an impressive amount of fragmentation phenomenology can be reproduced by adjusting its free parameters.

Given an initial set of partons to fragment (in the DIS case, a struck-quark–diquark-remnant configuration), JETSET follows the following iterative procedure [41]:

1. JETSET selects the flavor of the pair of quarks (or diquarks) to be produced at the next string break. As the likelihood of producing different flavors is as of yet incalculable but presumably quark-mass related, the relative likelihoods of producing the different light quark flavors u:d:s used by JETSET are 1:1:0.3. The strange quark can be suppressed further through a JETSET input parameter. The ratios of quark-antiquark to diquark-antidiquark pair production for the two lightest quarks and for strange quarks are also tunable.

2. The (mutually compensating) transverse momentum of the new pair to be produced (relative to the color-string) must be determined. This is selected from a Gaussian distribution of tunable width. Further parameters are available for fine-tuning the shape of the tails of this distribution.

3. At this point the quark composition of the new hadron is established. JETSET uses various tunable probabilities to determine quantum numbers, i.e. L, S, J, and I of the new hadron.

4. The simulation then decides where to break the string – i.e. how much energy to give to a new hadron and how much to give to the remainder-system. There is at this point only one degree of freedom remaining for the new hadron (m, p_x, and p_y are already specified). The selection of the final momentum component (and string break location) is accomplished using the Lund-Symmetric splitting function,

$$f(z) = \frac{(1-z)^a}{z}\, e^{-bm_\perp^2/z}. \tag{5.9}$$

   Here a and b are tunable string tension parameters, $m_\perp$ is the *transverse mass* ($\equiv m^2 + p_x^2 + p_y^2$), and z is the fraction of the available $E + p_z$, where p_z is the momentum along the string axis. The functional form of $f(z)$ is essentially unique as we require that fragmentation to be independent of the side where string breaking begins [42].

This process repeats on the remainder-system until the tunable lower threshold energy is reached and two hadrons are produced (rather than a hadron and another remainder system).

While this overview is somewhat simplified, it describes the core functionality of the fragmentation Monte Carlo and provides some idea of how the simulation is constructed and tuned to reproduce observed distributions.

5.3.2 Tuning JETSET

While the values of a few JETSET input parameters can be selected by hand on the basis of physical arguments, many (~ 10) must be tuned iteratively by comparing unpolarized Monte Carlo multiplicities to those from HERMES data. This tunes the model to HERMES kinematics, which are somewhat different than the high-energy regime for which the JETSET default settings are adjusted.

In order to do this, we construct a χ^2 function to gauge the agreement between MC multiplicities (which are a function of our tune) and the data multiplicities:

$$\chi^2_{\text{tune}}\left(\mathbb{P}_n\right) = \sum_{h:\{\text{hadrons}\}} \sum_{i:\{\text{bins}\}} \left(\frac{M^h_{\text{MC}}(\mathbb{P}_n, i) - M^h_{\text{Data}}(i)}{\delta M^h_{\text{Data}}(i)} \right)^2, \tag{5.10}$$

where $\mathbb{P}_n$ is the vector of n JETSET parameter values and M is a multiplicity ($\equiv \frac{N_h}{N_{\text{DIS}}}$). Enough Monte Carlo events are produced such that the denominator of χ^2_{tune} is dominated by the data uncertainty.

For this analysis, we have chosen to compare z and $p_{h\perp}$ dependent multiplicities for pions, kaons, and protons of both charges. The z multiplicities have 18 evenly spaced bins with $0.1 > z > 1.0$. The $p_{h\perp}$ multiplicities have 20 bins with $0 < p_{h\perp} < 1$. This gives a total of 228 bins, though the actual number of degrees of freedom in the χ^2_{tune} comparison was reduced to 224 by four empty high-z data bins. Figures 5.3 and 5.4 present the data multiplicities used to tune the Monte Carlo as well as multiplicities produced using the Monte Carlo using the tune resulting from this work, "Lund-Scan", and an earlier standard HERMES tune, 2003a.

In principle, the task of tuning the fragmentation model is as simple as minimizing the value of this chi-squared function. We are presented, however, with two significant technical challenges:

1. A ten dimensional parameter space is *vast* and the multiplicity-comparison χ^2 will most certainly have *strong correlations* between its tuning parameters. Because of this, the tuning must take place simultaneously in all of the parameters rather than in one at a time.

2. Each parameter-space point requires a Monte Carlo run to be produced with sufficient statistical precision to produce a reliable comparison to the available data. This number is approximately 5×10^6 events which, using available computer hardware, requires $\sim$1 hour of

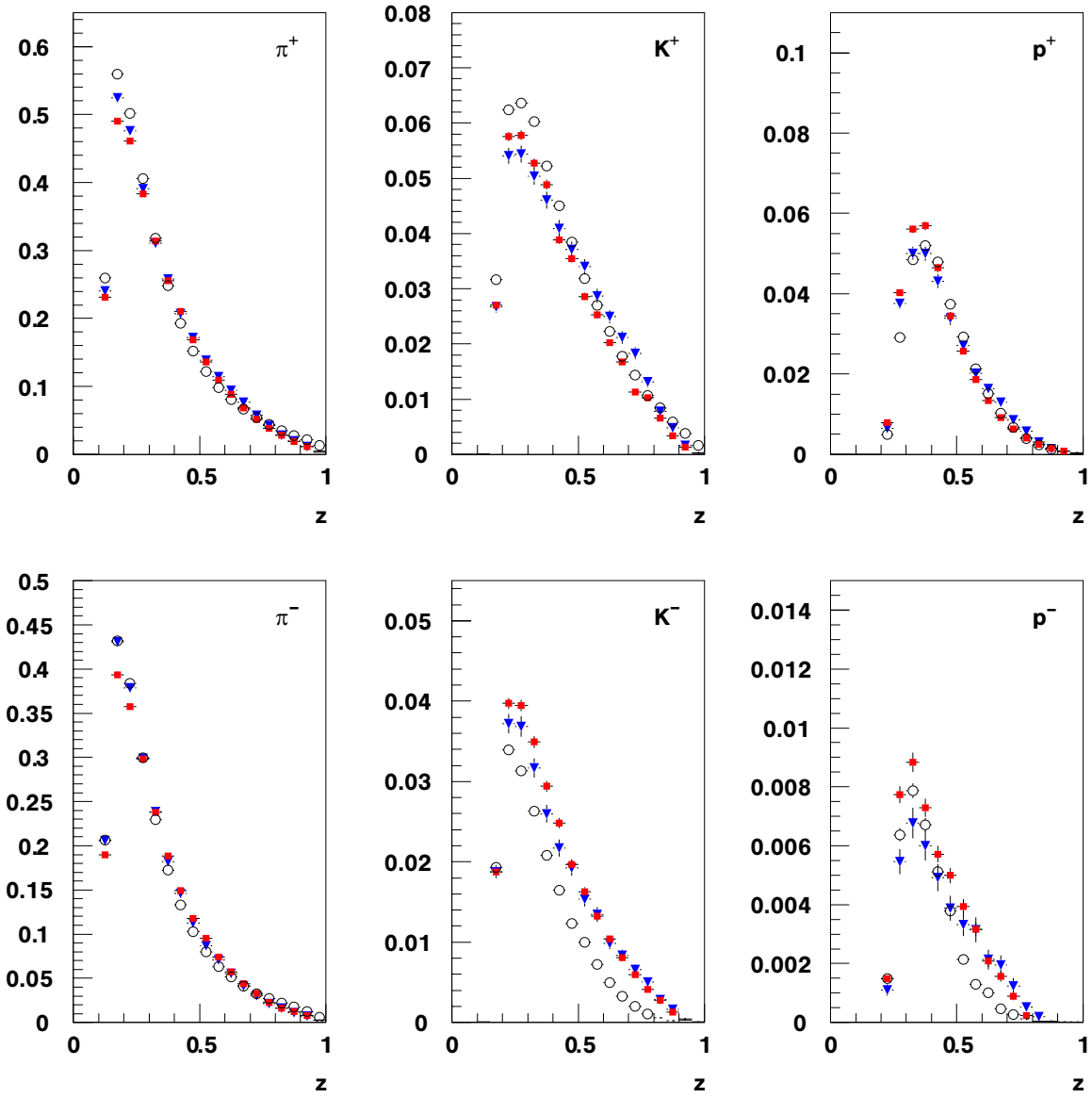

Figure 5.3: Hadron multiplicities, $N_h(z)/N_{\rm DIS}(z)$. Data (open points), Monte Carlo 2003a tune (blue triangles), and Monte Carlo "Lund-Scan" tune (red squares) are compared.

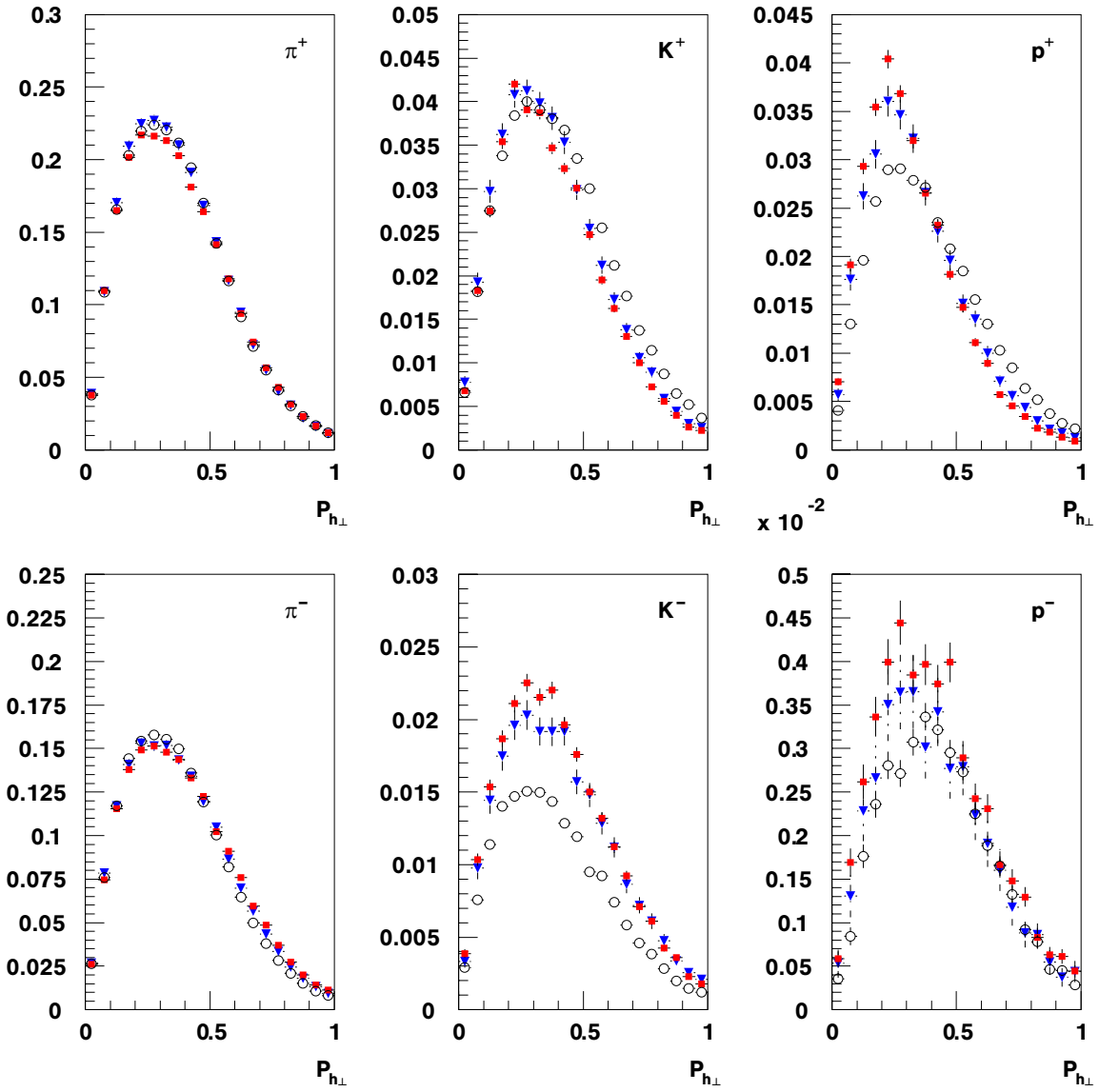

Figure 5.4: Hadron multiplicities, $N_h(p_{h\perp})/N_{\rm DIS}(p_{h\perp})$. Data (open points), Monte Carlo 2003a tune (blue triangles), and Monte Carlo "Lund-Scan" tune (red squares) are compared.

CPU time. Most standard minimization software packages, `MINUIT`[43] for example, are not designed for parallel computing purposes. Furthermore, while computing resources have become significantly more powerful since earlier tuning attempts, the statistical noise inherent in each evaluation of the χ^2_{tune} can easily confuse standard minimization algorithms.

Prior tuning efforts gradually transitioned from hand tuning individual parameters and educated guesses for parameter values to more sophisticated multidimensional chi-squared minimization as CPU power and analysis manpower became available. In fact, this effort continued in parallel with this analysis producing a series of very good tunes – `2003a`, `2004a`, `2004b`, and `2004c` – involving innovative tuning strategies such as genetic algorithms. While agreement with data is arguably comparable to the result of the "Lund-Scan" technique presented here, as we will see in the following sections, "Lund-Scan" provides us with a robust method for assessing the systematic uncertainty of the fragmentation tune and a means of excluding the possibility of parameter correlations producing regions of degenerate tune-minima.

Unlike more conventional minimization strategies, which essentially follow the negative gradient of a function – like a skier on a mountain – to find the quickest way to the minimum, the "Lund Scan" strategy assumes that χ^2_{tune} is smooth in some vicinity around the minimum. By sampling within a range in some combination of these variables, a quadratic function is fit to the region. By repeating this process, better scan ranges can be found and a region of quadratic smoothness can ultimately be identified. The cross-terms of the fit function contain the lowest order correlations of the parameters. This has two major advantages over prior techniques: statistical noise which confuses other minimization algorithms is naturally smoothed, and many samples at once can be computed in parallel on a computing cluster.

As we will now be introducing *a second* χ^2 – for the polynomial fit to a set of χ^2_{tune} points, it seems worthwhile to keep the notation clear. χ^2_{tune} will continue to be used as it has and the fit chi-squared will consistently be referred to as χ^2_{fit}.

What we will call *a scan* is an iterative process that begins with a sample of χ^2_{tune} values for two parameters distributed in a rectangular region and whose ultimate goal is to have a good quadratic fit to all ($\sim$10) parameters simultaneously. A scan is then comprised of the following steps:

1. Generate a set of well-distributed points $\mathbb{P}_n$ in Lund parameter space within a (hyper-)ellipsoid of constant χ^2_{tune}. The number of points required is a small multiple of the number of fit coefficients. Some oversampling reduces the impact of statistical noise. Properly selecting the size of the ellipsoid is essential to getting a good fit to the chi-squared surface. If the previous iteration yielded reasonable fit agreement, each new sampling point must also be given values for the new (as of yet unfit) parameter sampled in a reasonable range determined from a single parameter scan.

2. Compute a Monte Carlo sample of 5×10^6 events for each point. This can be performed in parallel with many CPUs. In practice, as many as 16 simultaneous Monte Carlo jobs were performed.

3. Compute χ^2_{tune} for each parameter-space point by comparing the Monte Carlo to data multiplicities.

4. Fit the $\chi^2_{\text{tune}}(\mathbb{P}_n)$ values with a quadratic polynomial of n variables. There are three possible outcomes which determine the next step:

   $\chi^2_{\textbf{fit}}$ **indicates good agreement:** Use the fit to generate the next set of samples and add an additional parameter.

   $\chi^2_{\textbf{fit}}$ **indicates bad agreement:** If the sampling pattern was too small, the fit will poorly reflect the location of the minimum (and yield a χ^2_{fit} which is too small, $\chi^2_{\text{fit}} \approx 0$). If the sampling pattern was too large, the fit will be poor as the surface becomes higher-order (the fit chi-squared will be large, $\chi^2_{\text{fit}} \gg 1/\texttt{DoF}$). In either case, the same parameters must be resampled and refit. If possible, use this fit to improve minimum location and sampling range.

   Fit polynomial has negative quadratic coefficients: This is the worst case. Regardless of the numeric fit agreement, if this occurs, the function can't be minimized and is clearly a unacceptable representation of the true χ^2_{tune} function. Reselect sampling range– perhaps remove the last parameter added and try adding them in a different order.

A challenge with this procedure is that as each parameter is added, the entire process becomes more fragile. While taking more time to generate a suitable number of sampling points, which makes it difficult to try multiple scan range variants quickly, it becomes easier to select sampling points that push into the higher-order region of the χ^2_{tune} function – particularly for newly added parameters where a nice parameterization of the ellipsoid of constant χ^2_{tune} is not yet available. In fact, with a rapidly increasing number of quadratic cross-terms (as n increases), it becomes increasingly likely for one of the weaker ones to pick up a negative sign out of simple statistical fluctuation. For these reasons, the procedure becomes fairly labor intensive and requires a lot of trial and error and some intuition for the "black art" of scan range selection.

The values for the "Lund Scan" tune are given in Table 5.1. The multiplicities at the final tune location can be seen in Figures 5.3 and 5.4.

The final quadratic fit to the χ^2_{tune} surface can be seen in Figure 5.5 in 36 two-dimensional cross sections. The agreement is good ($\chi^2_{\text{fit}}/195\text{DoF} = 0.82$) between the 55 parameter quadratic fit and the 250 parameter space/χ^2 points. The fit minimum, which is the best tune location, had

Parameter	$\Delta q(x)$ paper	2004c	"Lund-scan"	Parameter Description
PARJ1	0.02	0.029	0.02	Diquark suppression
PARJ2	0.20	0.283	0.25	Strange quark suppression
PARJ11	0.5*	0.5*	0.51	Vector meson suppression (light mesons)
PARJ12	0.6*	0.6*	0.57	Vector meson suppression (strange mesons)
PARJ21	0.37	0.38	0.42	Width of Gaussian $p_{h\perp}$ distribution [GeV]
PARJ33	0.8	0.8	0.47	String breaking mass cutoff
PARJ41	1.74	1.94	0.68	Lund-String "a" parameter
PARJ42	0.23	0.544	0.35	Lund-String "b" parameter
PARJ45	0.5*	1.05	0.74	"a" adjustment for diquark
PARL3	0.44	0.44	(0.44)	Gaussian width of intrinsic k_T [GeV]
PARJ23	0.03	0.01	(0.01)	Fraction of $p_{h\perp}$ distribution to have additional non-Gaussian tails
PARJ24	2.50	2.0	(2.0)	Strength of non-Gaussian $p_{h\perp}$ tails

Table 5.1: Various recent JETSET tunes. "Lund-scan" is the new tune described in this work. The values in parenthesis were left untuned by the "Lund-scan" method and taken from the 2004c tune. The $\Delta q(x)$ paper tune is sometimes colloquially referred to as the *Felix* tune [44] with the exception of the value above for PARL3 [45] (*JETSET default)

a value of 12.2 (per 224 degrees of freedom). A final $\chi^2_{\text{tune}}(\mathbb{P}_{\text{"Lund-Scan"}})/224$Do F gave a value of 12.8, whose consistency with the polynomial minimum further supports for the goodness-of-fit of the quadratic polynomial to the χ^2_{tune} surface.

If our model *could* reproduce nature perfectly, one would expect $\chi^2 \approx$ DoF (the number of degrees of freedom). To some degree the value our best tune gives depends on what we choose to include in the χ^2 comparison of Equation 5.10. Ultimately, however, JETSET is only a model and will never exactly reproduce the multiplicities we observe. We will make an attempt to take this into account when estimating our model-dependence in Section 5.3.3.

Purities

Ideally, we would both generate purity matrices and assess the tune-related systematic uncertainty on the purities using the "Lund-Scan" tune. At the time of writing, however, the "Lund-Scan" tune lacked a cross-check and a completely satisfactory result for the final three parameters of Table 5.1. Because of this, it was decided to produce the purities for the $\Delta q(x)$ extraction using the 2004c tune while estimating the model-dependent uncertainty using the "Lund-Scan" method.

The results for the one-dimensional x-dependent purities for the proton and deuteron are given in Figure 5.6.

Three-Dimensional Purities

The primary motivating factor of attempting this reanalysis in three kinematic dimensions – dividing the semi-inclusive asymmetries into x, z, and $p_{h\perp}$ bins – was to better isolate different

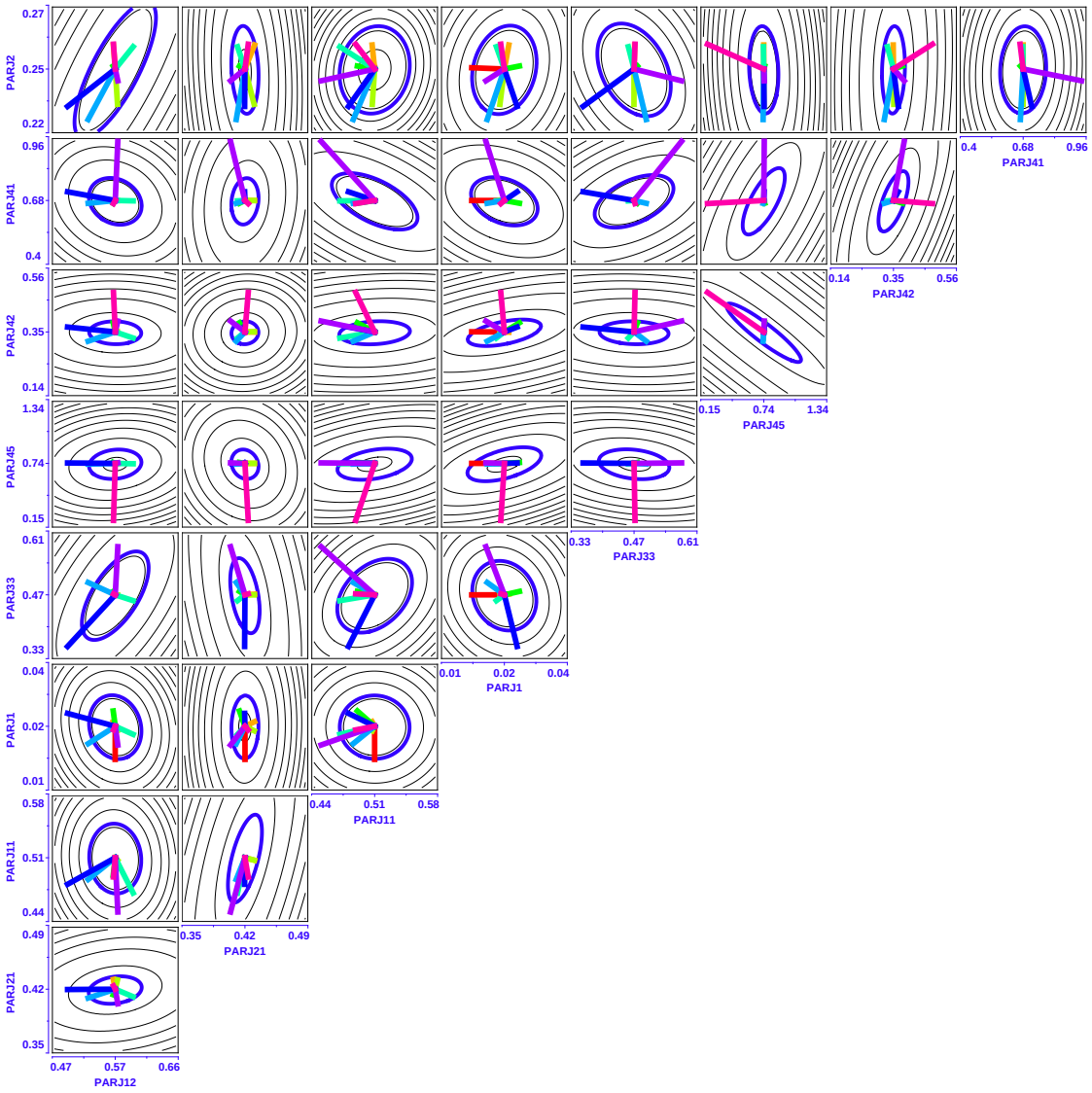

Figure 5.5: Contour plots of two-dimensional cross sections of the quadratic fit function in nine JETSET parameters to the $\chi^2_{\rm tune}$ surface produced by comparing Monte Carlo to data multiplicities ($\chi^2_{\rm fit}/195{\rm DoF} = 0.82$). Most panels contain contours with elliptical axes which are to some degree diagonal. This indicates correlation between the JETSET parameters. The blue band represents 2D slices of the hyper-ellipsoid that has a 68% likelihood of containing the true best tune. This band was expanded to compensate for the fact that the χ^2 minimum was still considerably greater than the number of degrees of freedom ($\chi^2_{\rm tune}/224{\rm DoF} = 12.2$). The colored lines represent the nine uncorrelated parameter axes produced by diagonalizing the Hessian matrix and terminate where they intersect the 68% hyper-ellipsoid.

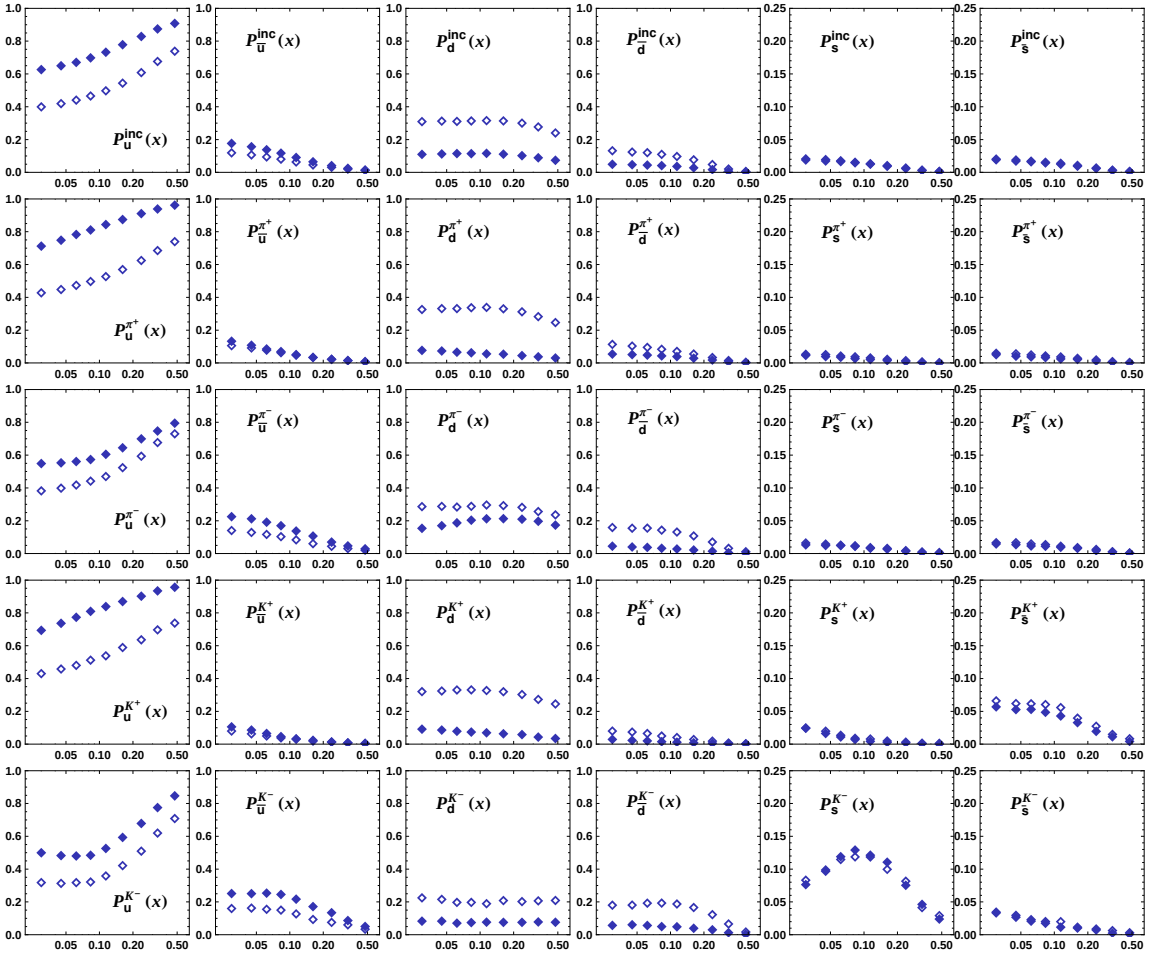

Figure 5.6: Purities in x-bins for the proton target (solid points) and deuteron target (open points) for each quark and asymmetry type. Note the change of scale for the strange quarks (last two columns).

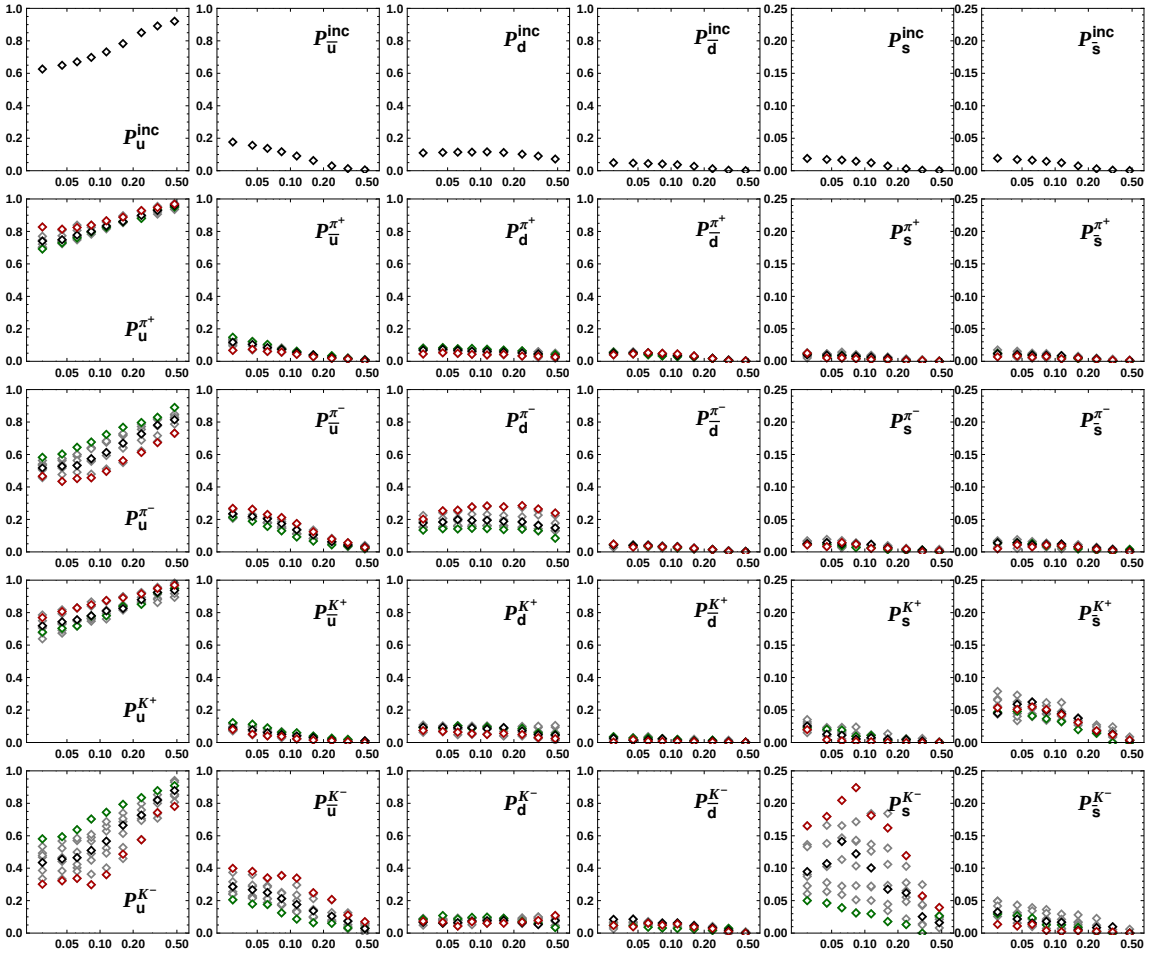

Figure 5.7: Purities in x-bins for the proton target. At each x position there are nine points, representing each of the nine z-$p_{h\perp}$ bin combinations. The "leading", high-z–low-$p_{h\perp}$ is plotted in red, the "remnant", low-z–high-$p_{h\perp}$, is plotted in green, and the "central", middle bin of each semi-inclusive variable, is plotted in black. All other combinations are shown in gray. Note the change of scale for the strange quarks (last two columns).

regions of fragmentation and get more benefit out of the statistics available. Conceptually, one can easily imagine that a high-z, low-$p_{h\perp}$ hadron is more likely to be associated with the struck quark where a low-z, high-$p_{h\perp}$ hadron is more likely to related to the target remnant. To make this idea more concrete, the three-dimensional purities are presented two ways. Figure 5.7 presents the nine z-$p_{h\perp}$ with the high-z, low-$p_{h\perp}$ or *leading* bin and the low-z, high-$p_{h\perp}$, or *remnant* bin in color. The significant difference in purities between these two bins support this picture. Figure 5.8 presents only five of the nine x-bins in order to make space to plot all nine of the z-$p_{h\perp}$ bins in each x position. Once can see that the purities depend on each of these semi-inclusive variables individually, but most dramatically on both simultaneously.

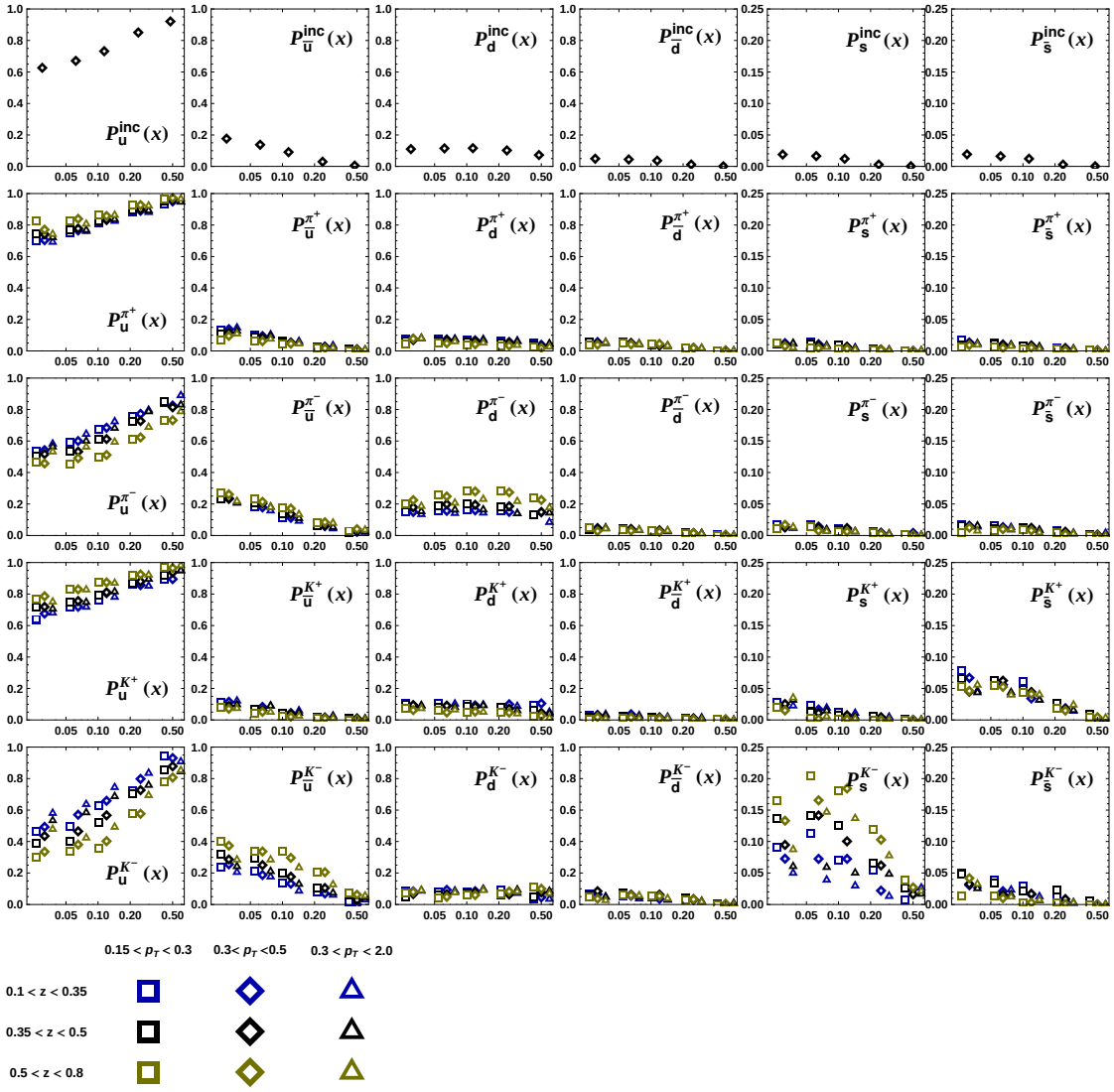

Figure 5.8: Purities in x-bins for the proton target. Only five of the nine x-bins are shown in order to make space for points representing all nine semi-inclusive bins. One can see that the purities depend on z (variations in point color) and $p_{h\perp}$ (variations in point shape) in addition to inclusive x. Note the change of scale for the strange quarks (last two columns).

5.3.3 Estimation of the Tune Uncertainty

While the "Lund Scan" procedure was generally very successful at finding a good JETSET tune, its primary goal was to provide a robust framework for estimating the tune-related uncertainty, and thereby the model-dependent systematic uncertainty of the purities and the purity method.

In the published $\Delta q(x)$ result [16], a purity-related systematic uncertainty was generated by comparing the central "Felix" tune with the JETSET default tune and a second high-energy tune, both of which were known to poorly reproduce multiplicities in the HERMES kinematic regime. The *hope*, for lack of a better procedure, was that this would be a conservative estimate. In addition to potentially greatly overestimating the uncertainty (the tune uncertainty is the largest source of systematic uncertainty in many bins), there was one potentially dangerous scenario that could not be excluded. *If* there was ambiguity in the best tune – i.e. a trough through which the value of χ^2_{tune} didn't change but which affected the value of the extracted $\Delta q(x)$, the purity method would have failed completely. For lack of the ability to exhaustively map the parameter correlations around the minimum, there was no way to know for sure.

The objective of the "Lund-Scan" then is twofold:

1. Determine rigorously the uncertainty on $\Delta q(x)$ due to the uncertainty in the tune and model imperfection.

2. Exclude the possibility of the *doomsday scenario*, a parameter space contour that is a degenerate χ^2_{tune} minimum, but changes the value of the extracted $\Delta q(x)$.

In order to accomplish this, the critical concept is that the χ^2 surface gives you more information than a single minimum indicating a best fit. It allows you to determine a confidence contour that encloses a specific likelihood of containing the true best tune to the underlying distribution. In a one-dimensional case, one can determine the error bar on a parameter by *climbing the χ^2 function the number of sigma that it is desired for the error bar to represent.* The ends of a standard 68% error bar should fall where χ^2 function is *one* unit above its minimum.

In a more conventional error propagation situation, when one has an *analytic* functional form and a set of parameters with 1-σ uncertainties (and covariances) as described above, one can easily utilize the standard error propagation methods to find the uncertainty on the function. In our case, rather than an analytic function, our Monte Carlo multiplicities are a *black-box* function of the tuning parameters – that is, it is impossible to take the required derivatives of the multiplicities with respect to the input parameters.

In order to address this, a different approach is taken. Rather than climbing this χ^2_{tune} one unit above the minimum for each parameter and establishing a set of individual 68% error bars and covariances for the individual parameters, we will select a height, K_{up}, above the tune minimum *that represents a 68% likelihood that all true best-fit parameters simultaneously occupy the region.*

n	1	2	3	4	5	6	7	8	9	10	11	12
$K_{\rm up}$	1.00	2.30	3.53	4.72	5.89	7.04	8.18	9.30	10.4	11.5	12.6	13.7

Table 5.2: The height, $K_{\rm up}$, above $\chi^2_{\rm min}$ that defines a parameter-space region with a 68% likelihood of *simultaniously* containing all of the unknown true parameter positions for n parameters.

Because a change in χ^2 *means* the number of σ (notice that the χ^2 function *is* the exponent in the Normal distribution), $K_{\rm up}$ is the number of σ distance one must integrate the Normal distribution from the mean to yield 0.68. The trivial case (and the one that defines the standard deviation to be 0.68) is the one parameter case. If $n = 1$, we require the integral from the mean to equal 0.68. The normal distribution with a mean of zero and a width of σ is written as follows:

$$p(x) = \frac{1}{\sigma\sqrt{2\pi}}\, e^{-\frac{x^2}{2\sigma^2}}\, dx, \tag{5.11}$$

We would now like to know how many sigma around the mean must we integrate to represent the canonical 68% of the probability distribution. To do this, we make the variable substitution $u = x/\sigma$, which means u is *a number of* σ and integrate from $-K_{\rm up}$ to $K_{\rm up}$.

$$0.6827 = \frac{1}{\sqrt{2\pi}} \int_{-K_{\rm up}}^{K_{\rm up}} e^{-\frac{1}{2}u^2}\, du \tag{5.12}$$

This equation can be solved yielding a value of 1 for $K_{\rm up}$, which is of course true by constuction. The more interesting case, however, is if we would like to determine the number of sigma required for the joint probability of n parameters to equal 0.68. In analogy to Equation 5.12, we write

$$0.6827 = \left(\frac{1}{\sqrt{2\pi}}\right)^n \int du_1 \ldots du_n \prod_{i=1}^{n} e^{-\frac{1}{2}u_i^2}, \tag{5.13}$$

Rather than a integrating over a rectangular region, however, we would like to integrate n-dimensional spherical shells out to a single value of radius $K_{\rm up}$. We make the appropriate change of variables to a spherical system:

$$0.6827 = \frac{1}{2\ \Gamma(n/2)} \int_{0}^{K_{\rm up}} e^{-u/2}\ (u/2)^{\frac{n}{2}-1}\, du, \tag{5.14}$$

which is a combination of an integral of the surface area of n-dimensional spherical shells (the angular part of the integral) and the radial integration over the Normal distribution. The formula has been solved numerically for several values of n which are provided in Table 5.2.

Additionally, we use a second factor to compensate for the limitations of `JETSET` – that it fails to perfectly reproduce the data multiplicities exactly when carefully tuned

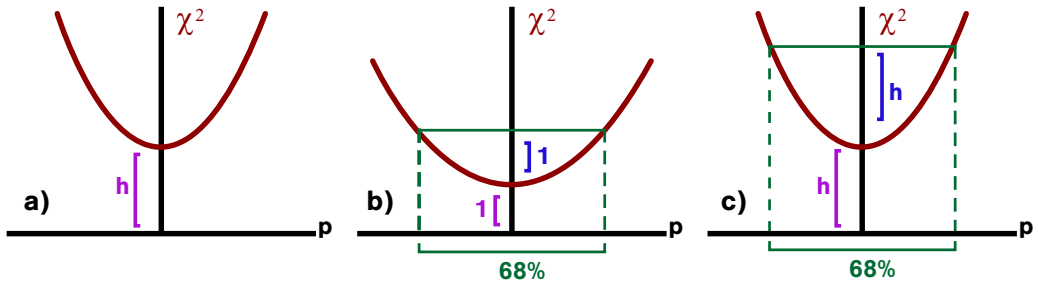

Figure 5.9: A set of schematic diagrams describing the artificial error inflation process for addressing unavoidable model-incompatibility. a) shows a χ^2 curve that depends upon one parameter p. $h = \chi^2_{\rm min}$ which is somewhat greater than 1. b) depicts the curve plotted again with the error bars in the χ^2 function inflated by a factor of $h^{1/2}$. This brings $\chi^2_{\rm min}$ back to one – restoring compatibility between the model and the data, i.e. restoring the interpretation that $\chi^2_{\rm min}+1$ provides the 68% inteval. c) demonstrates that by climbing the χ^2 function a height h above the original panel a) minimum, an error interval equivalent to panel b) is produced.

($\chi^2_{\text{“Lund-Scan”}}$/224DoF = 12.2). The strategy we will use is that used by the Particle Data Group [5] to reconcile inconsistent datasets. The procedure is essentially to artificially inflate the error bars of the data until they accommodate the discrepancy adequately. The steps described here are depicted schematically in 5.9. It can be easily shown that in order to reduce the minimum of $\chi^2_{\rm tune}$ to one, the data uncertainties of $\chi^2_{\rm tune}$ (Equation 5.10) should be inflated by a factor of $\sqrt{\chi^2_{\text{tune-min}}}$. Doing so would leave us with a situation analogous to panel b) of Figure 5.9. A simpler alternative, however, which is also simple to show, is to *increase the height above the existing minimum by a factor of* $\chi^2_{tune\text{-}min}$. This creates an uncertainty interval equivalent to inflating the errors themselves, accommodating the incompatibility of the model and the data.

Finally, then, we are able to establish a height above $\chi^2_{\text{tune-min}}$ that represents the joint probability of containing all of the ideal parameter values and accommodates model imperfection.

$$\begin{aligned} \Delta\chi^2 &= k_{\rm up}(n) \times \chi^2_{\text{tune-min}} \\ &\quad \textit{for our nine-parameter result} \\ &= 10.4 \times 12.2 \\ &= 127. \end{aligned} \tag{5.15}$$

This error band is shown as a blue ellipse overlaid in the two-dimensional cross section contour plots of Figure 5.5.

In order to characterize the 68% uncertainty contour in a way that we can propagate to further calculations which depend upon the purities, we follow the work of the CTEQ group and their decision to describe their most recent unpolarized PDF parameterizations, CTEQ6, using a set of uncorrelated *Hessian* vectors [40]. This procedure holds that by diagonalizing the matrix of $2^{\rm nd}$ derivatives of the χ^2 function, one gets a set of vectors which are an uncorrelated, orthogonal

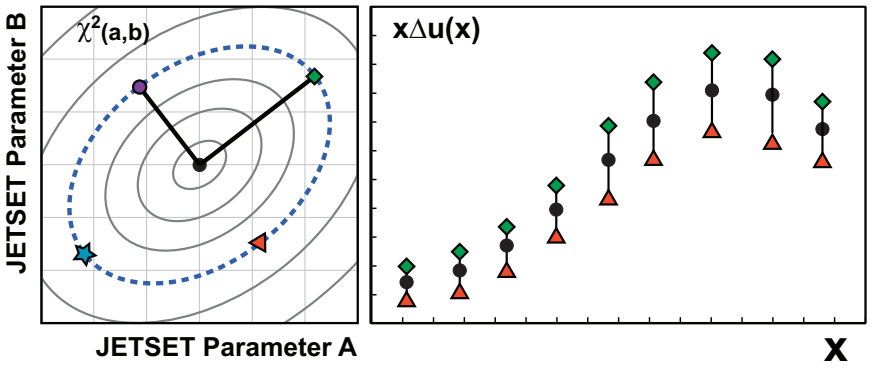

Figure 5.10: A schematic depiction of the Hessian error characterization procedure. (Left) A χ^2 contour is mapped out as a function of two parameters. One can see that because the 68% error ellipse (blue dashed) is oriented diagonally, the parameters are correlated. By diagonalizing the matrix of 2^{nd} derivatives of χ^2, the *Hessian* matrix, one computes the uncorrelated parameter directions. The intersections of these vectors with the contour (the four shapes) provide parameter sets that completely characterize the 68% contour of the parameter space. (Right) The model-related systematic uncertainty on a quantity ($\Delta q(x)$ in our case) computed from that model (JETSET in our case) can be approximated by computing that quantity at each Hessian-vector/contour intersection and taking the maximum deviation from the quantity at the best tune.

linear combination of the input parameters. They are also the axis vectors of the n-dimensional ellipsoid that represents the 68% contour. This procedure is depicted in the left panel of Figure 5.10.

For our calculation, the colored lines in Figure 5.5 are projections of the uncorrelated, Hessian vectors which originate at the fit minimum and terminate at the 68% contour. As each Hessian direction provides two intersections with the ellipsoid, we have 18 (2×9) tunes which completely characterize the model uncertainty. To demonstrate that these vectors do indeed represent the uncorrelated parameter basis, which is not entirely obvious from their projections, the fit, the 68% contour, and the Hessian vectors have been replotted in the Hessian basis in Figure 5.11.

Error Propagation to the $\Delta q(x)$ Result

These $2n$ Hessian error tunes can be used to estimate the uncertainty contributed to the $\Delta q(x)$ result. $\Delta q(x)$ is extracted (via the procedure that will be described in the following chapter) using purities generated with the JETSET best tune, $\mathbb{P}_{\text{“Lund-Scan”}}$, and with purities generated with each of the error tunes as depicted in the right panel of Figure 5.10. The maximum deviation from the best tune is the error estimate in the bin. The 18 $\Delta q(x)$ sets can be seen in Figure 5.12. Their deviations from the best tune are compared to purity-related and total systematic uncertainty from the prior publication [16] in Figure 5.13.

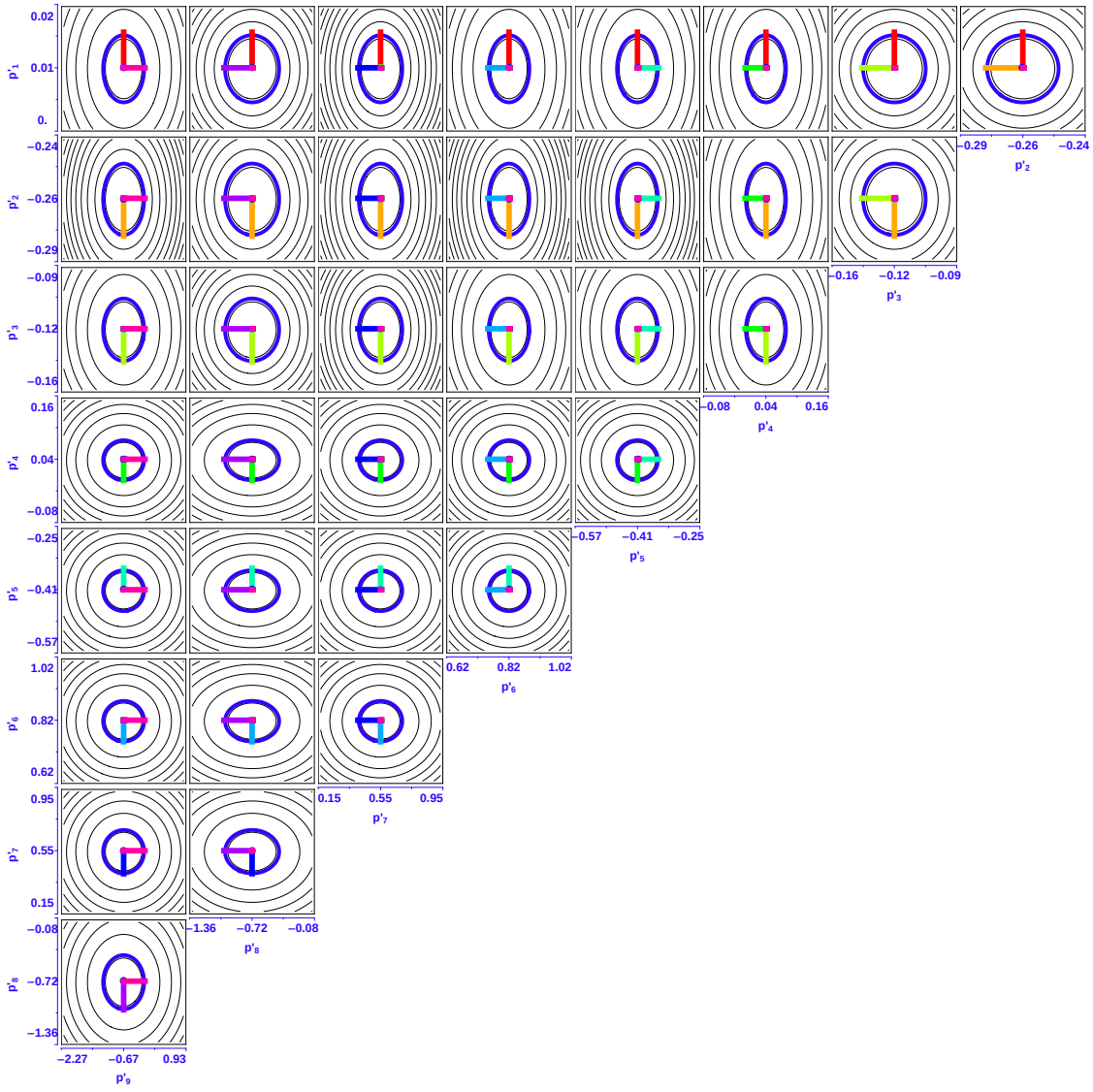

Figure 5.11: Contour plots of two-dimensional cross sections of the quadratic fit in nine JETSET parameters to the $\chi^2_{\rm tune}$ surface produced by comparing Monte Carlo to data multiplicities. Rather than plotting in terms of the JETSET parameters as in Figure 5.5, a change of variables has been made to the uncorrelated Hessian basis. All of the elliptical axes match the basis-axis directions. The blue ellipses represent projections of the 68% ellipsoid, and the colored lines represent the uncorrelated parameter directions whose intersections are used to generate the 18 error-characterizing tunes.

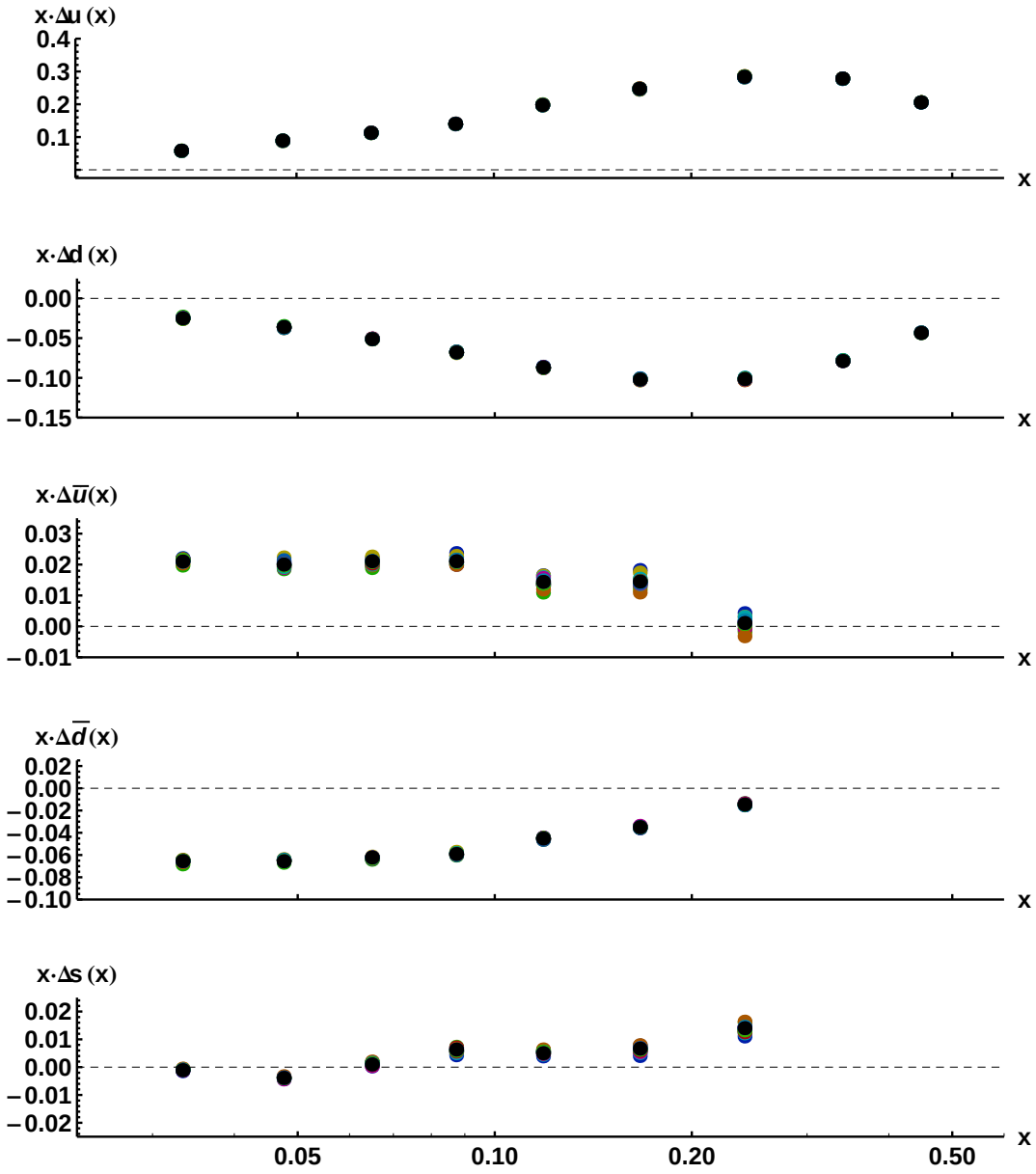

Figure 5.12: $\Delta q(x)$ for five quark flavors extracted using the best tune (black) purities and 18 Hessian purities lying on the 68% uncertainty contour. The variation of the valence quark helicity densities, $x\dot{\Delta}u(x)$ and $x\dot{\Delta}d(x)$ is so small relative to the function magnitude that it is nearly invisible.

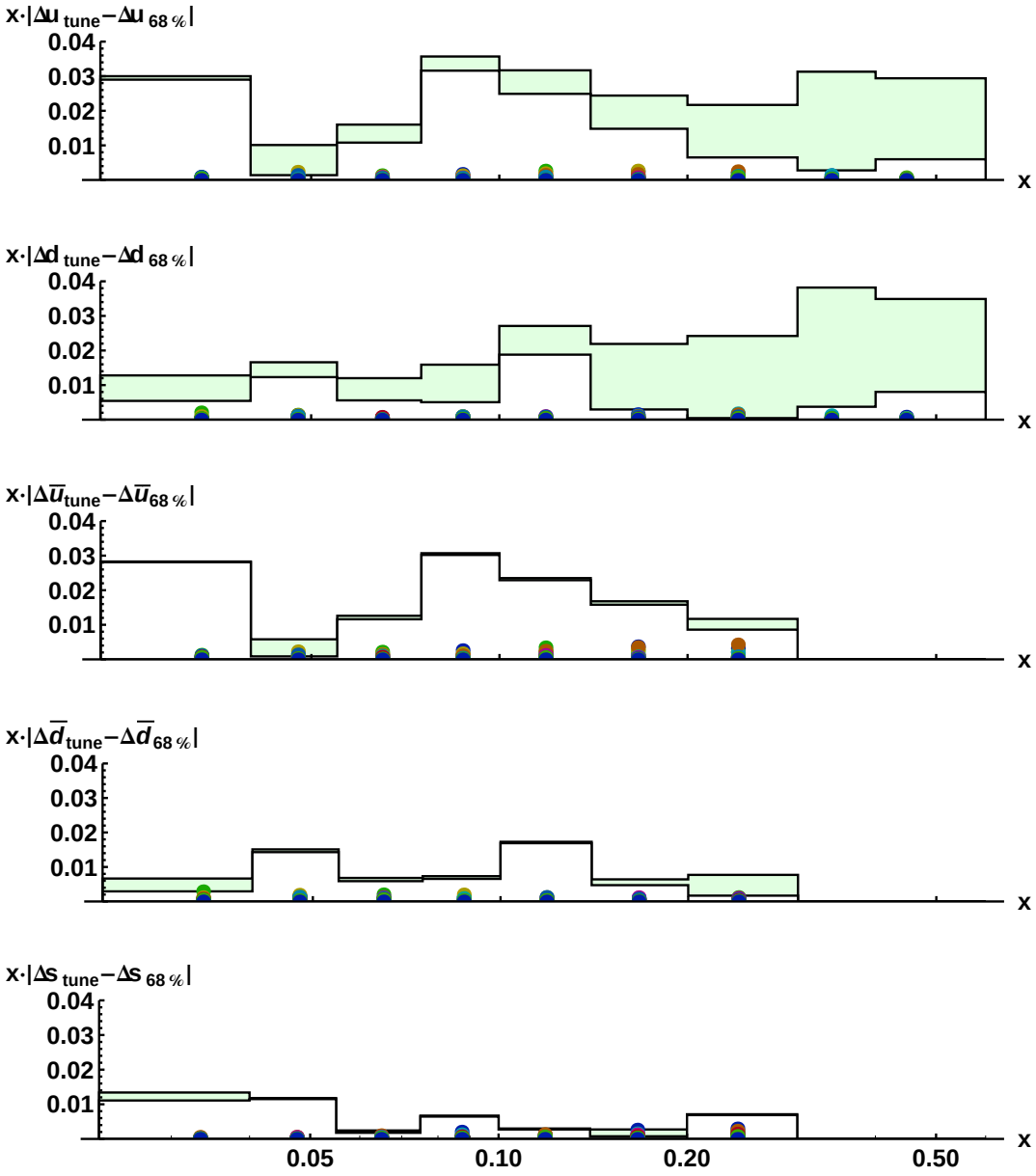

Figure 5.13: The magnitude of the difference between $\Delta q(x)$ extracted using purities generated with the best tune and those extractied using purities generated at the 18 Hessian 68% uncertainty tunes. The maximum deviation (highest point) is taken to be the new fragmentation model systematic uncertainty for $\Delta q(x)$. The white and green bands represent the tune-related and total systematic error bands from the prior 5-flavor extraction [16]. In most bins the previous estimate can be reduced significantly.

Chapter 6

The Quark Helicity Distributions

6.1 The Quark Polarizations

As established in chapter 1, the semi-inclusive asymmetry can be written as a combination of purity matrices, $\mathcal{P}$, and quark polarizations, $\Delta q(x)/q(x)$ as follows:

$$A_1^h(x) = \sum_q \mathcal{P}_q^h(x) \frac{\Delta q(x)}{q(x)}. \tag{6.1}$$

Using the measured asymmetries and the Monte Carlo modeled purity matrices, values for the quark polarizations can be extracted. To do this, the preceding formula is rewritten for a single kinematic bin x_i from a particular observed hadron h,

$$A_{x_i}^h = \sum_q \mathcal{P}_{q\ x_i}^h Q_{q\ x_i}, \tag{6.2}$$

where Q_{qx_i} is the unknown value of $\Delta q(x)/q(x)$ for quark q and kinematic bin x_i. In the simplest case, with the kinematic binning of the asymmetries and purities only in x, we have 72 data bins (eight asymmetries $\times$ nine x-bins) and at most 36 unknown quark polarization values (six quarks $\times$ nine x-bins). Because of this, the over-constrained quark polarizations are extracted using a best-fit technique. From the single-bin expression for A_1^h (eq. 6.2), we construct the following least-squares expression for χ^2,

$$\chi^2 = \sum_{t,h,x_i,x_j} \left[\left(\sum_q \mathcal{P}_{t,q,x_i}^h Q_{q,x_i} - A_{t,h,x_i} \right) \nu_{t,h,x_i,x_j}^{-1} \left(\sum_q \mathcal{P}_{t,q,x_j}^h Q_{q,x_j} - A_{t,h,x_j} \right) \right], \tag{6.3}$$

which is a function of the unknown quark polarizations $Q_{q,x}$. This function can then be minimized numerically or solved algebraically (i.e. linear regression) to find the best-fit quark polarizations.

The index t runs over the two targets, h runs over the available asymmetries per target (both inclusive and semi-inclusive), and x_i and x_j run over kinematic bins. The leftmost sum represents four individual sums, one over each of these summation indices. ν is a covariance matrix containing both the statistical uncertainties and correlations between kinematic bins as described in Section 4.3.

6.1.1 Statistical Uncertainties

Generally speaking, the statistical covariance matrix of parameters k_1 through k_n determined with a least-squares fit can be computed as follows:

$$\sigma(k_i, k_j)^{-1} = \frac{1}{2}\begin{pmatrix} \frac{\partial^2\chi^2}{\partial k_1^2} & \cdots & \frac{\partial^2\chi^2}{\partial k_1 \partial k_n} \\ \vdots & \ddots & \\ \frac{\partial^2\chi^2}{\partial k_n \partial k_1} & & \frac{\partial^2\chi^2}{\partial k_n^2} \end{pmatrix} \text{[5]}. \tag{6.4}$$

The square of the uncertainty on a particular parameter k_i is given by $\sigma(k_i)^2 = \sigma(k_i, k_i)$. For our calculation then, the quark polarizations, Q_{q,x_i}, are the k_i upon which χ^2 depends.

6.1.2 Systematic Uncertainties

Systematic uncertainties enter this analysis at many different points and are important components of both the asymmetries and the purities. Unlike statistical errors which can be propagated in a fairly standard and rigorous way, systematic uncertainty propagation is often a tricky and approximate business. The procedure utilized in this case to propagate systematic uncertainties to the quark polarizations has two parts:

1. Evaluate the impact of each uncertainty on the quark polarization individually by extracting $\Delta q/q(x)$ using values of purities or asymmetries varied to the limits of the uncertainty. Compare those resulting quark polarization to the *central* extracted value – i.e. with no systematic uncertainty applied – to compute $\sigma_i(\Delta q/q(x))$, for each source, i.

2. Combine all of the differences in quadrature: $\sigma_{tot} = \sqrt{\Sigma_i \sigma_i^2(\Delta q/q(x))}$. While these uncertainties may not represent statistically distributed quantities, they are unlikely to be in any way correlated. While this doesn't represent a worst-case-scenario, this technique provides a *reasonable* estimate of the scale of systematic uncertainties involved.

Figure 6.1 depicts the various contributions of the different sources of systematic uncertainty to the final total systematic uncertainty of $\Delta q/q(x)$. The largest contribution comes from the uncertainty in the unpolarized PDFs inside the Monte Carlo model that generates the purities. This uncertainty was computed by modeling the purities analytically, using available

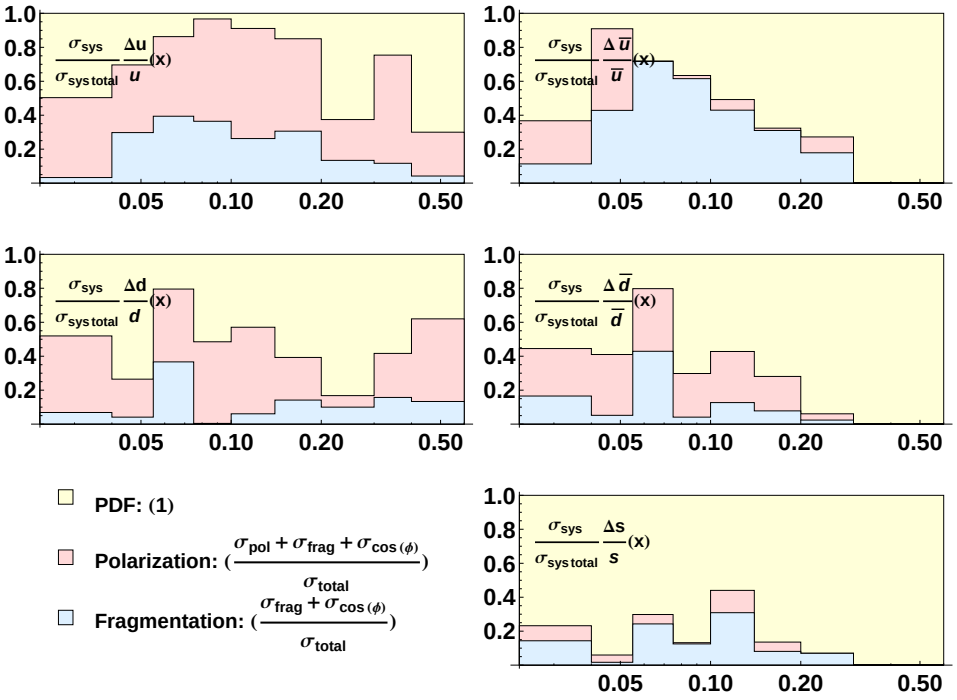

Figure 6.1: Fractional systematic uncertainty contributions to the extracted quark polarizations.

parameterizations of PDFs and fragmentation functions, 1) substituting alternate PDF sets and 2) varying these sets to their own uncertainties. The quark polarization was extracted with each combination. Due to the difficulty of evaluating this uncertainty and the lack of a reasonable fragmentation function parameterization at the time, this significant source of uncertainty was not included in the previously published result. The calculation of systematic uncertainties associated with polarization and the JETSET tune were described in Chapters 4 and 5, respectively. As described in Section 4.6, contributions from RICH unfolding and charge symmetric background are negligible.

6.1.3 $\Delta q/q(x)$ Result

Several variations of this extraction are possible. We will consider the main result, however, to be to be that produced using the x-binned inclusive and three-dimensionally binned semi-inclusive asymmetries and nine quark polarization bins for the valence quarks and seven for the sea quarks. While at times, the results may be referred to as being produced three-dimensionally binned asymmetries, the reader should be aware that the x-binned inclusive asymmetries are *always* included. This result can be seen in Figure 6.2 and is left unconstrained by the positivity limit which will be described in the following sections.

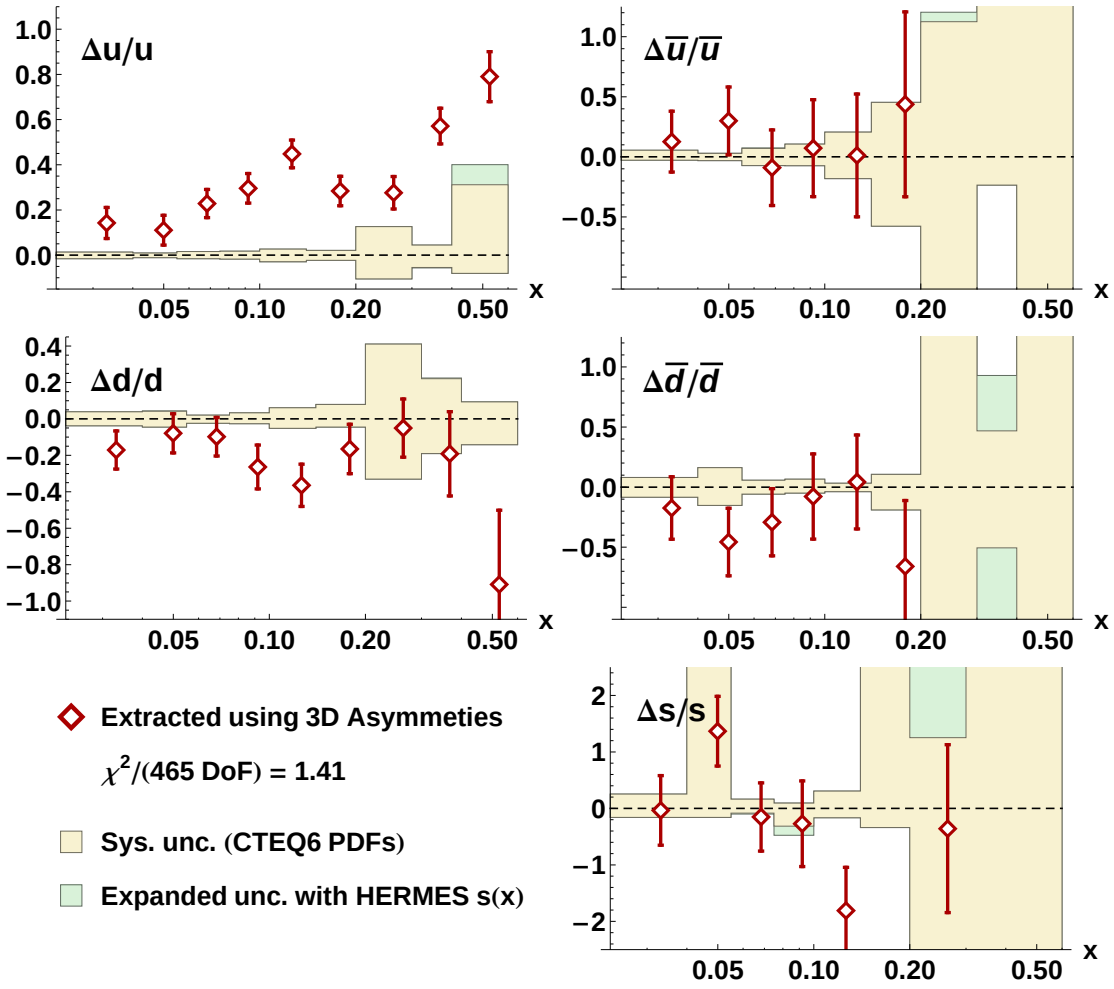

Figure 6.2: The result of the $\frac{\Delta q}{q}(x)$ extraction using the three-dimensional Born asymmetries of Section 4.5.1 and purities generated with the 2004c JETSET tune (Section 5.3.2). No fit constraints were applied. The bands represent systematic uncertainties under different assumptions for unpolarized strange quark density (yellow for CTEQ6L, green for CTEQ6L with HERMES modified $s(x)$ and $\bar{s}(x)$ [33]).

6.1.4 The Impact of Semi-Inclusive Kinematic Variables

As described earlier, a major goal of this analysis was to explore the use of additional, previously unexplored kinematic dimensions. One reason for this was to take advantage of as much statistical leverage as possible in the extraction of the quark polarizations. An early and driving hypothesis was the possibility that because semi-inclusive variables carry information about the fragmentation regime in which an observed hadron was produced, additional information about the hadron–struck-quark correlation might be unknowingly lost when these variables are integrated out. This hypothesis is strongly supported by the clear dependence of the purities on the semi-inclusive variables z and $p_{h_\perp}$ as seen in Section 5.3.2.

A Monte Carlo Study

A study was performed in order to estimate the impact of the inclusion these additional kinematic dimensions on the statistical uncertainties of the quark polarizations. Asymmetries were produced by combining Monte Carlo generated purities and CTEQ6L [40] spin-averaged and the GRSV (Leading-Order Standard) [39] polarized parton distributions. The purities and resulting asymmetries were binned in several ways: one-dimensional x-binned (as in the published result), two-dimensional x-$p_{h_\perp}$ and x-z-binned, and three-dimensional x-$p_{h_\perp}$-z-binned. The asymmetries from the published analysis were applied to the x-binned asymmetries. In order to estimate the uncertainties for the higher dimensionally binned asymmetries, the Monte Carlo yields used to generate the purity matrices were used to scale the x-binned uncertainties to reflect the division of the same statistics into more bins.

Using the extraction method described in Section 6.1, the purities and constructed asymmetries were used to extract the quark polarizations $\frac{\Delta q}{q}(x)$ and finally the CTEQ6L parameterization was reapplied to the result to yield the quark helicity distributions $x\Delta q(x)$. The result, Figure 6.3, is plotted with all extracted distributions at a common central value (that of the 1D extraction) so the impact of the binning choice would be clearly visible.

The Impact of Semi-Inclusive Binning On Data

While some of the uncertainty improvement observed in the study was realized when actual data was analyzed (which we will see in Figure 6.8), an important complicating factor was not taken into consideration in the Mote Carlo study: the apparent error-bar inflation, described in Section 4.3.5, is likely exaggerated by the increase in the number of observed bins contributing to each final Born bin in the asymmetries. Some of this inflation will be reflected in the full bin-to-bin covariance matrix, but as previously explained, this may not be reflected in the plotted error bars. A comparison of analytic fits to the data points should revel more about the statistical impact (Section 6.3).

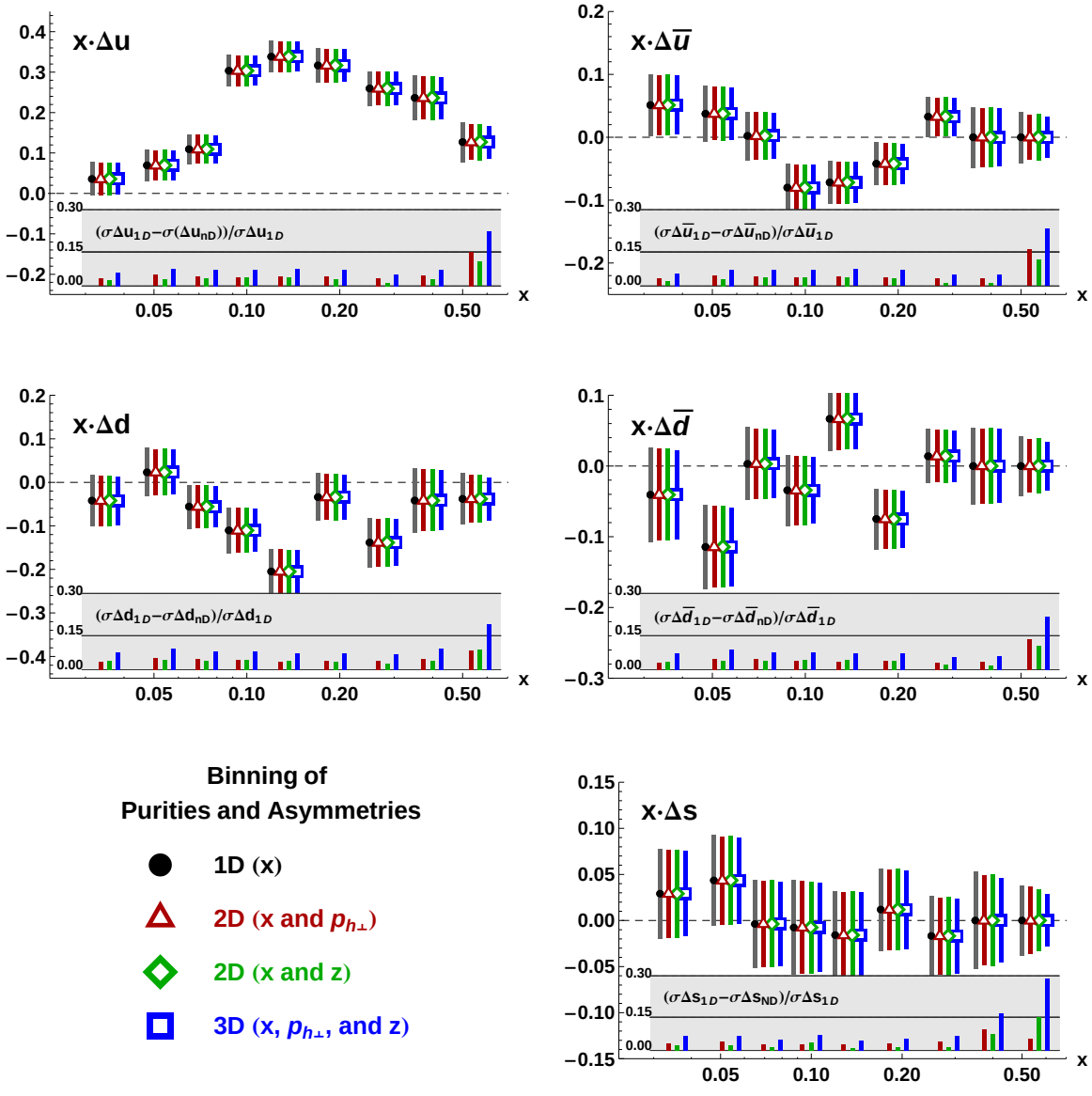

Figure 6.3: Result of a Monte Carlo study that demonstrates the benefits of additional kinematic dimensions on the precision of the extracted quark polarizations. The inset depicts the fractional reduction of the statistic uncertainties for each set relative to the one-dimensionsal x-binned extraction.

6.1.5 Assuming a Negligible Sea Contribution in the Valence Regime

For $x > 0.3$, an assumption is often made that the sea quarks contribute negligibly to the parton distributions. We generally expect that the low-x region is filled with many low momentum-fraction gluons. This leaves the sea-quarks, which are daughter particles of the gluons largely delegated to the low-x regime.

Because of this, we have chosen to fix the sea quark polarizations to zero for the two x bins above $x = 0.3$. While this takes some ambiguity out of the fit, it has a relatively small impact on the large-x valence distributions. Primarily, it serves the purpose of removing near-meaningless large error bar points from the quark polarization result.

6.1.6 The Positivity Limit and Possible Fit Constraints

One thing that can be observed in the $\Delta q/q(x)$ extraction (Figure 6.2) is that some of the values exceed one in magnitude, particularly for high-x bins and for the strange quark polarization. Strictly speaking, the physical quantity $|\Delta q/q(x)|$ must be less than one. This can be seen easily though the definitions of $q(x)$ and $\Delta q(x)$:

$$\begin{aligned} \Delta q(x) &= q^+(x) - q^-(x) \\ q(x) &= q^+(x) + q^-(x). \end{aligned} \tag{6.5}$$

Since $q^+(x)$ and $q^-(x)$ are number densities, they must have positive values. Because of this $q(x)$ must always be greater than or equal to $|\Delta q(x)|$. This is often referred to as *the positivity limit*.

The primary reason that this limit is sometimes violated in this analysis is that the quark polarizations are extracted using purity matrices that depend on parameterizations of the spin-averaged parton distributions, CTEQ6L, and of the F2 structure function, ALLM97 [22]. First of all, these parameterizations may not be entirely appropriate at HERMES kinematics. In addition, in the case of CTEQ6L, assumptions are made, such as $s(x) = \bar{s}(x)$, which provide PDF fitters with additional constraint, where the data available is inadequate, at the cost of additional model dependence. The fact that our extracted values exceed the physical limit may be an indication of discrepancy between the data measured at HERMES and the parameterizations used in this extraction. Additionally, it is possible that the RICH unfolding scheme employed (Section 3.1.2) could potentially cause small negative yields in bins where the data is sparse as it relocates counts from one bin to another. This can result in quark polarizations outside the physical limit where there are few statistics (high-x) as it would correspond to a non-physical $|A_1(x)| \geq 1$ asymmetry.

A sensible suggestion could be made to *constrain* the quark polarizations so that their magnitude doesn't exceed one in the extraction (Figure 6.4). Imposing such a constraint has

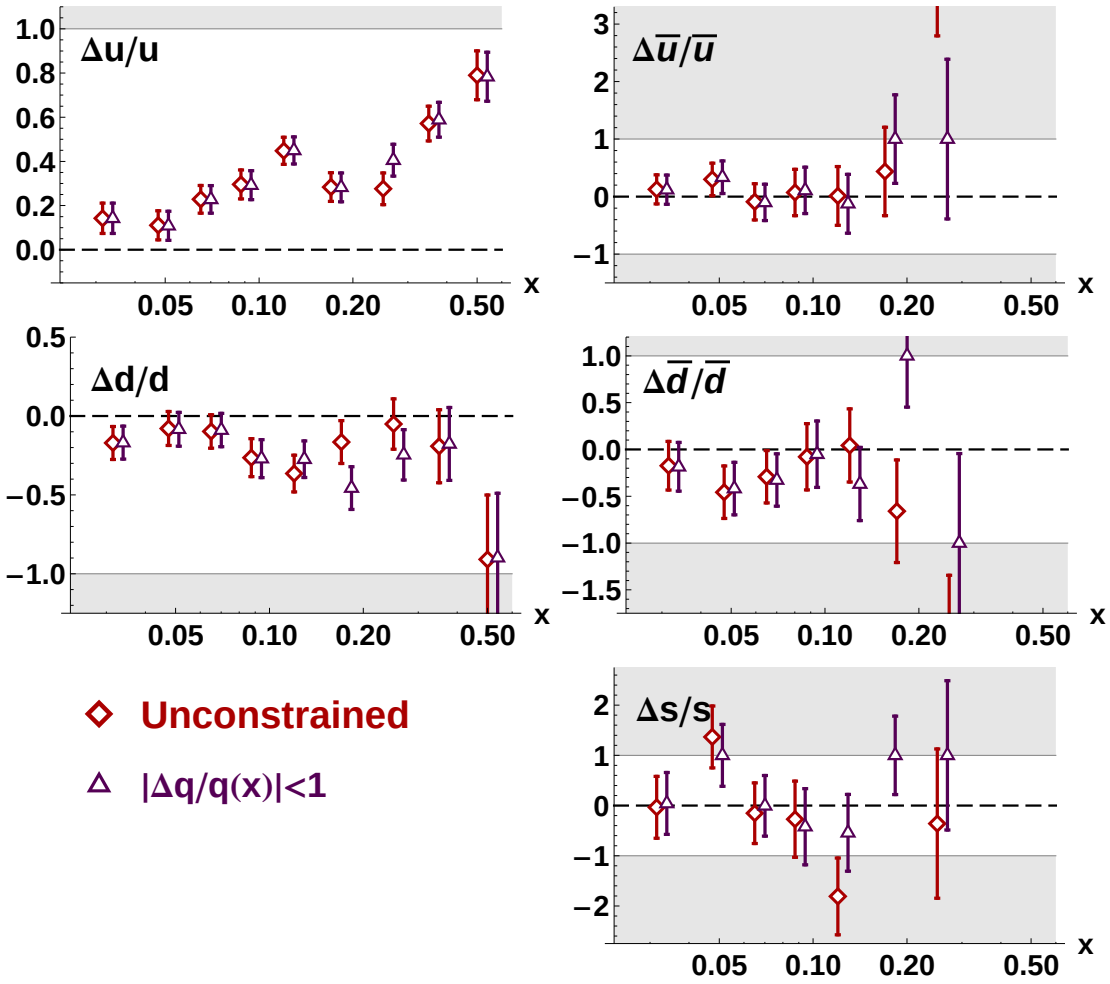

Figure 6.4: Comparison of quark polarizations extracted using three-dimensional semi-inclusive asymmetries with and without constraint of $|\Delta q/q(x)| \leq 1$. The white band represents the range of physically meaningful values for the quark polarizations.

benefits and drawbacks. An obvious benefit of a fit constraint is that all points in the extraction will take on physically meaningful values. Most points outside the physically meaningful region take on values of ± 1 as they are pushed against the constraint boundary. Previously physical values will move to some degree as the value of each $\Delta q/q(x)$ bin depends both on the other quark flavors in the same bin and, through kinematic smearing, on other kinematic bins of the same quark flavor (and hence, and to a lesser extent, on every other bin in the extraction).

A drawback, however, is the difficulty in establishing a meaningful measure of statistical uncertainty for bins which are forced against the constraint bound. An asymmetric error bar might be appropriate, but it would be difficult to interpret it in the normal 1-σ sense. A further complication is that applying such a constraint would in essence be *forcing* the points to take physical values despite the inconsistency between data and parameterizations described above.

In light of these drawbacks, it seems most sensible to provide the unconstrained result qualified by an understanding of some degree of internal inconsistency related to the unpolarized PDF parameterizations to explain the few places where the extraction provides a problematic result. We will see, however, that the χ^2 agreement of analytic fits suffer to some degree as this instability causes some non-statistical variation in the points (the very non-physical bin six of $\Delta s/s(x)$, for example, which if off-scale positive in Figure 6.2, but quite visible in the plot of $x\Delta q(x)$, Figure 6.7).

6.2 The Quark Helicity Densities of the Nucleon

As discussed in Chapter 1, the quark helicity densities, $\Delta q(x)$, represent the contributions of the individual quark flavors to the spin-dependant structure function $g_1(x)$:

$$g_1(x) = \frac{1}{2}\sum_q \; e_q^2 \;\left[q^+(x) - q^-(x)\right] = \frac{1}{2}\sum_q \; e_q^2 \;\Delta q(x). \tag{6.6}$$

While the calculation of $\Delta q(x)$ from the quark polarizations, $\Delta q/q(x)$ is, in essence, as simple as multiplying by the unpolarized parton distributions q(x) which are experimentally well established, there are additional complicating factors that must be taken into account.

6.2.1 Removing the dependence on the unpolarized PDFs from the Quark Polarizations

A first consideration is that there is some importance in utilizing the same unpolarized PDFs throughout the entire analysis. If the analysis is inconsistent in this regard, the discrepancy will likely manifest itself as a unwanted modification of the final helicity densities.

While unpolarized PDFs appear in the Monte Carlo event generator from which the purities are calculated as we've already seen, they also enter the analysis in this final step. In the generator Monte Carlo, the ALLM parameterization of $F_2(x)$ is used to produce a HERMES-like cross-section while the *flavor-separated* CTEQ6L is used to select between different quark flavors. The benefit of this combination is that ALLM produces an accurate cross-section at HERMES kinematics which CTEQ6L does not. This can be seen in Figure 6.5 (left). CTEQ6L, however provides the flavor separation that ALLM does not.

This suggests the following calculation to produce the final quark polarization:

$$\Delta q(x) \;=\; \frac{\Delta q}{q}(x) \times C_R(x) \; F_{2_{\mathrm{ALLM}}}(x) \frac{q_{\mathrm{CTEQ}}}{\sum_q q_{\mathrm{CTEQ}}}(x), \tag{6.7}$$

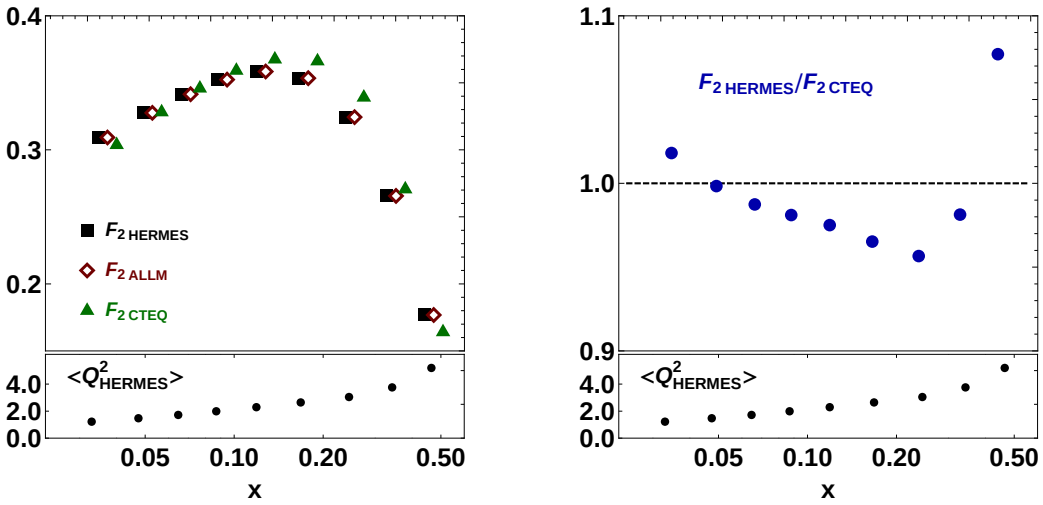

Figure 6.5: (left) A comparison of $F_2(x)$ computed from CTEQ6L, $F_2(x)$ from the more HERMES appropriate ALLM parameterization, and a recent fit of $F_2(x)$ performed at HERMES to the HERMES multiplicity dataset [46]. (Right) The ratio of $F_2(x)$ computed from CTEQ6L to the HERMES $F_2(x)$ fit. This can be interpreted as a measure of discrepancy between the CTEQ PDF parameterization and the true cross-section in the HERMES kinematic regime.

which can be trivially rewritten,

$$\Delta q(x) \;=\; \frac{\Delta q}{q}(x) \times C_R(x)\; q_{\mathrm{CTEQ}}(x) \frac{F_{2\mathrm{ALLM}}}{\sum_q q_{\mathrm{CTEQ}}}(x), \tag{6.8}$$

so that one can think of the conversion as multiplication by CTEQ6L PDFs with an accompanying cross-section correction, $\frac{F_{2\mathrm{ALLM}}}{\sum_q q_{\mathrm{CTEQ}}}(x)$. The factor C_R is described in the next section.

6.2.2 The C_R Factor – Adapting the CTEQ6 Unpolarized PDFs

In order to remove the unpolarized PDF denominator from the quark polarizations, we have taken advantage of the CTEQ6L parameterization of experimentally determined unpolarized parton distributions. Because of a subtle difference in definitions of $q(x)$ used, we must include an additional factor. CTEQ fits the sums of its parton distributions to the spin-averaged structure function $F_2(x)$ via the following relation:

$$F_2(x) \;=\; x \sum_q \; e_q^2 \; q_{\mathrm{CTEQ}}(x) [47]. \tag{6.9}$$

The result of this is that the parton distributions that CTEQ provides include a contribution from the longitudinal component of photon polarization which we've taken some care to remove completely from our asymmetries when $A_{||}$ is converted to A_1. As previously described, we define

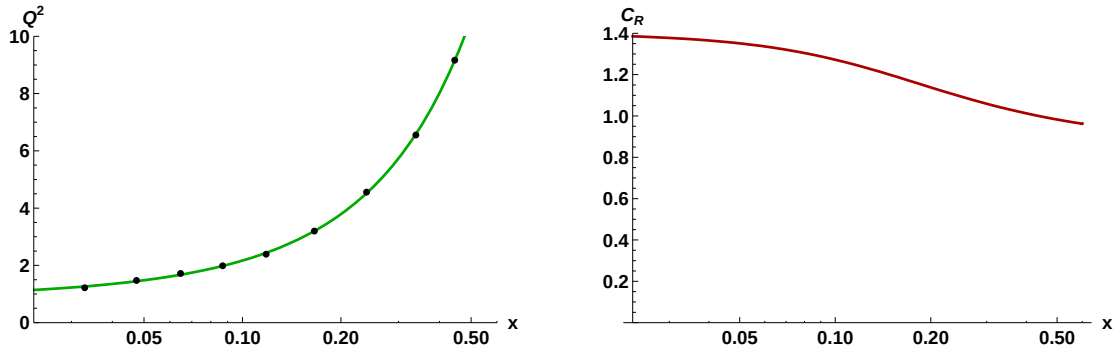

Figure 6.6: (Left) Black points represent $< Q^2 >$ in each x-bin of the inclusive asymmetry from the proton target which are fit with a smooth quadratic function (green). (Right) The $C_R(x)$ factor computed using the parameterization of $Q^2(x)$ shown on the left panel. This correction factor is used to remove the unwanted longitudinally polarized photon contribution to the $F_2(x)$ structure function (and to similarly defined PDFs) leaving all factors defined in terms of the pure transversely-polarized $F_1(x)$.

$q(x)$ in terms of $F_1(x)$ as follows,

$$F_1(x) \;=\; \frac{1}{2}\sum_q \; e_q^2 \; q(x). \tag{6.10}$$

The Callan-Gross relation(Equation 1.10), established a simple idealized relationship between F_1 and F_2 structure function in the large-Q^2 limit. In our scattering regime, Q^2 is somewhat more modest: the quark masses and transverse momentum can not be neglected and the frozen approximation cannot be considered exact. The following relationship between the spin-averaged structure functions, including a parameterized R $(= \sigma_L/\sigma_T)$, better reflects lepton-nucleon scattering in this regime:

$$2xF_1(x) = \frac{1+\gamma^2}{1+R}F_2(x), \tag{6.11}$$

which suggests that the relationship between our $F_1(x)$ defined $q(x)$ and CTEQ's $F_2(x)$ defined $q_{\text{CTEQ}}(x)$ is:

$$q(x) = \frac{q_{\text{CTEQ}}(x)}{C_R}, \tag{6.12}$$

where

$$C_R \;=\; \frac{1+R}{1+\gamma^2}. \tag{6.13}$$

6.2.3 Final Helicity Distributions

Finally then, taking all these factors into account, Figure 6.7 presents the flavor-separated quark helicity distributions computed with our three-dimensional semi-inclusive and x-binned inclusive asymmetries. The distributions are in good agreement with the leading-order GRSV

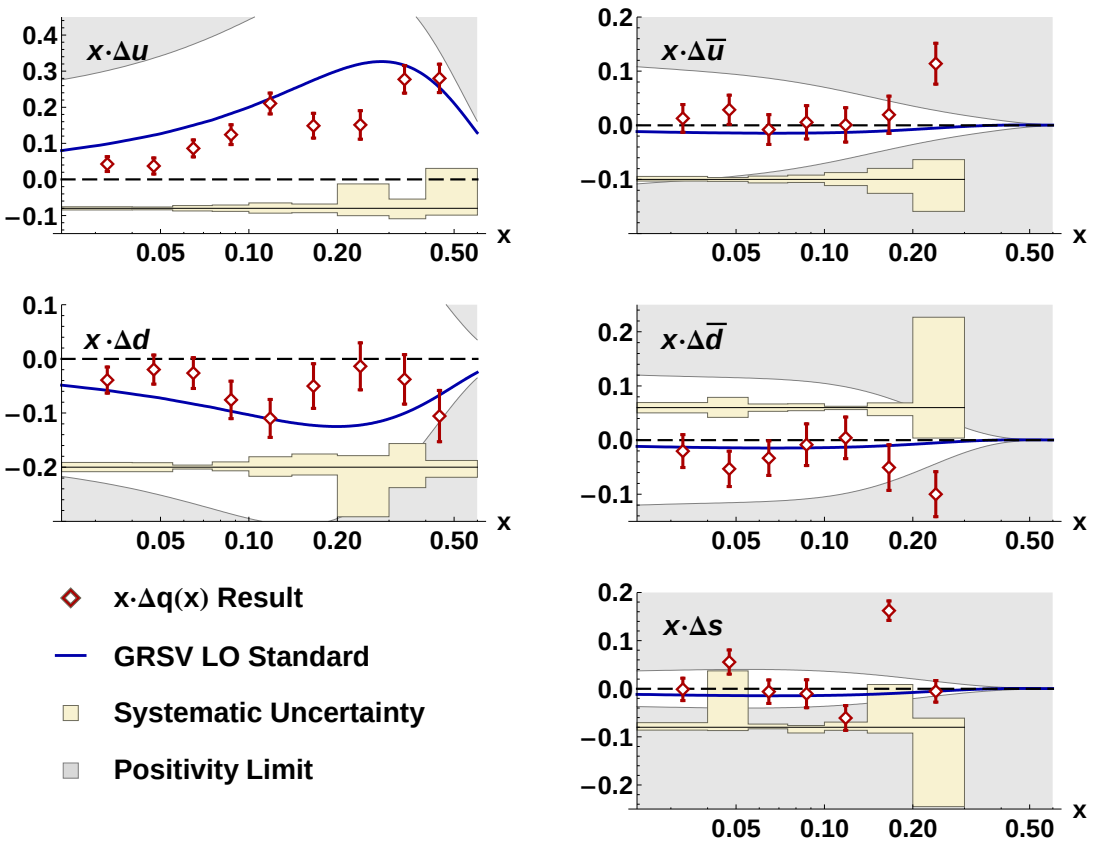

Figure 6.7: The quark helicity distributions. The white region represents the range of physically meaningful values allowed by the positivity limit. Its violation is addressed in Section 6.1.6.

parameterization.

A comparison of this result with that of the prior analysis if given in 6.8. Statistical uncertainties are improved in some areas and the systematic uncertainty is significantly different. This is primarily the result of the improved (generally reduced) purity-related systematic uncertainty and also the inclusion of the previously neglected PDF uncertainty.

6.3 Fits to the Quark Polarizations

A major conclusion of this analysis is that correlated statistical errors can be deceptive as only the diagonal elements of the error matrix are plotted as error bars. The natural way to assess the true statistical power of a dataset is to impose a model of some sort. While this also imposes a set of assumptions, an analytic function, for example, typically assumes a degree of smoothness; it can be helpful for presentation purposes and for comparing two highly correlated datasets. The extracted

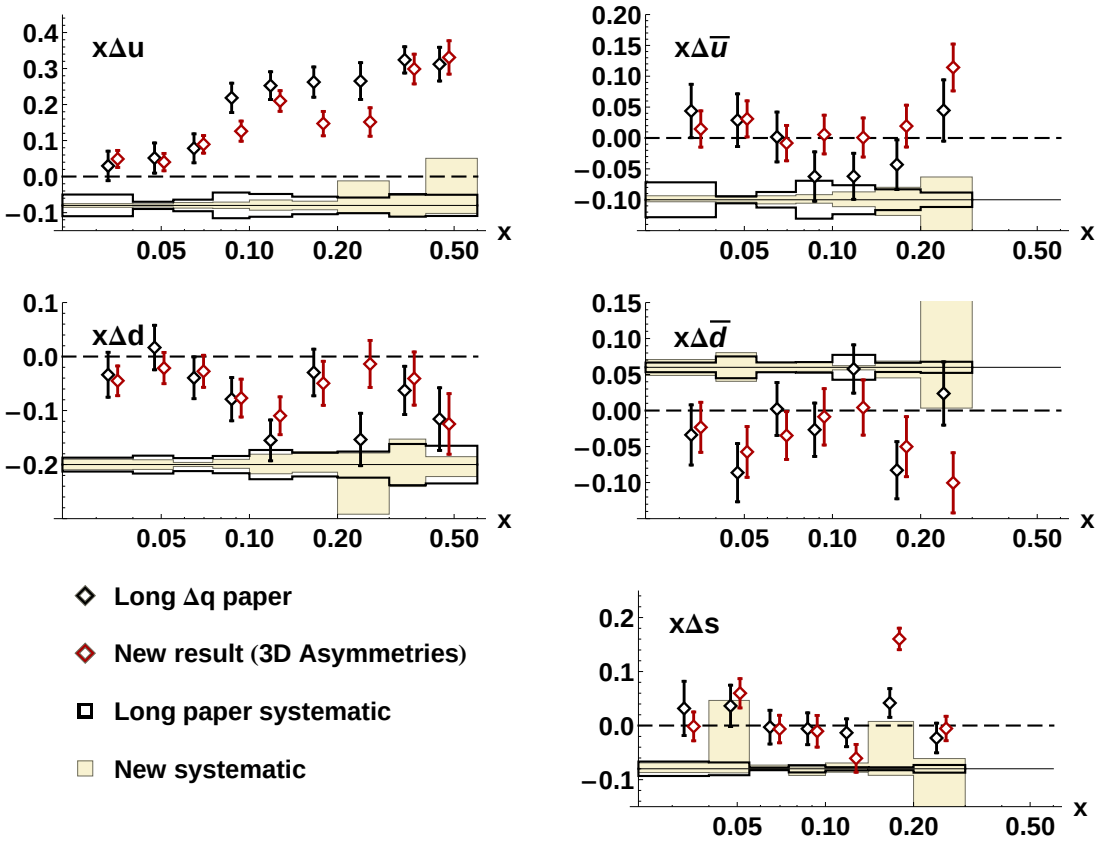

Figure 6.8: The quark helicity distributions extracted from the three-dimensionally binned asymmetries compared with the result from the prior HERMES analysis, "Long Δq paper" [16]. The statistical uncertainty is improved in some regions. The systematic uncertainties are improved significantly at small-x. This is primarily due to improvements in the Lund-tune uncertainty described in Chapter 5. In some regions the systematic uncertainty has become larger as the prior analysis made no attempt to estimate the model-dependant uncertainties of the unpolarized PDF parameterizations.

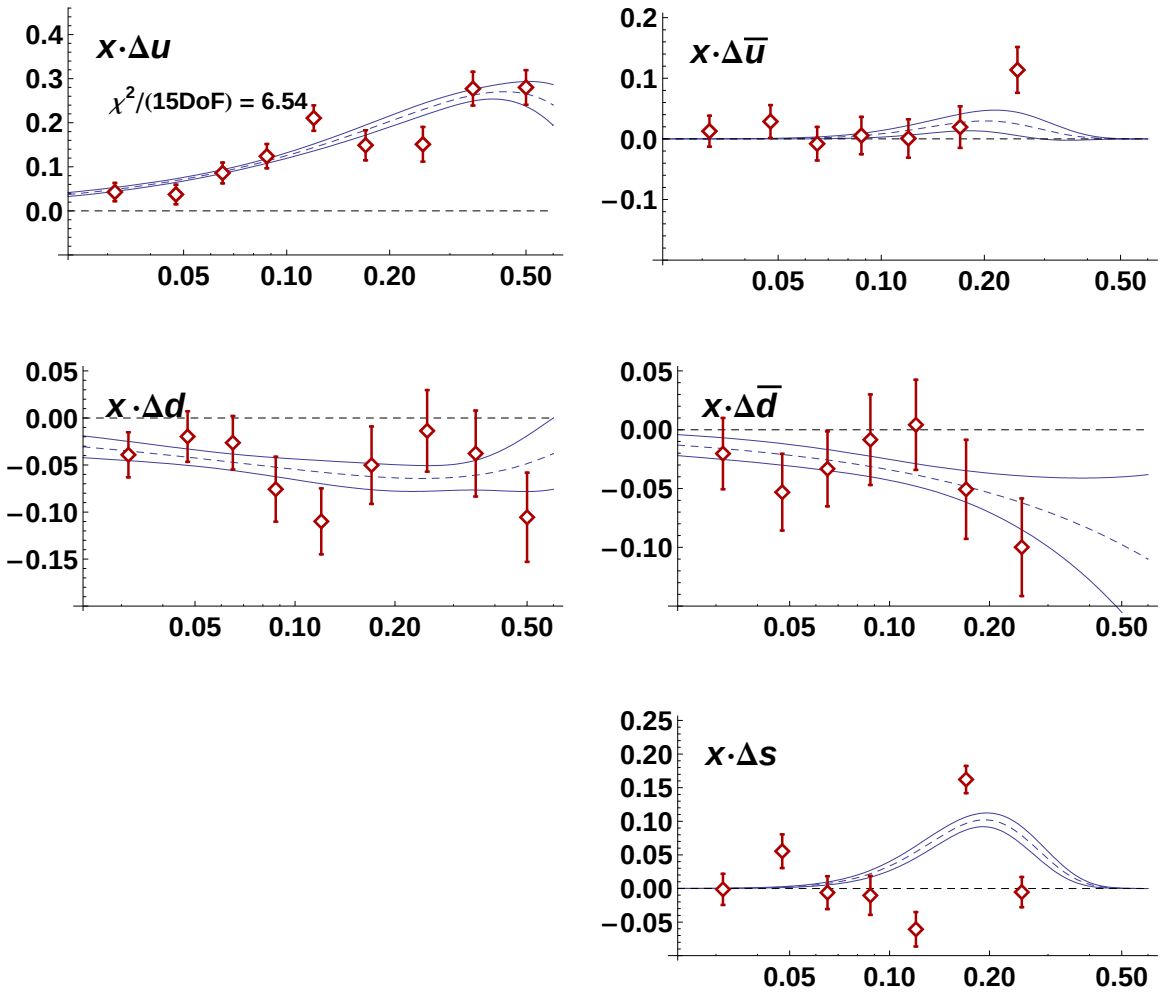

Figure 6.9: A polynomial fit of the form $q(x) = A\ x^{B^2}(1-x)^{C^2}$ to the three-dimensional extraction of $x\Delta q(x)$. Analytic fits can give an indication of the statistical power hidden in bin-to-bin covariance that that is not obvious from the error bars themselves.

$x\Delta q(x)$ points are provided in Figure 6.9 fit with the following functional form:

$$q(x) = A\ x^{B^2}(1-x)^{C^2}. \tag{6.14}$$

Squaring the coefficients in the fit constrains the exponents to positive values.

The large resulting $\chi^2/(15DoF) = 6.54$ is likely the result of the non-statistical variation in the points due to discrepancy between the unpolarized PDFs and physics in the HERMES kinematic regime, particularly for $x\Delta s(x)$ (note the large point variation relative to the error bar size!). This was addressed in 6.1.6.

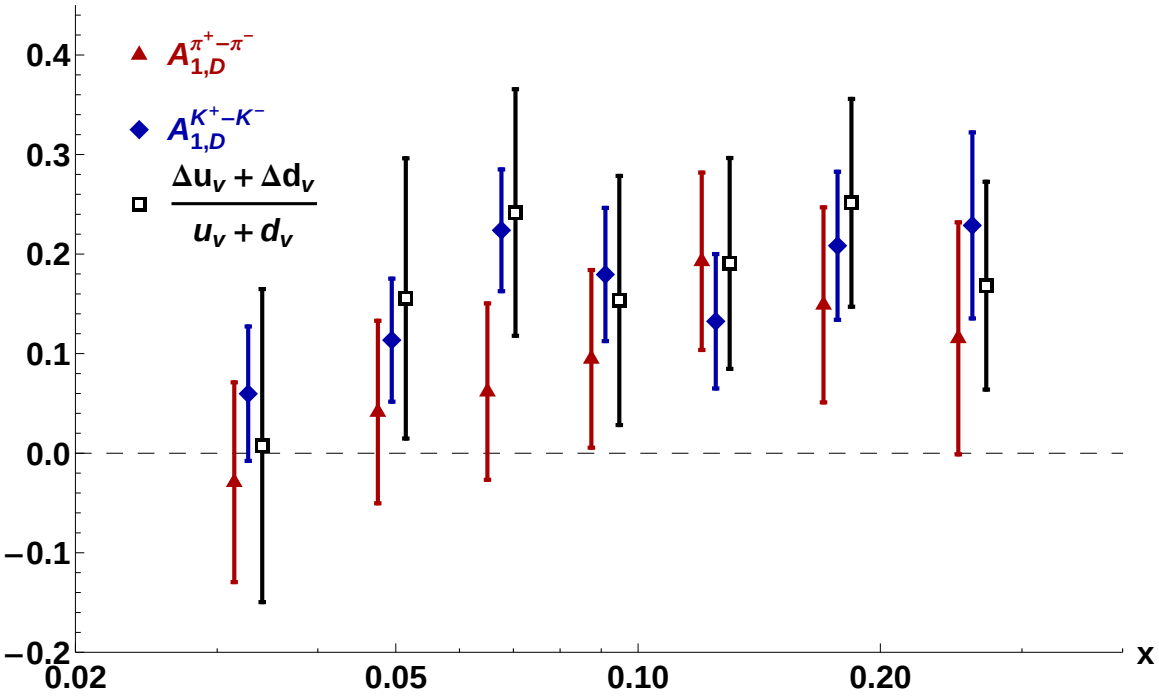

Figure 6.10: The hadron charge difference asymmetries from the deuterium target, $A_{1d}^{h^+-h^-}(x)$, for pions and kaons plotted with the quantity $\frac{\Delta u_v+\Delta d_v}{u_v+d_v}(x)$ from the purity extraction.

6.4 Valence Distributions and Difference Asymmetries

The hadron charge difference asymmetries, $A_1^{h^+-h^-}(x)$ were computed in Section 4.5.4. If charge conjugation symmetry in fragmentation is assumed, these asymmetries can be equated to the following rato for valence parton distributions, $\frac{\Delta u_v+\Delta d_v}{u_v+d_v}(x)$. While we drew the validity of this assumption into question in Section 5.2 using JETSET, our fragmentation Monte Carlo, it seems the natural point to compare these asymmetries with the valence distribution ratio computed from the extracted helicity distributions of this chapter.

Within the statistical error bars, which are much larger than any symmetry breaking effect we could produce using JETSET, the points agree. It should be noted however, that all of the yields that comprise both the pion and kaon charge difference asymmetries are ingredients in the helicity densities. This should be kept in mind when interpreting their uncertainties.

6.5 The Light Sea Asymmetry

A final derivative result of the quark helicity densities is the asymmetry of the light sea, $x\left(\Delta\bar{u}(x) - \Delta\bar{d}(x)\right)$, which is given in the left panel of Figure 6.11. This quantity is is somewhat larger than light sea asymmetry produced in the prior analysis [16] (right panel). This could be the result of additional low momentum hadrons from the deuterium sample, but could also be related

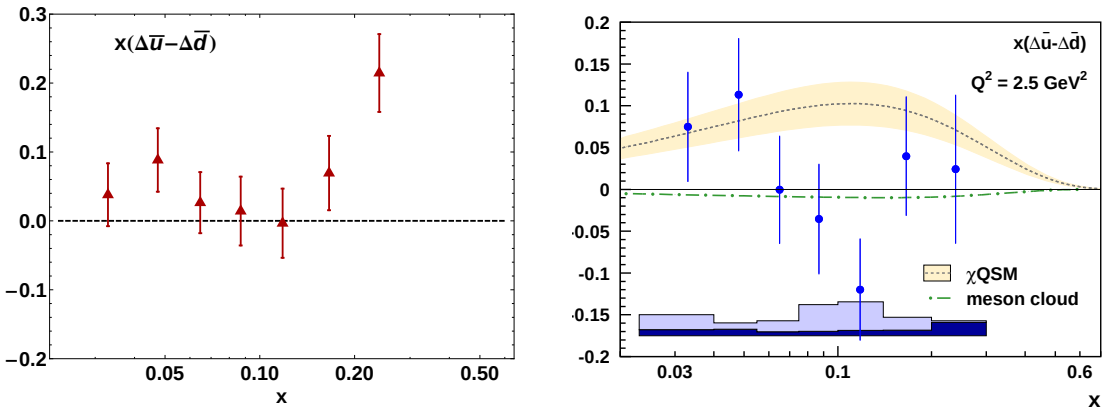

Figure 6.11: Comparison of the light sea asymmetry extracted from the three-dimensionally binned semi-inclusive asymmetries (left) with the same quantity from the prior HERMES analysis [16] (right). Note the difference in scale between the two plots. This analysis clearly yields a more positive light sea asymmetry and one that is somewhat more consistent with the predictions of the chiral quark soliton model (χQSM) [48].

to additional information included in the three-dimensional quark polarization extraction. While the exact χ^2 comparison of this new result and the prediction of the chiral quark soliton model [48] is not available at this time, it appears that agreement is better.

References

[1] H. Yukawa, Proc. Phys. Math. Soc. Jap. **17**, 48 (1935).

[2] C. M. G. Lattes, H. Muirhead, G. P. S. Occhialini, and C. F. Powell, Nature **159**, 694 (1947).

[3] M. Gell-Mann, Physics Letters **8**, 214 (1964).

[4] HERMES, A. Airapetian *et al.*, Phys. Rev. **D71**, 032004 (2005), hep-ex/0412027.

[5] Particle Data Group, C. Amsler *et al.*, Phys. Lett. **B667**, 1 (2008).

[6] J. D. Bjorken and E. A. Paschos, Phys. Rev. **185**, 1975 (1969).

[7] F. Halzen and A. D. Martin, *Quarks & Leptons: An Introductory Course in Modern Particle Physics* (Wiley, 1984).

[8] S. Wandzura and F. Wilczek, Phys. Lett. **B72**, 195 (1977).

[9] D. J. Gross and F. Wilczek, Phys. Rev. Lett. **30**, 1343 (1973).

[10] R. Brandelik *et al.*, Physics Letters B **86**, 243 (1979).

[11] PHENIX, A. Bazilevsky, Czech. J. Phys. **55**, A55 (2005), hep-ex/0505028.

[12] STAR, J. Sowinski, Future Investigations of the Flavor Dependence of Sea Quark Helicities at STAR, in *Proceedings of the 18th International Symposium on Spin Physics*, 2009, 0901.4581.

[13] HERMES, A. Airapetian *et al.*, Phys. Rev. **D75**, 012007 (2007), hep-ex/0609039.

[14] HERMES, K. Ackerstaff *et al.*, Nucl. Instrum. Meth. **A417**, 230 (1998), hep-ex/9806008.

[15] W. R. Leo, Berlin, Germany: Springer (1987) 368 p.

[16] HERMES, A. Airapetian *et al.*, Phys. Rev. **D71**, 012003 (2005), hep-ex/0407032.

[17] HERMES, A. Airapetian *et al.*, Nucl. Instrum. Meth. **A540**, 68 (2005), physics/0408137.

[18] E. D. Bloom *et al.*, SLAC-PUB-0653, Submitted to Int. Symp. on Electron and Photon Interactions at High Energies, Daresbury, Sept. 1969.

[19] E143 collaboration, Physics Letters B **452**, 194 (1999).

[20] O. A. Rondon, Phys. Rev. C **60**, 035201 (1999).

[21] I. Akushevich, H. Bottcher, and D. Ryckbosch, (1998), hep-ph/9906408.

[22] H. Abramowicz and A. Levy, (1997), hep-ph/9712415.

[23] HERMES, A. Airapetian *et al.*, Phys. Lett. **B442**, 484 (1998), hep-ex/9807015.

[24] HERMES, K. Ackerstaff *et al.*, Phys. Lett. **B464**, 123 (1999), hep-ex/9906035.

[25] I. V. Akushevich and N. M. Shumeiko, J. Phys. **G20**, 513 (1994).

[26] R. N. Cahn, Physics Letters B **78**, 269 (1978).

[27] A. Bacchetta *et al.*, Journal of High Energy Physics **2007**, 093 (2007).

[28] F. Giordano and R. Lamb, Measurement of azimuthal asymmetries of the unpolarized cross-section, HERMES Release Report, 2008.

[29] F. Giordano and R. Lamb, Measurement of azimuthal asymmetries of the unpolarized cross section at hermes, in *Proceedings of the 18th International Symposium on Spin Physics*, 2009.

[30] M. Anselmino, A. Efremov, A. Kotzinian, and B. Parsamyan, Phys. Rev. **D74**, 074015 (2006), hep-ph/0608048.

[31] H. Avakian, Studies on transverse spin effects at JLab, in 2^{nd} *Workshop On QCD Structure of the Nucleon*, 2006.

[32] P. Bosted, Semi inclusive dis results from JLab, in *Gordon Conference On Photonuclear Reactions*, 2008.

[33] HERMES, A. Airapetian *et al.*, Phys. Lett. **B666**, 446 (2008), 0803.2993.

[34] E. Christova and E. Leader, Phys. Lett. **B468**, 299 (1999), hep-ph/9907265.

[35] E. Christova and E. Leader, Nuclear Physics B **607**, 369 (2001).

[36] COMPASS, M. Alekseev *et al.*, Phys. Lett. **B660**, 458 (2008), 0707.4077.

[37] L. L. Frankfurt *et al.*, Phys. Lett. **B230**, 141 (1989).

[38] Spin Muon, B. Adeva *et al.*, Phys. Rev. **D58**, 112002 (1998).

[39] M. Gluck, E. Reya, M. Stratmann, and W. Vogelsang, Phys. Rev. **D63**, 094005 (2001), hep-ph/0011215.

[40] J. Pumplin *et al.*, JHEP **07**, 012 (2002), hep-ph/0201195.

[41] T. Sjostrand, Pythia 5.7 and jetset 7.4 physics and manual, 1995.

[42] B. Andersson, G. Gustafson, and B. Soderberg, Z. Phys. **C20**, 317 (1983).

[43] F. James, Minuit - function minimization and error analysis - reference manual, 1998.

[44] F. M. Menden, *Determination of the gluon polarization in the nucleon*, PhD thesis, Albert-Ludwigs Universitat Freiburg, 2001, DESY-THESIS-2001-060.

[45] Jürgen Wendland, *Polarized Parton Distributions Measured at the HERMES Experiment*, PhD thesis, Simon Fraser University, 2003.

[46] D. Gabbert, *Determination of the structure function F_2 at Hermes*, PhD thesis, Hambrg University, 2008.

[47] H. L. Lai *et al.*, Phys. Rev. D **51**, 4763 (1995).

[48] P. Schweitzer *et al.*, Phys. Rev. D **64**, 034013 (2001).

Author's Biography

Joshua George Rubin was born and raised in the San Francisco Bay Area. Though his early interests included art, music, and computers, an interest in science was particularly pronounced. Josh attended the University of California at Santa Barbara and graduated with degrees in physics and religious studies. After working in the computer industry for a year, he decided that the weather in California was too mild for his taste and matriculated to the University of Illinois at Urbana-Champaign to continue his studies in physics. Lured by the possibility of working with computer simulations and the promise of travel to Europe, he became deeply interested in the physics of the strong nuclear force.

Josh particularly enjoys contributing where physics intersects computing and art. Through his thesis work and stimulating exchanges with colleagues both in Urbana and in the HERMES collaboration in Hamburg, Germany, Josh finds himself as fascinated by the inner-workings of nature as he can remember ever having been.

Following the completion of his Ph.D., Josh will take a postdoctoral position at Argonne National Laboratory in Chicago where he will continue to study the individual quark contributions to the structure of the proton, particularly the quark sea in the large-x scattering regime.